

Characterization of Interfacial Interactions by Functionalized AFM Probes

Laura Rickard Dickinson

Rileyville, Virginia

Bachelor of Science, University of Mary Washington, 2010

A Dissertation presented to the Graduate Faculty  
of the College of William and Mary in Candidacy for the Degree of  
Doctor of Philosophy

Department of Applied Science

The College of William and Mary  
May, 2016

© Copyright by Laura R. Dickinson 2016

## APPROVAL PAGE

This Dissertation is submitted in partial fulfillment of  
the requirements for the degree of

Doctor of Philosophy

Laura Rickard Dickinson

Laura Rickard Dickinson

Approved by the Committee, March, 2016

Hannes Schniepp

Committee Chair

Associate Professor Hannes C. Schniepp, Applied Science  
The College of William & Mary

Mark K. Hinders

Professor Mark K. Hinders, Applied Science  
The College of William & Mary

Michael J. Kelley

Professor Michael J. Kelley, Applied Science  
The College of William & Mary

Mumtaz Qazilbash

Assistant Professor M. Mumtaz Qazilbash, Physics  
The College of William & Mary

## ABSTRACT

Interfacial interactions play a crucial role in many complex materials systems, determining many of their properties. However, characterization of these interactions, especially at the micro- to nanometer length scales is experimentally challenging. Consequently, insufficient knowledge of these systems limits technological advances in important applications. In this work, custom functionalized atomic force microscopy (AFM) probes were developed to measure the interaction forces in two important systems: petroleum reservoirs and nanocomposites. Our work seeks a deeper understanding of the specific interactions that occur in these two systems so that modified approaches can be developed to improve them.

Petroleum recovery is concerned with maximizing the collection of crude oil, which adheres to rock surfaces underground and resists release when flushed with injection water. To promote more efficient oil extraction, the injection water can be tailored to decrease this oil–rock adhesion. In our study of petroleum recovery, we coated a probe in crude oil and dried the oil to create a robust layer. By performing force measurements with this probe on a mica substrate and varying the surrounding aqueous composition, we observed the effect of multiple variables on the relevant forces in a reservoir, ultimately providing enhanced predictive capabilities for increased oil extraction in injection wells.

To achieve a graphene oxide (GO) nanocomposite with optimal properties requires a strong bond between the nanofiller particles and surrounding polymer matrix. To this end, we studied the interactions within a GO–polymer nanocomposite by coating a probe in GO flakes and performing force measurements on polymer substrates. The preferential attraction between GO and some polymers is consistent with the results of recent interfacial tests performed in our lab. Our research provides crucial information for the selection of novel GO–polymer combinations, which can be implemented in superior reinforced nanocomposite systems. Through development of these novel tools, we anticipate that our customized probes will enhance predictive capabilities in the study of colloidal and other interfacial systems.

## TABLE OF CONTENTS

Acknowledgements	iii
Dedications	iv
List of Tables	v
List of Figures	vi
Chapter 1. Introduction and Theory	1
a. Research Objectives	1
b. Background	2
c. Investigated Systems	15
Chapter 2. Experimental Methods	20
a. Equipment	20
b. Materials for Probes and Liquid Cell Solutions	25
c. Sample Preparation	27
d. Bare Silica Colloidal Probe	47
Chapter 3. Crude Oil Functionalized Colloidal Probe	62
a. Development	62
b. Wet Oil-Coated Probe	65
c. Dried Oil-Coated Probe	67
d. Discussion	98
e. Conclusions	105
Chapter 4. Graphene Oxide Functionalized Probe	107
a. Development	107
b. Force Spectroscopy Results	116

c. Peeling Test Results and Discussion	122
d. Peeling Test/Probe Comparison	133
e. Conclusion	137
Chapter 5. Alumina Platelet Probe	139
a. Development	139
b. Results and Discussion	145
c. Conclusion	151
Chapter 6. Conclusions and Future Work	152
Appendix A: Optical Analysis of Features in Crude Oil	159
References	163

## ACKNOWLEDGEMENTS

To begin, I want to express my appreciation to Dr. Hannes Schniepp for accepting me into his lab and providing constant support and guidance over the course of my Ph.D. research. Since our collaborators have helped make my research possible, I would like to thank Dr. David Kranbuehl, Dr. Brent Owens, and our fellow researchers at Shell Global Solutions International. Additionally, I want to thank my committee members, Dr. Mark Hinders, Dr. M. Mumtaz Qazilbash, and Dr. Michael Kelley, for the time and effort they have committed to review my dissertation and conduct my defense. The funding for my research was made possible by grants from Shell Global Solutions International and the Center for Innovative Technology (CIT)/Commonwealth Research Commercialization Fund (CRCF) (Grant No. MF145-034-AM). This material is based upon work supported by the National Science Foundation under Grant No. 1534428 and Grant No. DMR-1352542. I would like to acknowledge my great appreciation for this funding. Additionally, I would like to thank my undergraduate adviser, Dr. George King, III for his support and encouragement that I attend graduate school.

My current and former lab colleagues have facilitated my pursuit of this degree. Therefore, I would like to thank those who were present for a significant portion of my research: Minzhen Cai, Jaeton Glover, Qijue Wang, and William Dickinson. In particular, I would like to thank Sean Koebley for his extensive reading and editing of this document. I would also like to thank the undergraduate students who have contributed to my work via AFM scanning (Jing Ye), polyimide substrate creation (Natalie Hudson-Smith), and polyethylene substrate creation (Jake Lisi and Patrick Smith). Furthermore, I would like to thank Lydia Whitaker, Rosario Fox and Lianne Ashburne for their unwavering personal and professional support.

This dissertation is dedicated to my dad (who taught me to love science), my mom (who taught me to never give up), and my husband (who has been my friend, colleague and great love).

## LIST OF TABLES

1. Percentage of curves exhibiting repulsion in 10 mM and 1 mM NaCl liquid cell solutions. The total number of curves tested for each solution molarity is included in the Curves column. 83
2. Summarized literature references of improvements in the mechanical properties of polymers due to the addition of GO flakes. 121

## LIST OF FIGURES

1. Sample force spectroscopy curves: a raw deflection-displacement curve (A) and a processed force vs. tip-to-sample distance curve (B).	3
2. Theoretical effects of differing applied voltage (dashed green line: 20 mV and solid blue line: 200 mV) on electrostatic force trends.	8
3. Effect of two different Hamaker constant, $A_H$ , values on the attractive van der Waals forces. The solid black line designates $A_H = 40$ (vacuum) and the dashed red line designates $A_H = 0.4$ (water).	12
4. Sample processed approach curve with an exponential fit applied to the electrostatic repulsion region. Blue and pink boxes indicate the regions dominated by electrostatic repulsion and van der Waals attraction, respectively.	23
5. Sample processed retract curve with red arrow to indicate the adhesion measurement, e.g. Pull-off Force. Similarly, in an approach curve we would measure the same vertical region of the Snap-down to show the maximum downward deflection from the non-deflected state of the cantilever.	24
6. AFM topography scan of mica to provide an example of surface roughness.	30
7. AFM topography scan of silicon, with GO dispersed on the surface, to provide an example of surface roughness.	31
8. AFM topography scan of PMMA to provide an example of surface roughness.	32
9. AFM topography scan of PVA to show surface roughness.	33
10. AFM topography scan of PEI to show surface roughness.	34
11. AFM topography scan of PI to show surface roughness.	35
12. AFM topography scan of an acrylic substrate to show surface roughness.	36
13. AFM topography scan of HOPG, with GO flakes dispersed on the surface. A roughness measurement was collected on the entire	

image and a localized step (indicated by the “1” cross section bar) to show the different scales of roughness.	37
14. AFM topography scan of silanized mica, with GO dispersed on the surface, to show the surface roughness.	38
15. AFM topography scan of PS, melted on a hot plate and templated on mica, to show surface roughness.	39
16. AFM topography scans of HDPE that was heat pressed and cooled slowly (A) and LDPE that was heat pressed and quenched in liquid nitrogen (B). The cross sections show the relative height comparison of the surface roughness of the two substrates to the surface roughness of a 7.2 $\mu\text{m}$ diameter colloidal probe (C).	41
17. AFM topography scan of GO dispersed on silanized mica to show the relative size, shape, height, and spatial distribution of the GO flakes after spin coating.	43
18. Alumina platelets, dispersed on mica that have been identified optically (A) and with AFM (B). The red boxes indicate the same platelet in both (A) and (B).	44
19. Optical image (A) and AFM topography scan (B) of a mineral grain in a thin section. The scan in (B) was conducted on the grain indicated by the dotted lines in (A).	45
20. Optical microscopy images of three different sandstone grains stabilized in epoxy on which we later performed force spectroscopy experiments.	46
21. Optical image (A) of a cleaved piece of illite mineral and AFM topography scan (B) of a localized area of the illite showing the stepped features of its topography.	46
22. Custom AFM probe holder attached to a translation stage on the Olympus inverted microscope. Inset box shows a magnified view of the probe holder.	48
23. Scanning electron microscope image of a bare silica sphere probe constructed in our lab (A) and a 3D representation of a calibration grating scan of the surface of a silica sphere probe (B). We subtracted the spherical curvature from the AFM topography image to make a new flattened image (C) to which we applied a roughness analysis.	50

24. Processed approach curves from a commercial silicon nitride tip on a mica substrate in 10 mM NaCl (A) and 1 mM NaCl (B). 51
25. Force curves taken with a custom bare silica sphere probe on a mica substrate in the following brine solution order:  
10 mM/1 mM/10 mM NaCl, indicated by black, red, and grey scatter points, respectively. 52
26. Examples of features used to categorize approach curves in the complex brine experiments: repulsion (A), attraction (B) and other (C). In “C”, the curve transitioned directly from the no-deflection region to the constant compliance region without noticeable repulsion or attraction, i.e. snap-down. 53
27. Initial approach curve features for bare silica probe on mica experiments (M-1, M-2, M-3, M-4, M-5, M-6). The x-axis indicates the type of initial feature (Figure 26) observed in the curve and the y-axis indicates the number of each occurrence that were observed for an experimental set. The columns are labeled a separate color for each experimental set with the data from the formation liquid tests (FL) designated by solid columns and the low salinity brine tests (LSB) designated by textured columns. 54
28. Scatterplot of average results of adhesion between the bare silica probe and a mica substrate in two different brines for six experiments (M-1, M-2, M-3, M-4, M-5, M-6). In three experiments (M-3, M-5, M-6), only the low salinity brine was used. Error bars show the standard deviation of the measurements. 56
29. Column plot indicating the number of specific features in approach curves (Figure 26) between bare silica probe and mineral grain in two different brines: formation liquid (FL) and low salinity brine (LSB). The x-axis indicates the type of feature and the y-axis indicates the number of times that feature occurred for an experimental set. The data includes two different experiments (R-1, R-2), in which multiple measurements were conducted at each of a few locations on the substrate. An additional set of R-2 data was collected over a grid of points and is designated (grid) in the plot legend. 58
30. Plots indicating the relative location of each force curve in a grid of points for experiment R-2. Each location is color-coded to indicate the features present in its approach curve (Figure 26). Curves were taken in formation liquid (A) and low salinity brine (B). 59

31. Average adhesion values (and standard deviation) between a bare silica probe and a mineral grain for two experimental sets (R-1, R-2). Points are color coded to indicate brine salinity and offset horizontally to indicate average values for multiple curves taken at each of 19 locations. The results are arranged chronologically from left to right along the x-axis. 60
32. Location dependent adhesion indicated by increasing circle area ranging from 0 nN adhesion (empty circle) to 4.6 nN adhesion (largest circle) in formation liquid solution (A) and low salinity brine (B) for the R-2 experiment. 60
33. Optical image of probe coated in dried crude oil clearly displaying interference patterns on the cantilever surface. 63
34. Relative change in resonance value for two probes as a function of coating the probes in wet crude oil and then drying them. Resonance values for the bare silica probe and wet oil coated probe are in the grey box. 64
35. Average pull-off force results from the retract curves of three experiments (Wet-1, Wet-2, Wet-3) with error bars to represent the standard deviations. Experiments performed in formation liquid are designated with black circles and low salinity brine are designated with red squares. In each case, multiple measurements were taken at each of multiple locations on the substrate (A). Additionally, each individual measurement is plotted for Wet-3. The boxes indicate which points were collected on each substrate location (B). 67
36. Approach curves collected from four dried “A” oil coated probes in two different liquid cell solutions (1 mM and 10 mM NaCl) on mica. 69
37. Approach curves collected in four experiments (B-Oil1, B-Oil2, B-Oil3, B-Oil4) from four dried “B” oil probes in two different liquid cell solutions, 1 mM (red) and 10 mM (black) NaCl. The plot placement indicates the order in which the experimental data was collected: from left to right, showing that some probes were tested in the same solution molarity twice. The box around B-Oil4 shows the four experiments that were performed with the same tip in the order 10 mM/1 mM/10 mM/1 mM. 71
38. Approach curves collected from three dried “C” oil probes in two different liquid cell solution molarities (1 mM and 10 mM NaCl). The order of the experiments is shown by the plot placement from left to right. For one experiment, C-Oil3, the same probe was tested five

- times in the following solution order:  
10 mM/1 mM/10 mM/1 mM/10 mM NaCl. Its experiments are  
designated by the surrounding black box. 73
39. Approach curves collected from five dried “C” oil coated probes in  
two liquid cell solutions (1 mM and 10 mM NaCl). The order of the  
experiments is shown by the plot placement from left to right. 74
40. Salinity dependent trends in adhesion between dry oil-coated  
probes and a mica substrate for three different experiments  
(MicaC-1, MicaC-2, MicaC-3). 76
41. The plots use the circle area to indicate the relative difference in  
adhesion for experiment MicaC-3 for the formation liquid (black  
circles in “A”) and low salinity brine (red circles in “B”) results. The  
adhesion ranges from 0 nN (empty circle) to 2.4 nN (largest circle in  
“B”). 77
42. Sample approach curve (A) taken with dried oil coated probe on a  
mineral grain. Schematic (B) of possible surface topography that  
could have contributed to each area of repulsion and snap-down in  
“A”. Both “A” and “B” have corresponding numbers to indicate what  
features might lead to each part of the approach curve. The arrows  
indicate the repulsion and attraction forces working on the probe  
from each surface feature. 79
43. Various features observed in the pull-off curves of force  
spectroscopy measurements taken on rough mineral grains.  
Features include steps (A), multiple pull-offs (B), and unexpected  
repulsion (C). 81
44. Complex retract curve between a probe with dried “A” oil coating  
and an “A” mineral substrate in 10 mM NaCl solution (black) and a  
model retract curve exhibiting a clean and sudden snap-off (red). 82
45. Adhesion between dried “A” crude oil coated probes and mineral  
grain substrates in three experiments (RoughS-1, RoughS-2,  
RoughS-3). The average adhesion value at each of multiple  
locations on the mica is represented by scatter points and the  
standard deviation is represented by the error bars. The  
chronological order in which the data was collected is demonstrated  
by the left to right ordering of the data. 84
46. Initial features in the approach curves for experiments RoughC-1,  
RoughC-2, RoughC-3, RoughC-4. These are the results of

measurements performed at each of five locations in both formation liquid (FL) and low salinity brine (LSB).	86
47. Approach curve features at each grid point for RoughC-2 including formation liquid (A) and low salinity brine (B).	87
48. Adhesion between four dry oil-coated probes and a mineral grain substrate with the average value of curves taken at five locations each for experiment (RoughC-1, RoughC-2, RoughC-3, RoughC-4) and salinity.	87
49. Grid plots show the results of experiment RoughC-2 for the formation liquid (black circles in "A") and low salinity brine (red circles in "B") with adhesion ranging from 0 nN (empty circle) to 2.5 nN (largest circle).	88
50. Adhesion for each force spectroscopy curve of experiment RoughC-1 between the dry oil-coated probe and an "A" grain. The black circles indicate formation liquid data and the red squares indicate low salinity brine data.	89
51. Adhesion for each force spectroscopy curve of RoughC-2 between the dry oil-coated probe and an "A" grain. The black circles indicate formation liquid data and the red squares indicate low salinity brine data. Linear fits in corresponding colors have been applied to show the gradually decreasing adhesion over the course of the experiment.	90
52. Individual adhesion measurements in two solution molarities for the dried "A" oil coated probe on mineral grain (experiment RoughC-3). The black circles indicate formation liquid data and the red squares indicate low salinity brine data.	91
53. Individual adhesion measurement for two solution molarities using a dried "A" oil coated probe on a mineral grain (experiment RoughC-4). The black circles indicate formation liquid data, the red squares indicate low salinity brine data, and the blue diamonds indicate a repeated experiment using the low salinity brine data. The total experiment was performed in the order low salinity brine, formation liquid, repeated low salinity brine.	92
54. Q-Q plot of the first and second data sets collected in low salinity brine in experiment RoughC-4.	94
55. Q-Q plots comparing each low salinity brine data set to the formation liquid data set in experiment RoughC-4.	95

56. Percentage of approach curves from each of three crude oil varieties that exhibited long range Repulsion (blue) or Attraction (red) in dried oil coated probe experiments. Curves in which the electrostatic force was too weak to detect are indicated by "No Force" (black). The "A", "B", and "C" crude oils are indicated by labeled columns. The experiments were performed in 1 mM and 10 mM NaCl solutions. 99
57. AFM DFL images of the surface of a bare colloidal silica probe (A), the same probe coated in amine (B), and coated in GO flakes (C). These scans indicate that the topography of the probe surface is not noticeably changed by adding the amine layer. 111
58. DFL images from contact mode of a bare silica probe (A), the same probe after being coated in GO (B) and each subsequent rinsing to remove loosely bound GO (C-F). 112
59. Probe before (A) and after (B) force spectroscopy experiments on PDMS. The surface features remain unchanged. 113
60. Force spectroscopy results of the snap-down (Approach) and pull-off (Retract) force for three probe surfaces (bare silica, amine coated and GO coated) on silanized mica. The Approach and Retract curve results are arranged in designated rows and the results from two different probes (A, B) are arranged in columns. In all cases, the y-axis indicates force (nN) and the x-axis indicates the individual force curve measurements. 115
61. Normalized and averaged approach snap-down (A) and retract pull-off (B) curve data for interactions between three GO probes and ten substrates. The error bars represent the standard deviations of the averages. 118
62. These AFM topography scans show the distribution of GO flakes on mica (A), silanized mica (B), and silicon (C). In these scans, "B" uses GOi, while "A" and "C" use GOh. 124
63. AFM topography scan of the very bumpy surface of the acrylic polymer closest to a mica substrate after curing. 125
64. GO on mica substrate before (A) and after (B) peeling. The exact same flakes are present in both AFM topography images with the addition of droplets of polymer residue. 126
65. GOi distributed on mica and then heated in an Ar environment to convert the GO into rGO (A). AFM images in "B" and "C" are the

same scan but with the contrast adjusted to make shorter features (rGO flakes) visible in the background (C) underneath the extensive acrylic residue.	128
66. GOi on silanized mica before (A) and after (B) peeling. Only one flake is clearly missing (circled in blue). There is also a lot of polymer residue remaining on the surface.	129
67. Silicon/GO substrate after peeling acrylic. Faint flake-like shapes are visible in the blue circles in addition to acrylic residue.	129
68. GO on silanized mica substrate before (A) and rGO after (B) peeling off a PI film. The GO was reduced to rGO in the polymer during curing. Blue circles indicate the same features in both scans.	131
69. Force modulation magnitude image of rGO flakes embedded in PI after being peeled off mica substrate during peeling test (A). There is a lack of rGO on silicon after peeling off the PI. Only visible droplets of polymer remain on the surface (B).	132
70. Approach (A) and retract (B) force spectroscopy data using a GO probe (from Figure 61) with silanized mica, mica, and polyimide results circled to highlight differences.	135
71. Graphic indicating the contact between two designs of alumina platelet probe: the angled platelet probe, i.e. where the platelet is flush with the cantilever, (A) and the parallel platelet probe, i.e. attached to a colloidal probe (B).	140
72. Optical image of Olympus inverted microscope with translation stage and SMENA tip holder in orientation to construct an alumina platelet probe.	142
73. Optical image of alumina platelets attached to AFM cantilevers with epoxy.	142
74. Contact mode vertical deflection (DFL) images of the triangular end of a bare cantilever (A) and an alumina platelet probe (B).	143
75. AFM phase images showing an alumina platelet on a mica substrate (A) and a similar platelet which has been dipped in a GO dispersion (B). The second platelet clearly shows GO flakes attached to its surface with none on the surrounding mica.	144
76. Initial (A) and repeated (B) force spectroscopy measurements between angled alumina platelet probe and substrates. The black	

circles indicate the average retract curve adhesion and the red squares indicate the average approach curve attraction. The error bars are standard deviations of the averages.	145
77. Raw lateral force images for friction measurements on mica (A, B) and silanized mica (C, D) in the forward (A, C) and backward (B, D) scan directions.	148
78. Subtracted images of mica (A) and silanized mica (B). The average values for each image are 17.01 pA for mica and 12.81 pA for silanized mica.	149
79. Raw AFM lateral force scans on mica (A, B) and silanized mica (C, D) in the forward (A, C) and backward (B, D) scan directions.	150
80. Subtracted LF images of mica (A) and silanized mica (B). The average values for the two images are 5.34 pA for mica and 3.12 pA for silanized mica.	150
81. Reflective brightfield (A), darkfield (B), differential interference contrast (C), and transmission (D) images of crude oil on glass. The same location is shown in both "A" and "B".	160
82. These images show the varied sizes and shapes of features that we have observed. Images in "A" and "B" show the different range of size features that we have seen. Those in "B" were found in crude oil that was mixed with toluene and centrifuged.	161
83. Same crude oil droplet on glass before (A) and after (B) drying. Some features near the edge of the droplet are immobilized as the oil dries (B).	162

## **Chapter 1: Introduction and Theory**

### **a. Research Objectives**

Surface interactions govern many aspects of colloids, nanocomposites and other systems. Although the same forces are at work in all colloidal systems, the unique situations of each system, e.g. different molecules, sizes, ions in solution, and temperature, lead to a wide variety of resulting interactions.<sup>1</sup> Consequently, in many important systems, these interactions are still not well studied, which limits our capabilities to improve them. We use force spectroscopy<sup>2–4</sup> to measure forces between surfaces in two distinct but important examples: oil recovery and polymer nanocomposites. We functionalize force spectroscopy probes to directly and quantitatively measure forces between two surfaces. Due to the micro- to nanometer length scale on which these forces interact, this is one of the only ways to study these interactions.<sup>5</sup> These probes allow us to directly observe the relationship between the experimental conditions of the system and the resulting surface forces.

In chapter 1 of this dissertation, we first introduce the technique of atomic force spectroscopy and previous work with functionalized probes. Next, we address the theory of fundamental surface interactions in the context of force spectroscopy experiments that are relevant to our research. We also provide relevant background information on oil recovery and polymer nanocomposites. In chapter 2, we introduce our experimental methods, including the method to manufacture a basic colloidal probe. We present our work using a crude oil coated probe in an aqueous environment

(chapter 3), which introduces predictive capabilities to improve the efficiency of oil recovery. To advance the design of nanocomposites, we introduce two other custom probes that incorporate graphene oxide (chapter 4) and alumina (chapter 5). In the conclusion, we summarize our results and suggest next steps for future experiments using these custom probes (chapter 6). In the appendix, we include a small report on the characterization of some unexpected structures that we identified in crude oil.

## b. Background

### b.1. Atomic Force Spectroscopy

Atomic force spectroscopy<sup>2–4</sup> provides a method of quantitatively measuring the interactions between two materials: a probe and substrate. This technique is one of few methods capable of measuring forces on the micro– to nanometer length scale. It makes localized force measurements possible so that the probe and substrate materials can be varied to simulate different systems.<sup>5</sup> To perform measurements, a tip that is only a few nanometers to a few microns in diameter is located at the end of a flexible microscopic cantilever. The tip and cantilever comprise the probe.<sup>6</sup> In many types of force spectroscopy experiment, a piezoelectric transducer—which confers sub-nanometer positional accuracy—is used to vertically approach the probe toward the substrate surface.<sup>7</sup> As the tip approaches the substrate from above, interactions between the tip and substrate cause the cantilever to bend upward if the forces are net repulsive and downward if the forces are net attractive. A laser reflected off the back of the cantilever

and onto a photodiode shifts slightly as the cantilever deflects. This shift, which is directly tied to the tip-sample interaction, is recorded.<sup>7</sup>

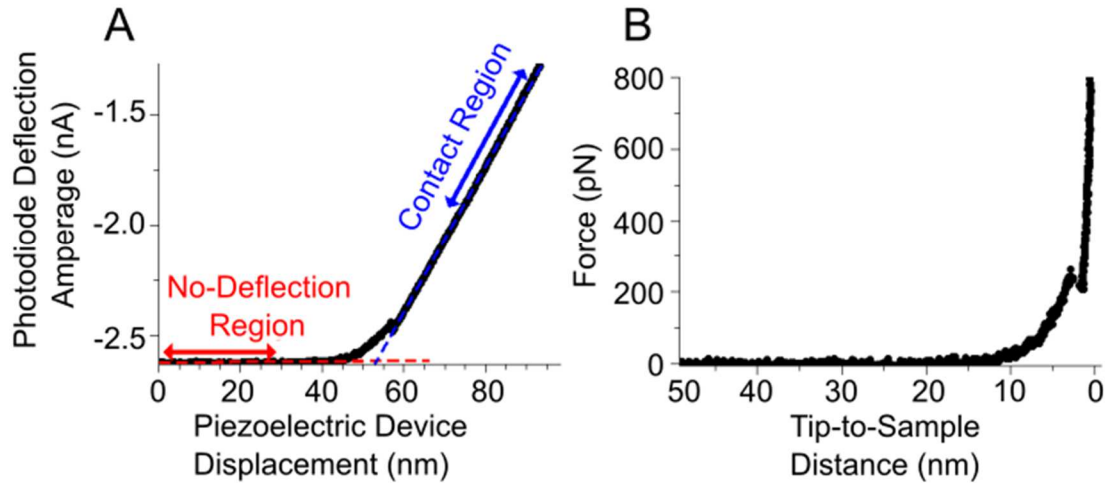


**Figure 1 Sample force spectroscopy curves: a raw deflection-displacement curve (A) and a processed force vs. tip-to-sample distance curve (B).**

To visualize the tip–sample interactions in this process, we plot the deflection of the laser along the photodiode (units: nA) as a function of the vertical piezoelectric device displacement (units: nm) (Figure 1A).<sup>5,8,9</sup> In this case, the photodiode is composed of quadrants which provide a differential photo current based on how much of the total laser signal is present in different areas of the detector. For example, as the laser moves vertically along the detector, the difference in laser signal between the top and bottom halves of the quadrant photodiode produces a differential current which indicates the deflection of the laser beam.<sup>7</sup> Sometimes raw deflection–displacement data provides the most information about a particular experiment and/or it is not possible to process the curves further. If we are interested in analyzing the true tip–sample forces and

distances, this raw deflection–displacement data becomes more useful once it is converted into force vs. tip-to-sample distance data (Figure 1B). To convert the raw data, a few assumptions must be made. One assumption is that a cantilever is in contact with a surface that is stiff enough to resist probe indentation. In this case, the cantilever bends in direct proportion to the vertical extension of the piezoelectric transducer.<sup>5</sup> Based on this assumption, in the contact region (indicated by the blue arrow in Figure 1A) each nanometer of vertical piezoelectric transducer extension ( $x$ -axis) should correspond to a nanometer of cantilever deflection ( $y$ -axis). In other words, we can scale the  $y$ -axis values of this region to equal one.<sup>5</sup> This effectively converts the photodiode deflection current (nA) to cantilever deflection (nm). In the hypothetical situation in which no electrostatic or van der Waals forces between the tip and sample are experienced, the deflection transitions directly from zero deflection, i.e. the no-deflection region, to the contact region, i.e. where the tip touches the surface.<sup>5</sup> Once the tip touches a rigid surface, the cantilever begins to bend since the Pauli exclusion principle prevents the atoms in the tip from penetrating between the atoms of the substrate. There are some electrostatic or van der Waals forces present in most cases, however, so to approximate the point where the tip first touches the surface, we use the intersection of fit lines applied to both the no-deflection region and the contact region (intersection of blue and red dotted lines in Figure 1A).

To convert from piezoelectric displacement to tip-to-sample distance, we simply add the cantilever deflection (nm) to the piezoelectric device displacement (nm).<sup>5</sup> This step compensates for the additional change in distance due to the cantilever deflection prior

to contacting the surface, e.g. greater distance for a repelled probe and smaller distance for an attracted probe. As a final step, we multiply the cantilever deflection (nm) by the spring constant of the cantilever (N/m) and scale it by 1000 to yield units of force (pN) (Figure 1B).<sup>5</sup> Although this final step is very straightforward mathematically, it can introduce significant errors to the resulting force values. The reason for this is the large error associated with the cantilever spring constant. These values can be dramatically different from the nominal value indicated by the manufacturer.<sup>7</sup> Consequently, to obtain accurate force measurements it is vital that these cantilevers be calibrated in-house using a calibration method<sup>7,10-12</sup> such as the Sader Method.<sup>13</sup> These measurements can be performed in vacuum, air, and liquid environments, allowing a wide variety of systems to be studied.<sup>4,5,9,14,15</sup> Beyond the basic mechanics of performing and calibrating force spectroscopy measurements, there is the complex task of interpreting them. Since the results are a function of the experimental scenarios being tested, many past studies have focused on the interpretation of force curves in different specific situations. For example, adhesion,<sup>6,16</sup> environmental conditions<sup>5,9,17</sup> etc.,<sup>18-21</sup> all impact the force spectroscopy results.

Sharp-tipped (<20 nm diameter) probes are commonly used to obtain sufficient resolution during imaging. However, they can easily break, and their geometry is often not well defined. Although sharp probes are employed in some force spectroscopy experiments,<sup>22,23</sup> colloidal probes are an attractive alternative. A colloidal particle has a larger diameter (>1  $\mu\text{m}$ ), making it more robust and its geometry more predictable. A more defined geometry of a sphere interacting with a plane makes the system easier

to model. Additionally, a bigger probe provides a larger interaction area with the substrate, yielding a greater force to measure, and a reduction in the depth of deformation compared to a sharp probe.<sup>24</sup>

Colloidal probes can be constructed in a lab with an optical microscope and a micrometer translation stage, with no etching or evaporation equipment required.<sup>6</sup> Any spherical or semi-spherical material of a few microns in size can be attached to a tipless cantilever using adhesive. Epoxy is commonly used to attach the spheres,<sup>6</sup> although non-adhesive methods have also been employed.<sup>25</sup> Researchers have used spherical materials made from borosilicate glass,<sup>25</sup> silica,<sup>26–30</sup> polymers,<sup>31</sup> and alumina.<sup>29</sup> Some have even used semi-spherical materials, such as illite clay particles.<sup>32</sup> These probes can also be coated with individual functional groups,<sup>22,23</sup> petroleum and its components,<sup>33–38</sup> and polymers.<sup>39</sup> Functionalizing sometimes requires specialized equipment, e.g. to grow graphene onto the probe,<sup>40</sup> or can be as simple as dipping the probe in a droplet of liquid. In all cases, functionalization expands the number of options available to explore the interactions between two materials.

## b.2. Fundamental Interactions

Correctly interpreting the force measurements between the probe and substrate requires an understanding of the interaction forces. These interactions can be influenced by the probe and substrate geometries, material properties, and the properties of the surrounding medium, to varying degrees. We worked predominately with a spherical, colloidal probe and planar substrate in our experiments, a system that has been described by multiple reviews.<sup>5,9,6,17</sup> Therefore, we will only briefly explore the

relevant forces, electrostatic and van der Waals forces, to show how they affect our experiments.

### b.2.1. Electrostatic Forces

Electrostatic forces occur between two objects with charged surfaces, which may either be polar or nonpolar. In a vacuum, Coulomb's law shows the force between two charged points:

$$F(D) = \frac{1}{4\pi\epsilon_0} \left( \frac{Q_1 Q_2}{D^2} \right) \quad (1)$$

where  $F$  is the force between the points,  $Q_1$  and  $Q_2$  are the charges on the two points,  $D$  is the distance between them, and  $\epsilon_0 = 8.854 \times 10^{-12} A s V^{-1} m^{-1}$  is the permittivity of free space.<sup>41</sup> Note that for oppositely charged particles,  $F$  will be negative, indicating an attractive force. This equation can be modified to describe the sphere/plane geometry we employed in our AFM experiments. By assuming perfectly smooth conducting materials with an even distribution of charge on their surfaces, researchers have modeled these interactions after a capacitor system of the same geometry:

$$F(D) = \frac{-\epsilon\epsilon_0\pi RV^2}{D} \quad (2)$$

when  $D \ll R$ .<sup>42-44</sup> Here,  $R$  is the radius of curvature of the colloidal probe,  $D$  is the separation distance between the probe surface and planar surface,  $V$  is the applied voltage, and  $\epsilon$  is the dielectric constant of the medium. Since our colloidal probes have tips that are microns in diameter and our AFM piezoelectric device can only separate the probe and substrate by a few microns, this equation where  $D \ll R$ , is valid in most cases. However, in the case of  $D \gg R$ , the force-distance equation becomes:

$$F(D) = \frac{-\varepsilon \varepsilon_0 \pi R^2 V^2}{D^2} \quad (3)$$

Additionally, in a vacuum, the dielectric constant  $\varepsilon$  of the surrounding medium is equal to 1, further simplifying the equation.<sup>5,9,45–48</sup> To demonstrate how these forces might change as a function of surface charge, a sample spectroscopy scenario is modeled below (Figure 2). Here, two different voltages, 20 mV and 200 mV, are applied between the probe and sample, and the anticipated force-distance results are plotted. The squared voltage variable in the electrostatic force equation indicates the significant influence of the applied voltage on the resulting force. In the case of a force spectroscopy experiment, this applied voltage relates to the amount of surface charge on the probe.

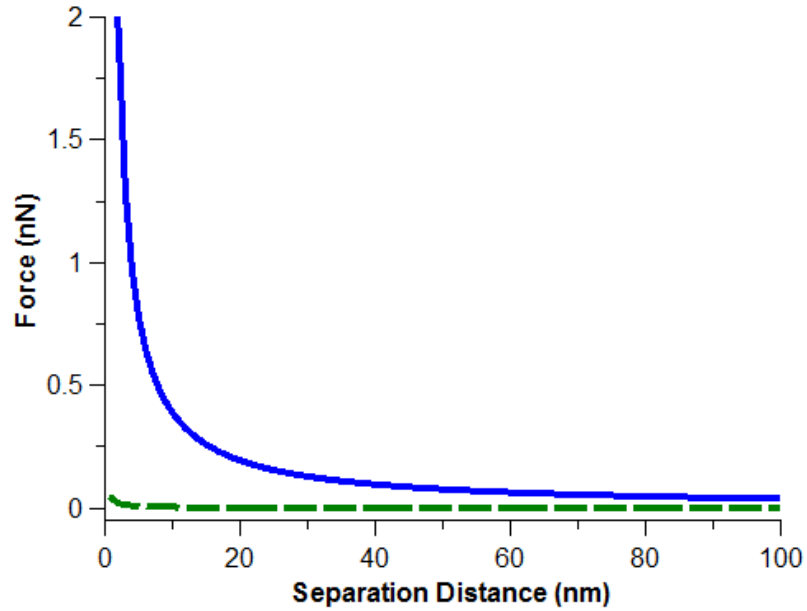


**Figure 2** Theoretical effects of differing applied voltage (dashed green line: 20 mV and solid blue line: 200 mV) on electrostatic force trends.

All of our experiments were performed in either air or aqueous solution. Substituting  $\epsilon \approx 1$  for experiments in air into (2)<sup>42</sup> shows that the force relationships in air and in vacuum are approximately equivalent. However, humidity is often present in air, which can reduce electrostatic interactions.<sup>5</sup> This effect can be advantageous if van der Waals forces are of most interest, as a reduction in the electrostatic charge makes van der Waals attraction more visible in the force curves. Due to its effect, humidity should be considered as an important environmental variable when comparing force measurements.

Performing force spectroscopy experiments in an aqueous solution introduces its own challenges. Depending on the isoelectric point of the surfaces, the probe and substrate may develop either a positive or negative charge due to the dissociation of surface groups, chemical reactions, or ion adsorption. The newly charged surfaces then attract ions of the opposite charge in solution. The highest concentration of ions forms closest to the charged surface, but this concentration decreases as a function of distance from the surface. These ions form a dynamic layer that is constantly moving and rearranging as a function of thermal fluctuations. Additionally, the ion cloud acts as a screening mechanism that leads to an exponential decrease in electrostatic force as a function of distance between two charged surfaces. This phenomenon is described by the DLVO theory or electric double layer theory and requires a separate equation to model the force-distance interactions.<sup>49,50</sup>

Although the equations for the double layer force vary based on geometry, they all exhibit an exponential decay of force with separation distance and they all employ a

characteristic decay constant: the Debye length.<sup>41</sup> For a sphere-plane geometry between two equipotential surfaces where  $D \ll R$  but  $D$  is equal to or larger than the Debye length, the double layer force can be approximated to be

$$F = \kappa R Z e^{-\kappa D} \quad (4)$$

Here  $\kappa^{-1}$  is the Debye length,  $e$  is the charge of an electron, and  $Z$  is defined by Israelachvili as an “interaction constant” which groups together all the constants related to the surface features<sup>41</sup>:

$$Z = 64\pi\varepsilon_0\varepsilon \left(\frac{kT}{e}\right)^2 \tanh^2\left(\frac{ze\psi_0}{4kT}\right) N \quad (5)$$

where  $z$  is the valency of ions in solution,  $k$  is Boltzmann’s constant,  $T$  is temperature, and  $\psi_0$  is surface potential.<sup>41</sup> The equation for the Debye length is:

$$\kappa^{-1} = \left( \sqrt{\sum_i \frac{\rho_{\infty i} e^2 z_i^2}{\varepsilon \varepsilon_0 k_B T}} \right)^{-1} \quad (6)$$

where  $\rho$  is the molarity of ions in solution.<sup>9</sup> This equation shows that as the ion concentration increases, the Debye length will decrease. The Debye length will also be less for multivalent ions than for monovalent ions. Therefore, calculating the Debye length for a set of experimental conditions is essential to correctly interpreting the data. If we assume that solution composition, solution temperature, and probe diameter are all constant, we can approximate the electrostatic repulsion as a simple exponential:

$$F = A e^{-\kappa D} \quad (7)$$

where  $A$  is the amplitude. Fitting this equation to our data allows us to measure the force between the colloidal probe and substrate. It will also highlight any unexpected

changes that might be occurring to the solution composition or surface chemistry during the experiment.

### b.2.2. van der Waals Forces

Van der Waals forces occur between the three different types of dipoles: permanent-permanent, permanent-induced, and spontaneous-induced.<sup>51</sup> Consequently, they are greatly affected by the material properties of both the surfaces, the surrounding medium, and the geometries of the interacting components.<sup>41,51</sup> In the case of a spontaneous-induced dipole, there is a lag in time between the formation of the spontaneous and induced dipoles, leading to a more rapid decay in interaction force. Consequently, there are two categories of van der Waals equations based on the separation distance  $D$  between the two interacting surfaces: a “normal” equation for  $D < 10$  nm and a “retarded” equation for  $D > 20$  nm to compensate for the effect of spontaneous-induced dipoles. Between these two distances, the trends of the forces are not well defined because the resulting interactions are a combination of these two distinct regions.<sup>52</sup> In the case of a sphere-plane geometry, the equation at small separation distances<sup>41,52</sup> is

$$F = -\frac{A_H R}{6D^2} \quad (8)$$

and the retarded equation at larger separation distances is<sup>52</sup>

$$F = -\frac{2\pi B R}{3D^3} \quad (9)$$

where  $A_H$  is the Hamaker constant and  $B$  is the retarded Hamaker constant. As (8) and (9) indicate, the equation for van der Waals forces is dependent on the Hamaker

constant, which in turn depends on the properties of the two interacting materials and surrounding medium.<sup>41</sup>

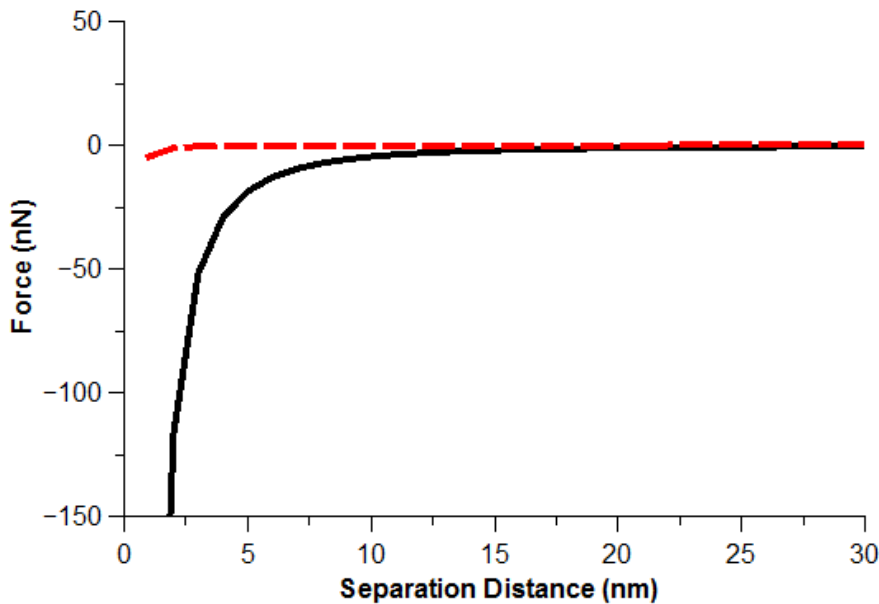


**Figure 3 Effect of two different Hamaker constant,  $A_H$ , values on the attractive van der Waals forces. The solid black line designates  $A_H = 40$  (vacuum) and the dashed red line designates  $A_H = 0.4$  (water).**

The effect of the Hamaker constant, which typically ranges from 0.46 to 49,<sup>5,53</sup> can be observed in a model system (Figure 3) for the normal van der Waals equation (8). When force spectroscopy experiments are performed in an aqueous solution ( $A_H = 0.4$ ), the strength of the van der Waals force is much lower than in a vacuum ( $A_H = 40$ ). This is due to the highly polarizable nature of water. As the water molecules orient themselves according to the orientation of the dipoles in the two surfaces, the effect of the dipoles is effectively screened, weakening the attraction between the surfaces.

### b.2.3. Combination of Interactions

Because electrostatic and van der Waals forces exhibit different distance dependencies, the colloidal probe will encounter regions of either electrostatic or van der Waals dominance as it approaches a substrate. After the probe contacts the substrate, adhesion combines the effects of van der Waals and electrostatic forces. These interactions are further complicated by many variables. Greater contact area between the two surfaces will lead to greater adhesion. Consequently, the roughness and topography of both the substrate and probe will significantly impact the results. Some theories model adhesion to include only the contact area,<sup>54</sup> while others include surrounding parts of the surfaces that are close enough to be influenced by interaction forces.<sup>6,55</sup> Consequently, some models would treat the geometry of an infinitely sharp probe, represented by a single column of atoms, differently from a spherical probe. Both might have the same contact area, i.e. a point contact, but the spherical probe has a larger curved area that is still close enough to the substrate to be influenced by the van der Waals and electrostatic forces.

Deformation of the surfaces leads to multiple complications, including increased contact area. Additionally, it complicates curve processing by making it difficult to determine when the probe contacts the substrate. Depending on the type of deformation, plastic or elastic, and its viscoelastic properties the resulting force measurement can also change based on how quickly the probe approaches the surface and its contact time with the surface.<sup>6</sup> For samples exhibiting viscoelastic properties, the contact time will increase the adhesion.<sup>6</sup> For samples exhibiting plastic

deformation, the amount of force applied will affect the adhesion.<sup>6,56</sup> Some important theories, JKR,<sup>54</sup> DMT,<sup>55</sup> and Maugis-Pollock<sup>56</sup> model the adhesion interaction based on elastic vs. plastic surface deformation and contact area.<sup>6</sup> Careful preparation and choice of the probe and substrate materials can reduce the effects of some of these variables on adhesion measurements. In addition, researchers may design their experiments to maintain constant probe/substrate approach speed, applied force, and contact time to further reduce complications.

The combined effects of van der Waals and electrostatic forces in a medium can also lead to differences in adhesion. Adhesion measurements in air have a complex relationship with humidity. For a sample with excess surface charge, a humidified environment can be used to reduce the charge, decreasing the electrostatic forces and adhesion. However, too much humidity can also form water layers on polar surfaces. These layers result in capillary forces between the probe and substrate, which can increase the adhesion.<sup>6,47,57,58</sup>

In an aqueous solution, changing ion concentration will affect the strength of the electrostatic forces. This can also modify the adhesion. In some adhesion models, the electrostatic forces can act on the parts of the spherical probe that do not make contact with the substrate.<sup>6,55</sup> Therefore, even though the ion concentration has no effect on the van der Waals forces within the contact area of the probe/sample, the adhesion can still change. All of these aspects are important to consider while designing an experiment, especially since the many of the variables are interdependent.

### **c. Investigated Systems**

Our experiments involved the design and use of force spectroscopy probes to study force interactions in two important fields: oil recovery and nanocomposites. In the following section, we provide motivation, background information, and our experimental approach for each topic. By modeling and predicting outcomes in relevant environmental scenarios, these probes can be used to increase the efficiency of technological advance in these two fields.

#### **c.1. Petroleum Reservoirs**

Oil is a vital resource in the world economy. However, current oil extraction techniques remain inefficient. After a well is initially tapped and the primary volume of pressurized oil and natural gas is collected, engineers turn to secondary recovery methods to extract the non-pressurized reserves. A popular method is water injection, which artificially increases the pressure in the reservoir and pushes oil to the surface.<sup>59</sup> However, even after water injection, much of the oil remains trapped in rock pores and adhered to rock surfaces.<sup>60,61</sup> An enhanced understanding of the interactions between oil and rock in an aqueous environment would make it possible to introduce compounds to the injection liquid and modify these interactions to allow for more efficient oil extraction. Thus, our work focuses on understanding the interactions between the oil and mineral surface.

To manipulate the interfacial forces holding the oil within the reservoir, some researchers have studied the effects of different compositions of salt solution as the

injection liquid.<sup>62–64</sup> However, the results have been inconsistent among reservoirs.<sup>65–</sup>

<sup>68</sup> Determining the reasons for these inconsistencies is complicated by the heterogeneous chemical nature of the oil from various reservoirs and the rough topography of the mineral grains.<sup>59,69–71</sup>

Typically, research in this field has used core flooding experiments and spontaneous imbibition tests to observe the oil-substrate interactions as a function of pH, temperature, and ion composition of the surrounding aqueous solution.<sup>61,72–81</sup> However, since these methods inherently test the average result over many mineral grains and species, it can be difficult to determine which substrate components have the greatest effect. Some researchers have addressed this ambiguity by conducting contact angle measurements using different petroleum-derived species on a single mineral surface such as kaolinite, mica, silicon or silica. In these tests, the effects of solvents,<sup>82</sup> surfactants,<sup>83</sup> pH,<sup>30,36,84–87</sup> different types of petroleum,<sup>88</sup> and ion composition were measured.<sup>30,36,84–87</sup> Although these experiments provide useful knowledge regarding interfacial energies,<sup>41</sup> they do not give more specific information on how the forces behave over distance. Also, contact angle studies require large, flat substrates, which limits the number of materials available for testing.

In contrast, force spectroscopy provides a quantitative method for measuring these interaction forces as a function of distance and requires an area many orders of magnitude smaller on which to perform a measurement.<sup>9</sup> Additionally, this method can be performed in an aqueous environment, allowing the simulated injection liquid to be modified during the experiment to test the effect on the oil-mineral interaction forces.

In these force spectroscopy experiments, the two surfaces—probe and substrate—can be chosen to represent the reservoir mineral and oil, respectively. For example, some researchers employed a tip material that reflects the reservoir mineral by using a spherical silica bead<sup>27,28,30</sup> or semi-spherical illite<sup>32</sup> particle. However, this approach limits the mineral options that can be explored since not all reservoir minerals are available as spherical particles.

Functionalizing a colloidal probe to represent the crude oil and using a reservoir mineral as the substrate greatly increases the available experimental options. Some researchers used this design by functionalizing their probes with chemical groups ( $-\text{CH}_3$ ,<sup>22</sup>  $-\text{COOH}$ <sup>22,23</sup>), representative chemicals (*n*-decane,<sup>27</sup> octadecane<sup>33</sup>), or petroleum subsets (asphaltenes,<sup>35,38</sup> bitumen,<sup>36,37</sup> resin<sup>35</sup>) and conducting force spectroscopy measurements on mica,<sup>22,33,34</sup> sandstone,<sup>23</sup> silicon,<sup>22</sup> illite,<sup>22</sup> or glass.<sup>34,35</sup> One group even used crude oil to make the experiment more similar to the actual reservoir interactions, but they reported problems with the oil pulling off the probe whenever the probe made contact with the surface.<sup>33–35</sup>

Our approach involved functionalizing a colloidal probe with crude oil and then drying the crude oil to create a customized AFM probe. By drying the oil, we created a more robust coating that remained attached to the probe throughout the measurements. This customized probe allowed us to measure the interfacial forces between crude oil and rocks from the same reservoir—a more accurate, reservoir-specific method for measuring and improving oil recovery efficiency.

## c.2. Polymer Nanocomposites

Nanocomposites promise a new era of enhanced structural materials. These materials unite the remarkable mechanical properties of a nanomaterial, such as graphene, with the low density of the composite polymer, to produce compounds that are both strong and lightweight.<sup>89–92</sup> The study of different nanomaterial-polymer combinations is crucial, for the bond between the polymer matrix and nanofiller is responsible for the improved strength of the bulk material. If this bond is weak, the nanocomposite will fail at the matrix-filler interface whenever stress is applied, and the material will fail to achieve the desired mechanical properties of its constituents.<sup>89,93</sup>

The adhesion between the matrix and filler is therefore an imperative issue in this field, but it remains difficult to quantitatively measure.<sup>94</sup> This problem is difficult to address. Since the nanofiller is embedded in the matrix, it is difficult to access the interface to perform adhesion measurements. Additionally, manufacturing defects such as bubbles or cracks in the polymer often obscure the effect of the nanofiller. Our work focuses on the interactions between graphene oxide (GO), an extremely promising nanofiller in nanocomposite development, and various polymers. The functional groups found on GO make it a polar material that is easier to disperse in organic solvents than graphene. Consequently, this makes it easier to incorporate into polymers for industrial applications.

In order to understand the interactions between GO and each tested polymer, we functionalized a colloidal probe with GO sheets and used the probe to perform force measurements on various polymer substrates. This method allowed us to predict which

material combinations would result in the greatest adhesion, and consequently, the greatest strength. Although other researchers have explored this technique using tips functionalized with carbon nanotubes<sup>95–98</sup> and graphene,<sup>40</sup> they did not test the effect of GO. Additionally, they did not use colloidal probes, so the interactions in their experiments were not as easily modeled. Our GO-functionalized colloidal probe thus provides a unique ability to directly measure the interactions occurring within a GO-polymer nanocomposite.

## **Chapter 2: Experimental Methods**

### **a. Equipment**

#### **a.1. Atomic Force Microscopy**

##### **a.1.1. Model and Usage**

All of our imaging and force spectroscopy experiments were performed with an NT-MDT NTEGRA AFM (Controller model: P9). The complementary NT-MDT components included a SMENA head, Universal head, and the SMENA liquid cell (Model: MP3LCNTF). We processed the scan images by using the NT-MDT programs NOVA and NOVA\_Px in addition to the free software Gwyddion ([gwyddion.net](http://gwyddion.net)). We also developed custom Python programs to process the force spectroscopy data. To characterize the surfaces of the substrates, we collected images in both contact and dynamic modes. Contact mode provides three important pieces of information: a topography (Height) image, the vertical deflection of the cantilever (DFL) and the lateral deflection of the cantilever (LF). All three signals are beneficial to our work because they provide information on the magnitude of the topography of the sample (Height), features with sharp edges (DFL), and areas of differing friction (LF). The dynamic mode also outputs three signals to detect the topography (Height), sudden changes in the surface forces (Mag), and localized areas of differing surface interactions (Phase). The Phase image is of particular use in the dynamic mode because it can distinguish different materials that exhibit similar surface topography.

When using our custom AFM colloidal probes, we performed force spectroscopy measurements in both air and aqueous solutions. In tests performed earlier in the research, after landing the probe on the substrate we collected multiple measurements on the same location before moving the probe to another area and repeating the measurements. Over time, we switched to performing measurements on a grid where one measurement was collected at each location. We determined that performing measurements in a grid pattern helped to average over any surface heterogeneities, providing a more representative set of measurements for the interactions between the probe and substrate. In the following chapters the method of data collection for each experiment is identified. In cases where we used aqueous solutions, we switched between brines by flushing the liquid cell with 3 mL of the subsequent brine 6–8 times. We also used a new disposable pipette tip with each rinse to avoid contaminating the experimental setup.

### a.1.2. Data Analysis

The details for processing a raw force spectroscopy curve were described in the Introduction. However, after processing the curves we needed to perform additional analysis to measure the interactions. In the approach curves, we focused on two different aspects: electrostatic repulsion in a liquid environment and van der Waals attraction, indicated by a snap-down of the probe close to the surface. As described in the Introduction, in an aqueous solution we expect electrostatic forces to exhibit the exponential trend:

$$F = Ae^{-\kappa D} \quad (10)$$

Here  $A$  is the amplitude ( $y$ -intercept of the curve),  $\kappa$  is the Debye length, and  $D$  is the tip-to-sample distance. Figure 4 shows an example of a processed approach curve that exhibits both long range electrostatic repulsion (blue box in Figure 4) and a sudden snap-down due to close range van der Waals attraction (pink box in Figure 4). In this type of curve, i.e. with both electrostatic repulsion and a snap-down, determining the region in which to apply an exponential fit is straightforward (blue fit line in Figure 4). In contrast, some curves exhibit no snap-down. Instead the repulsion curve gradually becomes non-exponential close to the surface, where the van der Waals attraction is dominant. For these curves, we apply fits that avoid the region within the first few nanometers of the surface and confirm that the exponential fit line is centered within the scatter points.

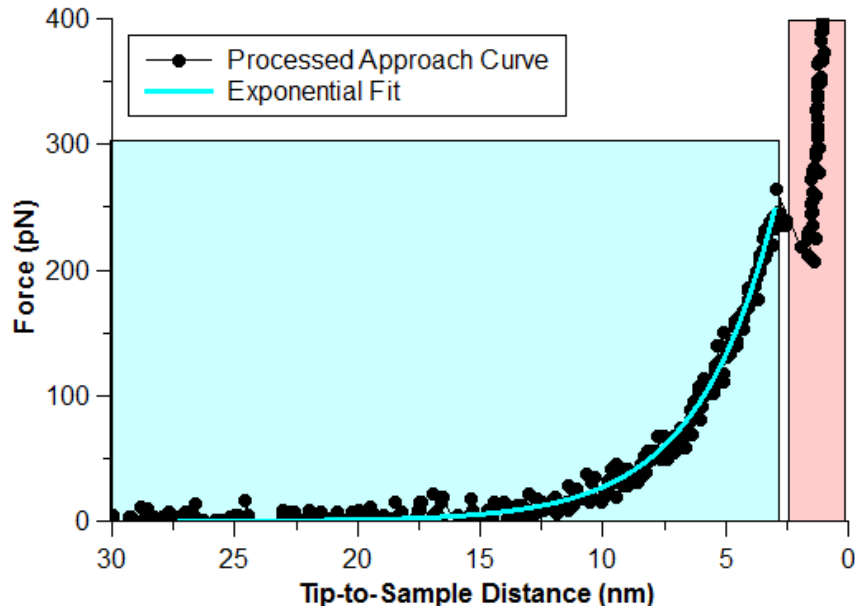


**Figure 4 Sample processed approach curve with an exponential fit applied to the electrostatic repulsion region. Blue and pink boxes indicate the regions dominated by electrostatic repulsion and van der Waals attraction, respectively.**

If the van der Waals snap-down occurs when the cantilever is still experiencing a net upward deflection, above the no-deflection region, as in Figure 4, we have calculated the net van der Waals attraction to be zero for the purposes of comparison. In some cases, the snap-down of the van der Waals attraction extends below the level of the no-deflection region, which indicates a net downward deflection of the cantilever. In these cases, we measure the van der Waals attraction in the approach curve and the adhesion in the retract curve in the same way: the maximum downward deflection of the cantilever from the non-deflected state, i.e. no-deflection region. For example, in Figure 5 the adhesion is approximately 2 nN (indicated by the vertical range of the red arrow). If this was an approach curve instead of a retract curve, we would measure the snap-down in exactly the same method (as 2 nN). Since these measurements are only

performed with respect to the vertical deflection of the cantilever, it is unnecessary to perform the last step of the force curve processing, where the  $x$ -axis is converted from piezoelectric device displacement to tip-to-sample distance.

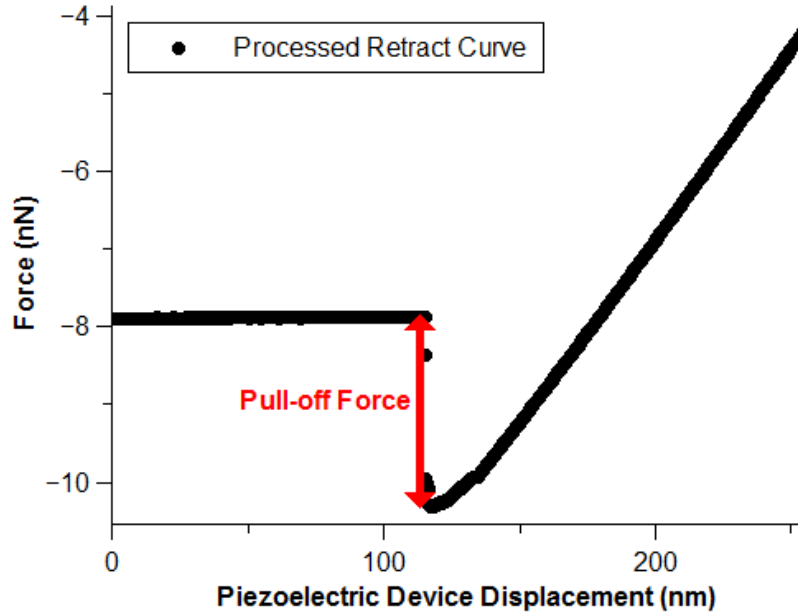


**Figure 5** Sample processed retract curve with red arrow to indicate the adhesion measurement, e.g. Pull-off Force. Similarly, in an approach curve we would measure the same vertical region of the Snap-down to show the maximum downward deflection from the non-deflected state of the cantilever.

## a.2. Other Laboratory Equipment

To perform our experiments, we used a variety of commercially available equipment which can be categorized by function: optical analysis, heat treatment, AFM probe preparation, substrate preparation, and solution preparation. We performed optical analysis of samples and probes using the Olympus inverted microscope (Model: IX71) and Nikon stereomicroscope (Model: SMZ800). In particular, the Olympus microscope contained multiple objectives MPLFLN-BD 5 $\times$  (0.15 NA), MPLFLN-BD

$20\times$  (0.45 NA), MPLFLN-BD  $100\times$  (0.9 NA), and LUCPLFLN,  $40\times$  (0.6 NA) with options for bright field, dark field, and differential interference contrast. We performed heat treatments on samples using ovens (Thermo Scientific Lindberg Blue M V0914A vacuum oven and Thermolyne 47900 furnace) and a hot plate (Fisher Scientific, Isotemp). During AFM probe construction, we worked with two different translation stages (Newport Corporation XYZ translation stage, Model #: 460-XYZ and Siskiyou Corporation hydraulic micromanipulator, Model #: MX6600R) and a vacuum desiccator (Fisher Scientific). For substrate preparation, we utilized the Laurell WS-400Bz-6NPP-Lite Spin Processor (spin coater) and balance (Fisher Scientific, model # SI-64). In addition, all solutions were made utilizing the Millipore UV water filtration system (Synergy). In cases where we took pH measurements, we used the Oakton PH/CON 510 pH meter.

## **b. Materials for Probes and Liquid Cell Solutions**

Most of the essential materials that we used for our force spectroscopy experiments involved components for the functionalized probes and liquid cell solutions. To construct our AFM probes, we relied on various types of tipless cantilevers from Mikromasch (model: CSC12 uncoated), Bruker (model: MLCT-O10 coated silicon nitride), and NanoAndMore (model: All-In-One tipless aluminum coated). We also used two different epoxies from Ace Hardware (5 Minute Quick Set Epoxy and Marine Epoxy), and microspheres from Cospheric (solid soda lime glass microspheres, mean diameter: 8–12  $\mu\text{m}$ ) and Bangs Laboratories (non-functionalized silica spheres, mean diameter: 7.27  $\mu\text{m}$ ).

Depending on the project, we functionalized the probes with an amine (Gelest, (3-trimethoxysilylpropyl) diethylenetriamine), GO flakes (lab of Dr. David Kranbuehl, Chemistry department, The College of William & Mary), alumina platelets (Merck, Ronaflair® White Sapphire) and crude oils (Shell Global Solutions International). To reduce contamination and degradation, the three oil samples that we received were collected from the well head and stored in dark glass bottles with argon or nitrogen blankets away from sunlight. Further details of the chemical composition and origin of the oils is proprietary. Therefore, we simply refer to them by assigned letters, i.e. “A” oil, “B” oil, and “C” oil.

We made an assortment of brines for our liquid cell solutions. Some used only one salt variety, i.e. simple brines, in the concentrations of 1 mM, 10 mM, 100 mM, and 1 M. For two other brines, i.e. complex brines, we used recipes from Shell Global Solutions International to simulate the connate brine (formation liquid) and injection liquid (low salinity brine) for a particular reservoir. The exact ratios of each of the four salts (calcium chloride, sodium chloride, potassium chloride, magnesium chloride) in these brines are proprietary, however, the molarities of the resulting solutions are approximately 4 M (formation liquid) and 28 mM (low salinity brine). We made all brines from Synergy UV Millipore water and the following salts: 99+% for analysis potassium chloride (ACROS ORGANICS), 99+% for analysis calcium chloride dehydrate (ACROS ORGANICS), sodium chloride (Sigma Aldrich; Certified ACS Grade), and magnesium chloride hexahydrate reagent ACS (ACROS ORGANICS).

### **c. Sample Preparation**

Preparation of substrates for AFM and spectroscopy is critically important to the outcome of the experiment. As a minimum requirement, to remain within the physical limits of the equipment, the substrate's vertical topography can vary no more than a few microns. If this condition is met, then AFM typically can be performed on the sample to show a topography map of the surface. In atomic force spectroscopy with a colloidal probe, contact area, substrate deformation, contamination, and the polar nature of the surface all affect the interactions between probe and sample. Contact area between the probe and surface will affect the magnitude of the force interaction. Consequently, a homogeneous but rough substrate can falsely indicate that the force varies over the surface more than it actually does. In this case, a substrate with a surface topography of only a nanometer or less is an ideal choice for studying the interactions between a probe and a single material.

Sample deformation can affect the adhesion by changing the contact area between the probe and sample. This aspect is an important consideration for substrate selection, although it may be impossible to change if one particular substrate is required. Contamination of the substrate via air-borne molecules or contact with other substrates should be minimized as much as possible, e.g. storing the substrates upright in covered Petri dishes when not in use and touching as little of the sample as possible when moving it with clean tweezers. This is particularly important because, when force measurements are performed with a colloidal probe, the measurements are performed with limited knowledge of the exact location on which they are being collected. If the

sample is first scanned with a sharp tipped probe, to identify any surface features/contaminants and then the measurements are taken, the user knows the exact location. However, measuring the forces becomes difficult because the interactions are between a much smaller probe and surface. Additionally, if the probe becomes blunted throughout the experiment, then the force measurements will change as a function of the changing probe contact area. Furthermore, polar substrates can develop a water film on their surfaces when exposed to naturally occurring humidity in the air. This water layer can then lead to capillary forces between probe and sample which further complicate any adhesion measurements being conducted. These aspects demonstrate the importance of preparation method for substrates used in AFM. In the following sections we detail the process of preparing a wide variety of substrates from our experimental work.

### **c.1. Homogeneous Substrates**

For some applications, we require a substrate which exhibits a similar surface chemistry over a macroscopic area (millimeters) but has very little surface topography (nanometers). To facilitate use by other researchers, we have grouped these surfaces into polar and nonpolar categories. In each case, we provide a sample AFM topography scan of the substrate and a roughness measurement. The RMS roughness is calculated as the standard deviation of all the height measurements for an entire scan. In cases where there are GO flakes on the surface, i.e. mica, the GO flakes are excluded from the roughness measurement.

### c.1.1. Polar

Mica, a sheet silicate, provided an atomically smooth, polar surface on which to apply various particles and test force interactions. In all cases, we cleaved the mica (Ted Pella; PELCO®, Grade V5) with Scotch® transparent tape to expose a new, uncontaminated surface. Figure 6 shows a mica substrate with a group of GO flakes deposited along the left side of the image. The RMS roughness of the mica is 0.078 nm. Some applications, such as the AFM liquid cell, also require the edges of a mica piece to be clean. For these applications, it is best to retain a dedicated pair of scissors which have been previously cleaned via sonication in surfactant solution, dried with compressed nitrogen and stored in a designated Petri dish. We then cut the edges of the piece of mica so that when the final cut is made, the mica falls onto a waiting piece of Scotch tape for cleaving.

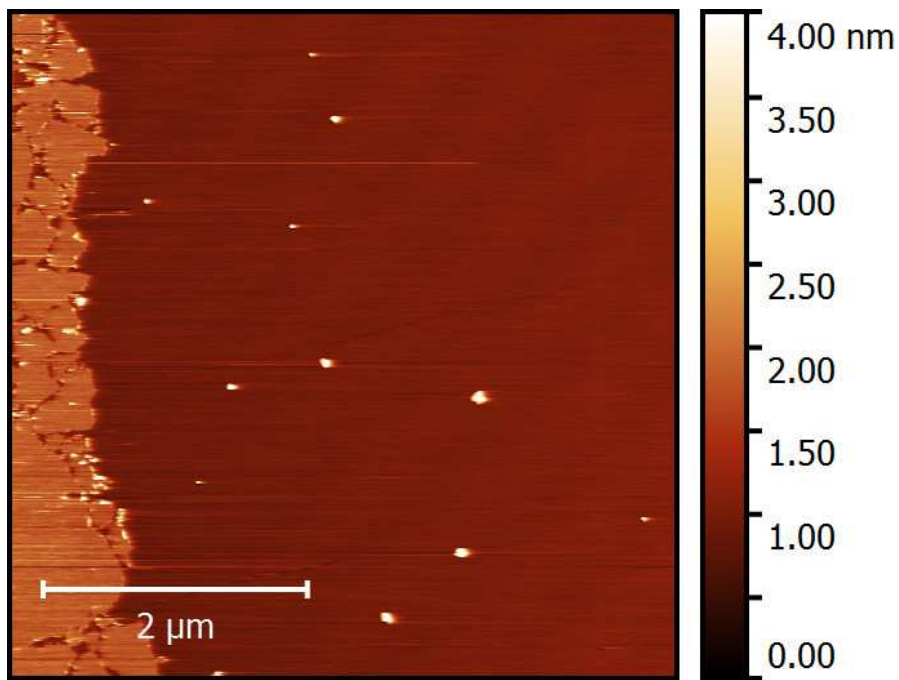


**Figure 6 AFM topography scan of mica to provide an example of surface roughness. GO flakes are dispersed along the left side of the scan.**

Although mica is useful as a model polar substrate, sometimes the ease with which it cleaves is not ideal. As an alternative to mica we used a silicon wafer (Ted Pella 200 nm thermal oxide on ø6”, ultra-flat wafer) broken into small pieces. In comparison to mica, silicon is not as flat. Figure 7 shows an AFM scan of a silicon surface with deposited GO flakes. The RMS roughness is 0.263 nm. In addition to its rougher surface, silicon must be subjected to cleaning before use, with surfactants or Piranha, depending on the experimental necessities. However, its inability to cleave like mica is essential in some cases. For example, when making a flat polymer film it may be necessary to peel the film off of a flat template. If the adhesion between the polymer and mica is large enough to cleave the mica, then silicon will be the necessary choice.

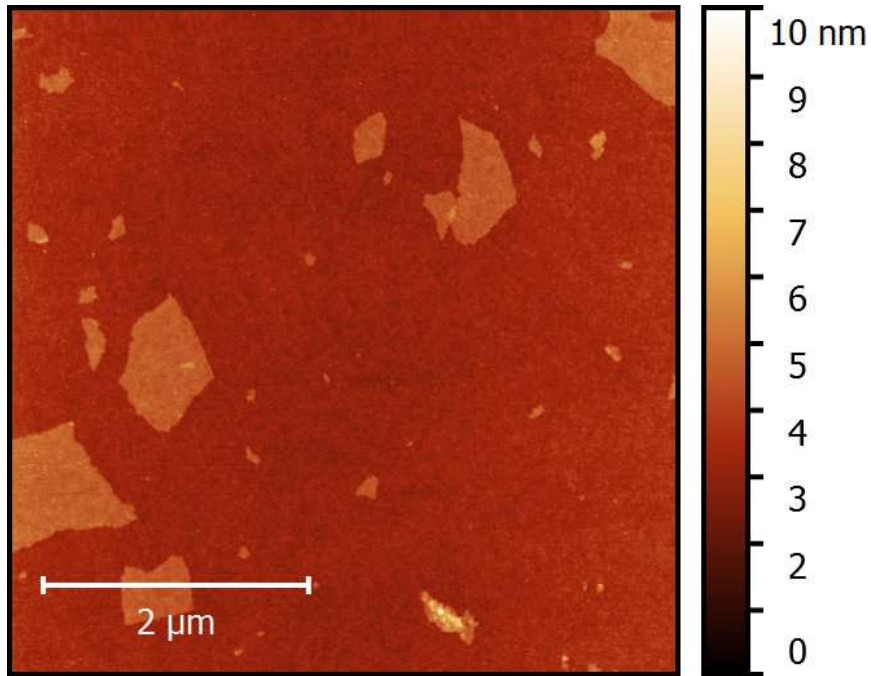


**Figure 7** AFM topography scan of silicon, with GO dispersed on the surface, to provide an example of surface roughness.

To make a film from poly(methyl methacrylate), or PMMA, we combined PMMA (molecular weight 120,000 from Sigma Aldrich) with DMF at 20% PMMA to 80% solvent. We applied this mixture to a cleaved piece of mica (or HOPG) and dried it at 90 °C.<sup>99</sup> To expose the flat side of the PMMA, we used a scalpel to separate the film from the mica, peeled it off and inverted the film. Figure 8 shows an AFM topography scan of the PMMA side that was closest to the mica template. The polymer surface exhibits small holes, indicated by black dots, with some variation in background color. The RMS roughness is 0.435 nm.

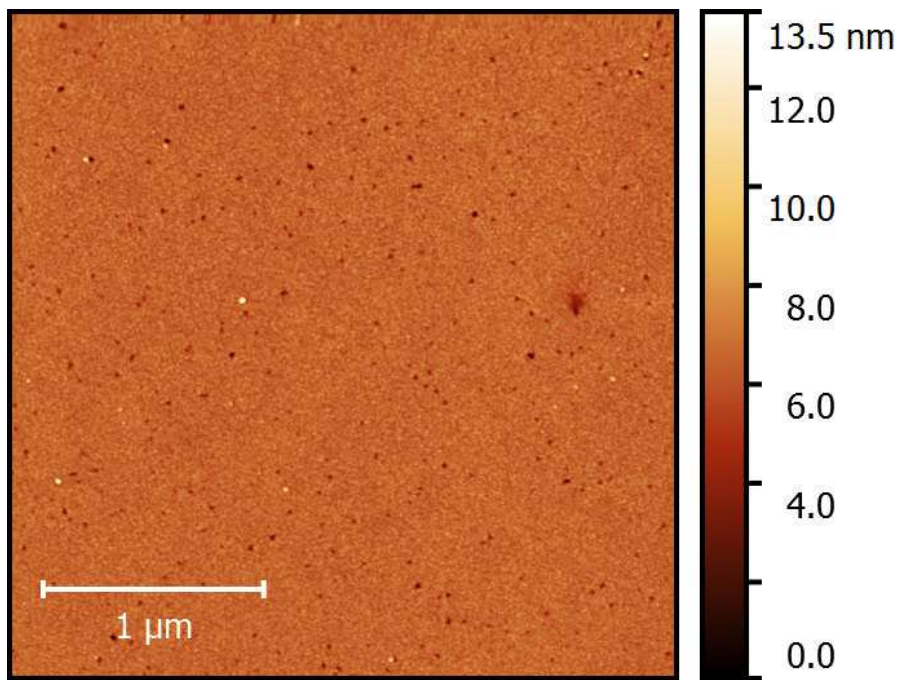


**Figure 8 AFM topography scan of PMMA to provide an example of surface roughness.**

Our lab has made a flat film from poly(vinyl alcohol), or PVA, by combining Mowiol 4-88 (molecular weight of 31,000 from Sigma Aldrich) with deionized water at 20% PVA to 80% water.<sup>99</sup> We then applied this mixture to a cleaved piece of mica and dried it on a hot plate at 50 °C. We peeled the sample in the same manner as PMMA. However, since PVA and mica are both polar this sample is sometimes more difficult to peel from the mica compared to a nonpolar polymer. Figure 9 shows an example of the PVA peeled from a mica template. The side of the PVA closest to the mica has a RMS roughness of 0.449 nm.

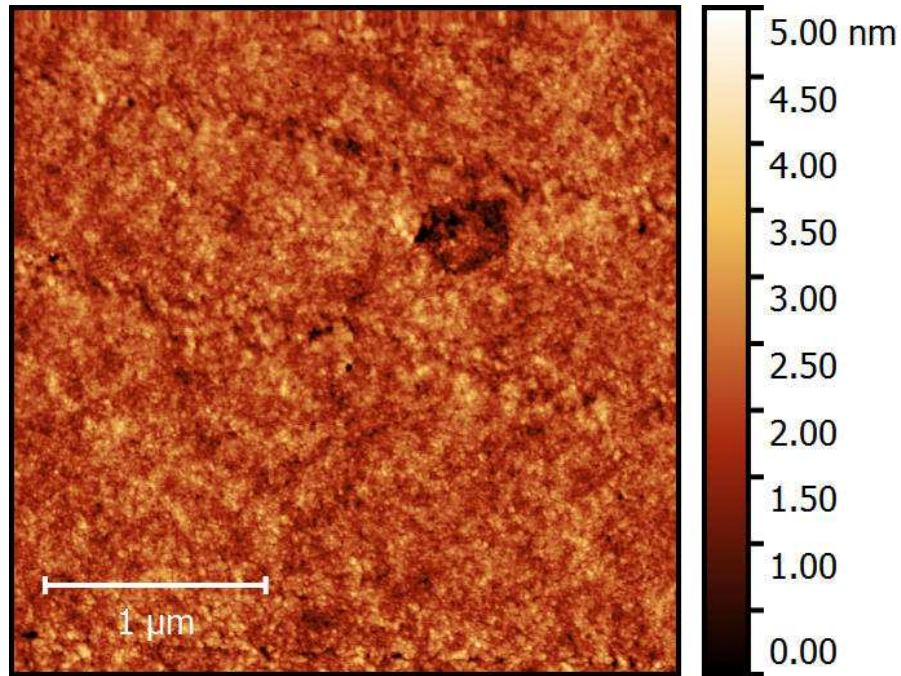


**Figure 9 AFM topography scan of PVA to show surface roughness.**

We made a polyetherimide, or PEI, film by combining PEI (Ultem 1000) with DMAc at 20% PEI to 80% solvent, applied it to cleaved mica (or cleaved HOPG) and dried it at 90 °C.<sup>99</sup> Then we peeled and inverted the sample using the same method as PMMA. The AFM scan in Figure 10 of PEI peeled from mica shows multiple small holes on a uniformly colored background surface. This scan exhibited a RMS roughness of 0.77 nm.

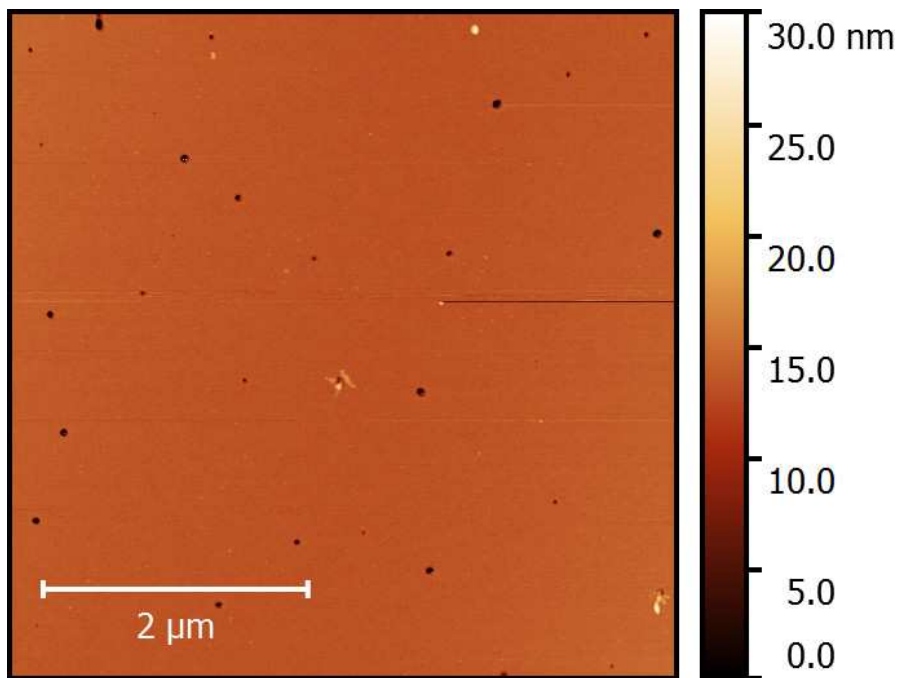


**Figure 10 AFM topography scan of PEI to show surface roughness.**

We collaborated with the lab of Dr. David Kranbuehl (Chemistry department, The College of William & Mary) to obtain flat polyimide (PI) films.<sup>100,101</sup> They prepared the poly(amic acid) using benzophenone-3,3'-4,4'-tetracarboxylic dianhydride (BTDA), 4-4' oxydianiline (4-4' ODA) and dimethylacetamide (DMAc). We pipetted less than 1 mL of this resulting yellowish orange liquid onto a cleaved sheet of mica, nearly covering the entire surface. To cure the PI film, we placed the mica in a glass Petri dish into a cold Thermolyne 47900 furnace. We set the furnace temperature to increase to 100 °C, remain at temperature for one hour, increase to 300 °C for over two hours, remain at temperature for one hour, and decrease to room temperature. To remove the polymer from the mica, we used a scalpel. However, this polymer makes a very thin layer which rolls upon itself when removed from the mica. To study the flat surface closest to the mica we determined that the best method was to cut around the

edges of the size piece we needed. We then attached a piece of adhesive tab to a metal disc (both from Ted Pella), pressed this firmly against the PI piece and then used the scalpel to release it from the mica. In this way, the PI is already attached to the disc and cannot curl. We then performed AFM scans on the PI to determine surface topography. The scan in Figure 11 shows a mostly uniform background coloration with a few holes. This resulted in a RMS roughness of 0.432 nm.

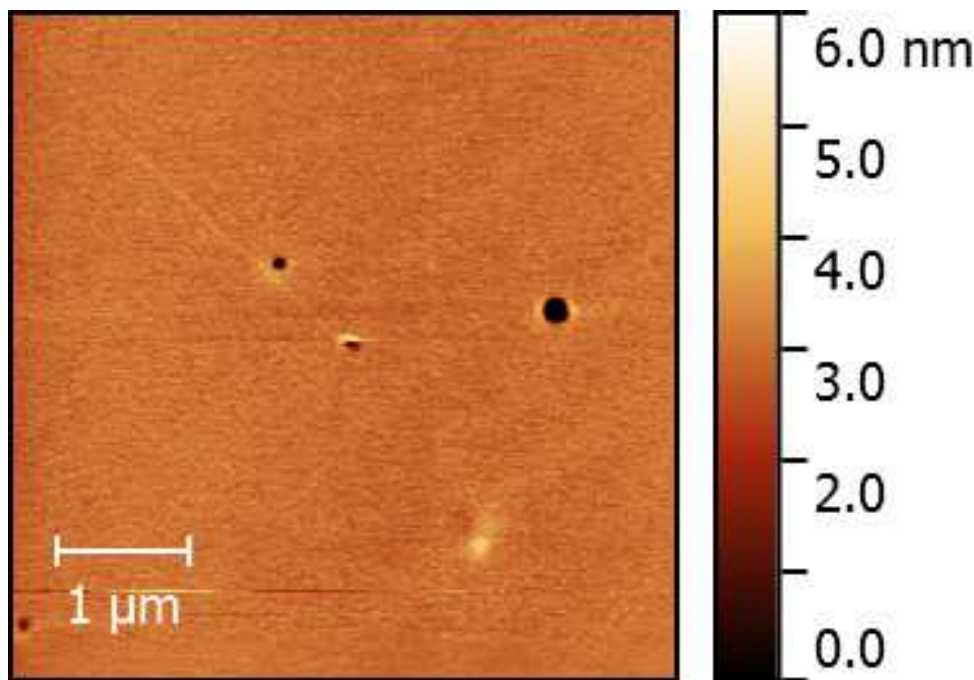


**Figure 11** AFM topography scan of PI to show surface roughness.

One of the roughest polymer samples that we utilized was made from an acrylic emulsion (Rhoplex™ HG-706) mixed with water and drop cast onto a mica substrate. We cured the polymer samples at ambient temperature and pressure for a range of times from a few hours to a few weeks. In all cases, after peeling the acrylic from the mica substrate and scanning the side closest to the mica, we observed a bumpy surface. The exact roughness of this sample is difficult to quantify because it encompasses both

small scale, few nanometer tall sphere-like protrusions, and large scale topography variations (Figure 12). However, by using the same method for determining roughness as the other substrates, we found a value of 1.756 nm.

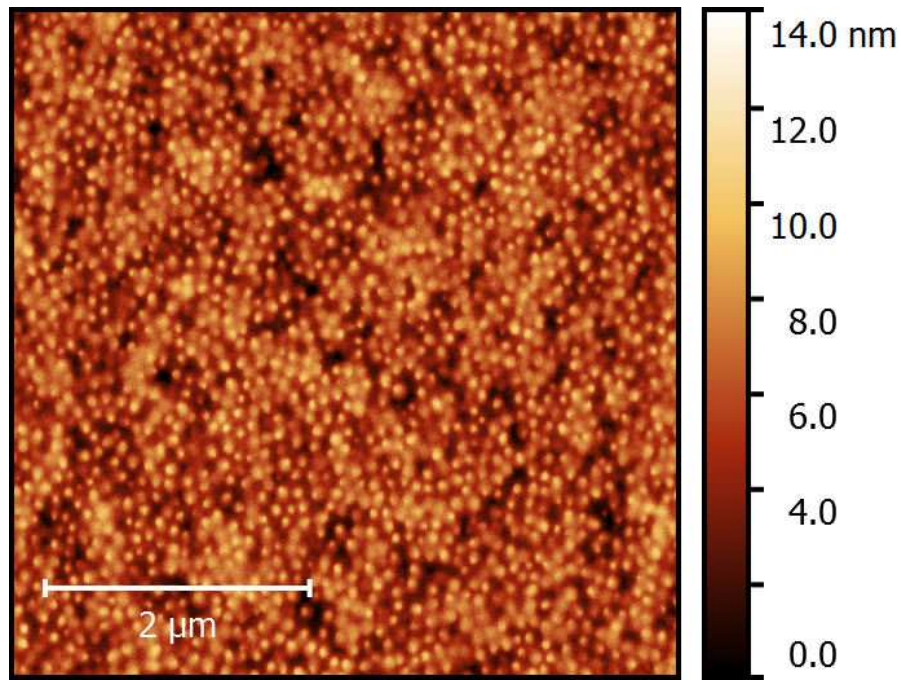


**Figure 12 AFM topography scan of an acrylic substrate to show surface roughness.**

### c.1.2. Nonpolar

Highly oriented pyrolytic graphite (HOPG) provides a nonpolar surface which is easily cleaved with Scotch tape. Just like mica, it requires no additional cleaning of the substrate, only cleaving. However, compared to mica it exhibits layers that are smaller laterally. This difference results in a surface with many flat stepped features. The AFM scan image in Figure 13 shows many layers of HOPG with GO deposited on top. The cross section ("1") along a single atomic step shows an RMS roughness value of 0.158 nm. In contrast, the entire image shows a roughness of 0.967 nm.

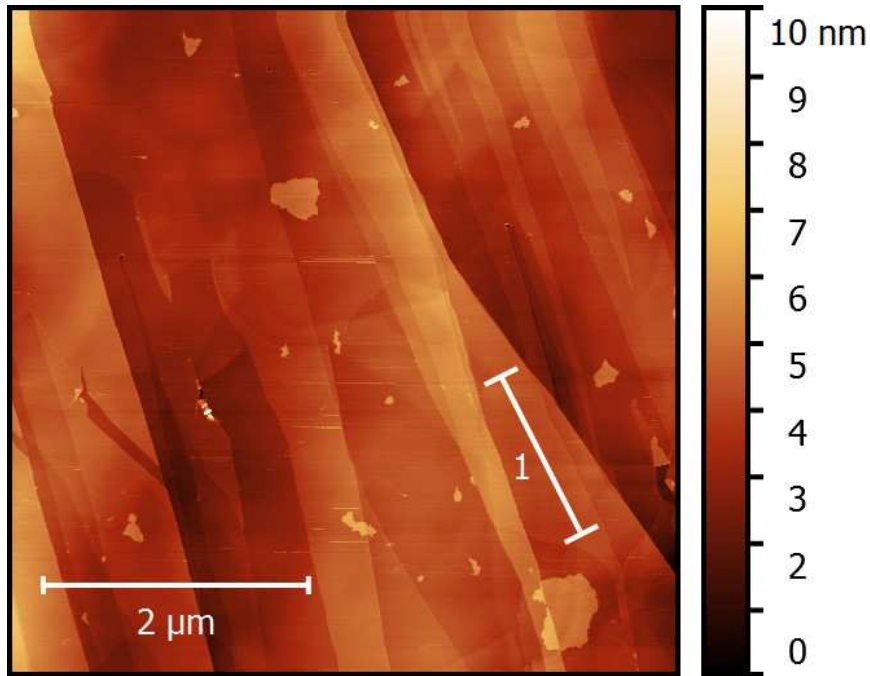


**Figure 13 AFM topography scan of HOPG, with GO flakes dispersed on the surface. A roughness measurement was collected on the entire image and a localized step (indicated by the “1” cross section bar) to show the different scales of roughness.**

Silanizing mica creates a hydrophobic, flat surface. This can be a very useful replacement for HOPG because the much larger lateral layers of mica are less likely to peel off if something, like a layer of polymer, needs to be removed from the surface.

Figure 14 shows an AFM topography scan of silanized mica with GO flakes on top for comparison. The roughness of the silanized mica is similar to silicon as the RMS roughness is 0.210 nm. To silanize the mica we use (Tridecafluoro-1,2,2-Tetrahydrooctyl) Trichlorosilane (Gelest, Inc.). Great care should be taken with the silanizing agent as it is very corrosive and degrades when it contacts water in the air. It should always be stored in a vacuum desiccator when not in use. To silanize the mica we started by placing a Petri dish with the sample and a microscope coverslip in a desiccator. We then added 3  $\mu$ l of silanizing agent to coverslip, sealed the desiccator

and waited for 2 hours. Afterwards we removed the newly silanized substrate and stored it in a sealed Petri dish until needed.

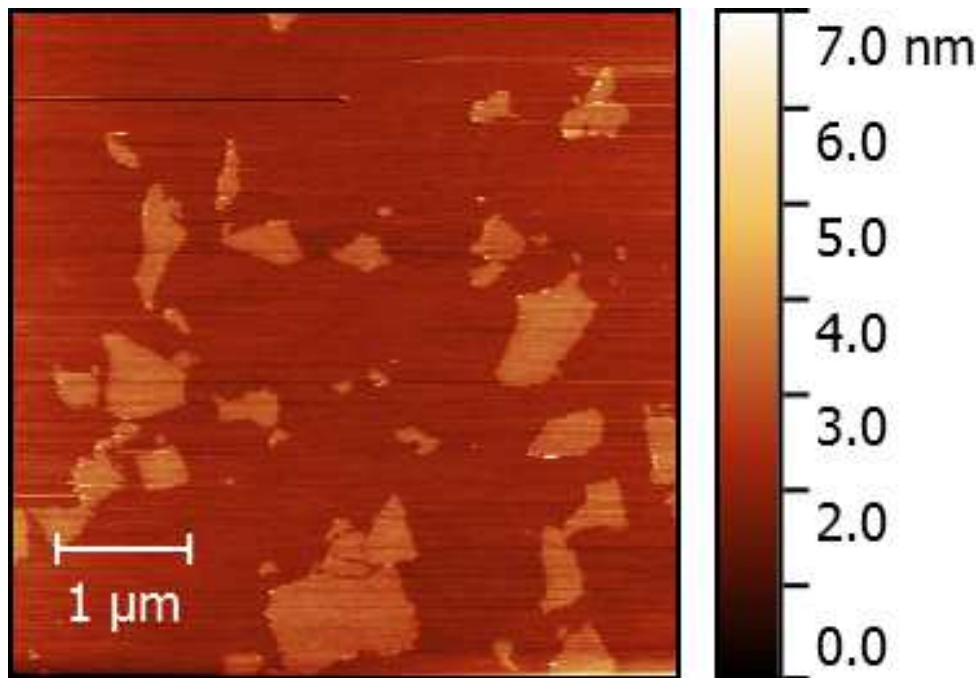


**Figure 14** AFM topography scan of silanized mica, with GO dispersed on the surface, to show the surface roughness.

Our lab has made polystyrene (PS) films using both solvent cast and melting techniques. For the solvent technique, we combined PS (molecular weight 230,000 from Sigma Aldrich) with toluene at 20% PS to 80% solvent, applied the mixture to cleaved mica (or HOPG) and dried it at 50 °C.<sup>99</sup> We have also placed cleaved mica directly on a hot plate at 200 °C, added PS (Polystyrene, Melt Index 7.5, Sigma Aldrich) pellets and heated for approximately 5 minutes. We then added another piece of cleaved mica and pressed gently to distribute the melted PS into a film. Within minutes of removing it from the hot plate there was an audible cracking sound as it

separated from the mica. An AFM scan of our heat pressed PS is included in Figure 15. It shows a RMS roughness of 0.181 nm.

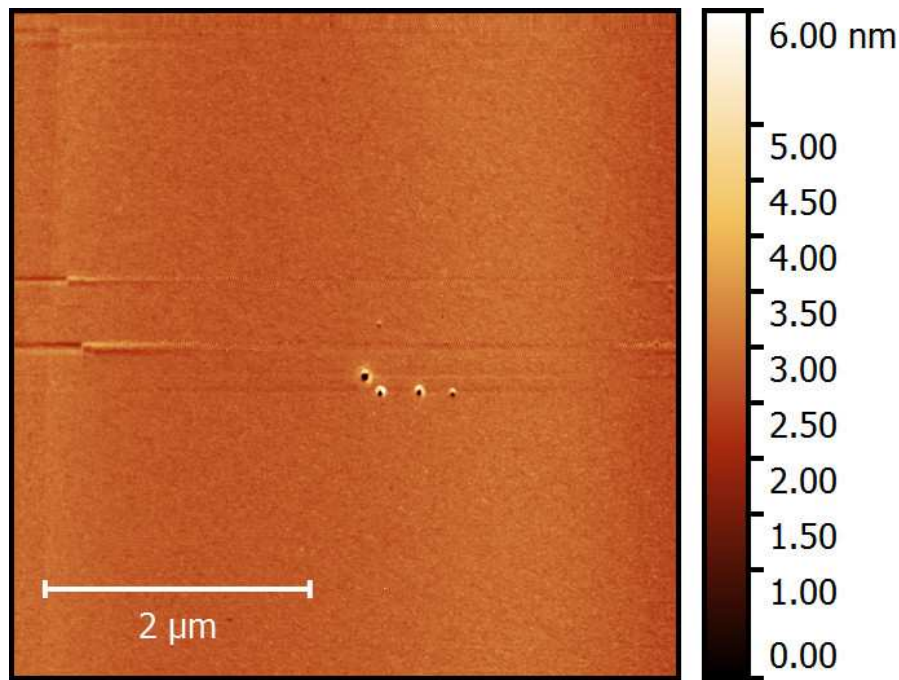


**Figure 15 AFM topography scan of PS, melted on a hot plate and templated on mica, to show surface roughness.**

We have worked with two different polyethylene (PE) substrates, a high density polyethylene (HDPE) and a low density polyethylene (LDPE), but these polymers were not as flat as the other polymer substrates. To make the samples, the HDPE (Sigma Aldrich) and LDPE (melt index 25g/10min., Sigma Aldrich) were each individually sandwiched between cleaved sheets of mica. Then the mica/PE/mica substrate was placed between two Teflon® plates and wrapped in Teflon® film, which was sealed with Kapton® tape. The film pouch was flushed with argon gas during the experiment. After heating a heat press (Carver laboratory press) to 145 °C, the experiment deviated for the two substrates. For the HDPE, the sample was heated in the press without

pressure for 30 minutes. Then the sample was pressed, the heater was unplugged and the sample was allowed to reach room temperature under pressure. Four hours later, it was removed from the press. In contrast, the LDPE was left in the heat press for 20 minutes without pressure. Then the sample was pressed, the mica/PE/mica sandwich was quickly removed from the heat press and it was dropped into a container of liquid nitrogen to quench. As Figure 16 exhibits, the surface topographies are very different for these two polymers which were prepared in two different ways. They are much rougher than any of our other substrates with RMS roughness values of 6.40 nm for HDPE (Figure 16A) and 5.65 nm for LDPE (Figure 16B). Although they are much rougher than the other polymers that we have worked with, if we compare cross sections of the two with a cross section of the surface of a colloidal probe, we see that the localized flatness of the plate-like features of the LDPE provide many flat areas of contact (Figure 16C). Based on the application, this method for preparing this nonpolar polymer could still be very useful.

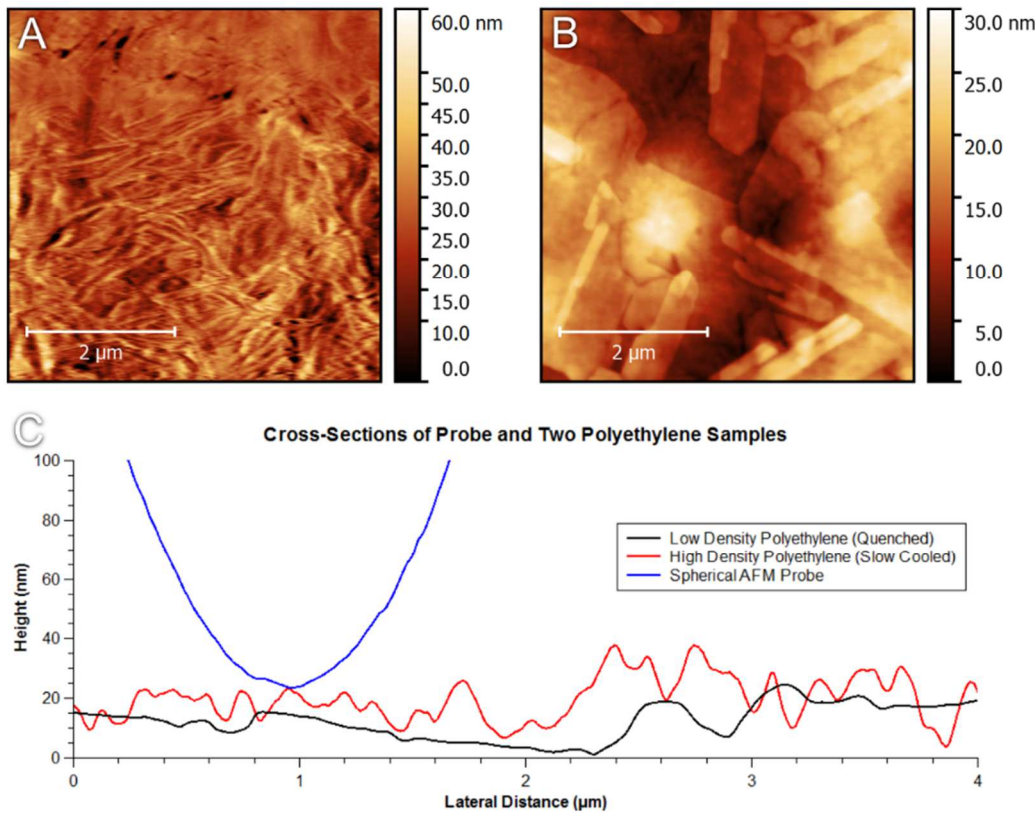


**Figure 16 AFM topography scans of HDPE that was heat pressed and cooled slowly (A) and LDPE that was heat pressed and quenched in liquid nitrogen (B). The cross sections show the relative height comparison of the surface roughness of the two substrates to the surface roughness of a 7.2  $\mu\text{m}$  diameter colloidal probe (C).**

### c.2. Heterogeneous Substrates

Particle size and shape strongly affected which preparation method we chose to characterize different materials in our research. The planar structure of some, such as GO and alumina, necessitated dispersing the particles onto a larger flat substrate. However, other materials, like sandstone grains, exhibited such a complex shape that we needed to rely on other methods to stabilize them for analysis. The following sections detail the processes for working with each type of particle to make heterogeneous substrates. Force spectroscopy data is not included for all of these

substrates in the results chapters. However, the development process for each substrate was vital to our final experimental choices. Therefore, as a reference for other researchers, we have included a detailed account of how to make a variety of flat substrates for AFM characterization.

In order to assess the exfoliation and size of GO particles, our collaborators in the lab of Dr. David Kranbuehl (Chemistry department, The College of William & Mary) provided GO flakes that were dispersed in water at varying concentrations. The GO was produced in two different ways (Hummers' method and Improved method) and then dispersed in Millipore water to make a Hummers' method GO<sup>102</sup> (GO<sub>h</sub>) dispersion of 0.26 mg/mL and an Improved method GO<sup>103</sup> (GO<sub>i</sub>) dispersion of 0.46 mg/mL. We used sonication to disperse the GO<sub>h</sub> and to break the GO<sub>i</sub> into flakes of similar size to the GO<sub>h</sub>. Spin coating conditions were 1  $\mu$ L, 3000 rpm and 3 minutes for both dispersions and all substrates, e.g. mica, silanized mica, silicon, and HOPG. By performing AFM scans (Figure 17), we can then determine particle size and thickness. This method is very effective due to the flat, plate-like nature of the flakes.

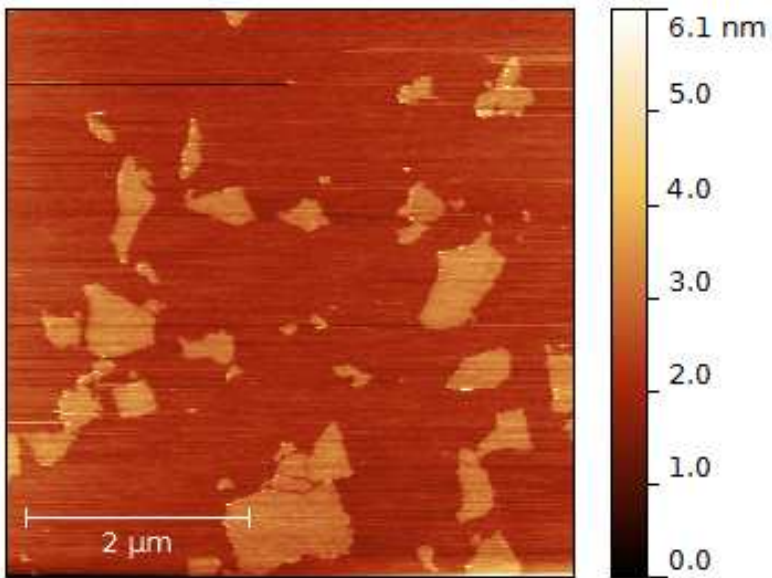


**Figure 17 AFM topography scan of GO dispersed on silanized mica to show the relative size, shape, height, and spatial distribution of the GO flakes after spin coating.**

We combined alumina platelets (Ronaflair® white sapphire alumina flakes from Merck) with Millipore water and spin coated them onto a glass cover slide at 3000 rpm for 3 minutes. Before use, the glass cover slide was cleaned in surfactant solution and dried with compressed nitrogen. Unlike the GO flakes, this spin coating process results in many platelets piled on top of each other. To remove the excess and loosely bound platelets, we tilt the mica vertically and rinse it with a gentle stream of 1 mL of Millipore water. Spin coating a second time removes the excess water. Most of the platelets are large enough to clearly see in our optical microscope (Figure 18A). Any remaining aggregates exhibit visible rainbow interference patterns. In contrast, only the outline is visible on individual flakes that are flat against the substrate (red box in Figure 18A). Their large lateral size makes it possible to locate the exact same platelet

in both optical images and AFM scans. Scans of these platelets show that they have a stepped surface (Figure 18B) similar to the HOPG substrate. As the AFM image shows, on the same platelet the range in height can easily vary by over 100 nm.

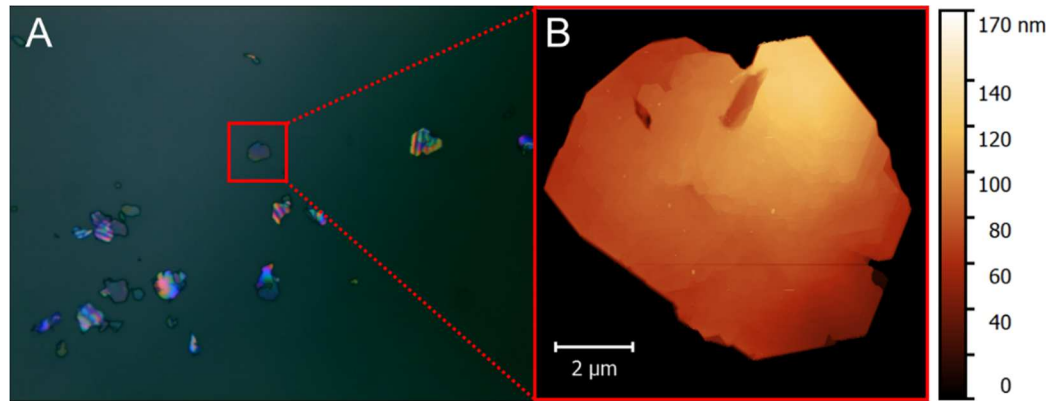


**Figure 18 Alumina platelets, dispersed on mica that have been identified optically (A) and with AFM (B). The red boxes indicate the same platelet in both (A) and (B).**

Although sandstone grains provide the opportunity to study native mineral surfaces, in some cases we wanted to examine the surface forces while minimizing the effects of topography. For those cases, we analyzed a pre-made thin section of sandstone (Shell Global Solutions International). A thin section is a type of sample commonly used by geologists for rock identification. The sandstone, or other rock, may be injected with resin for stability, attached to a glass slide and cut to a set thickness. Dr. Brent Owens (Geology department, The College of William & Mary) helped us use their petrographic microscope in order to identify individual mineral species so that we could later perform AFM experiments on particular minerals. Our experience has been that these thin sections provide a surface that is flat enough to easily scan with an AFM. In Figure 19 we show an optical image of a feldspar grain in a thin section (Figure 19A) and the corresponding AFM scan of part of the same grain (Figure 19B).

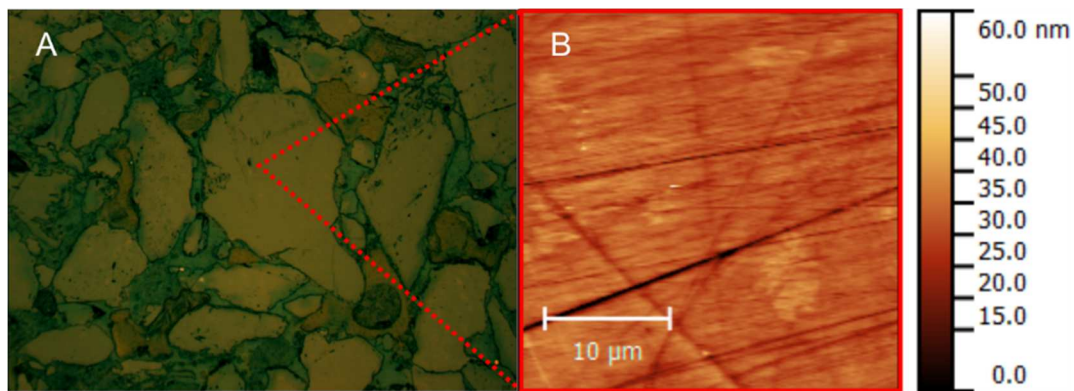


**Figure 19 Optical image (A) and AFM topography scan (B) of a mineral grain in a thin section. The scan in (B) was conducted on the grain indicated by the dotted lines in (A).**

It is also possible to investigate sandstone grains without the aid of a thin section. The method described by Hassenkam et al.<sup>22</sup> involves dropping individual sandstone grains onto a thin layer of epoxy on a flat substrate. Then optical microscopy is used to identify grains which landed with flat sides of the mineral facing upward. Figure 20 provides an example of three mineral grains that we prepared in this manner. We received these “A” reservoir grains from Shell Global Solutions International to perform force spectroscopy tests with “A” oil from the same petroleum reservoir. We attached the grains to a mica substrate so we could cut around the grains which we intended to test. By also cleaving the back of the mica sample, this reduced the possible contamination that could be introduced to the liquid cell by the substrate.

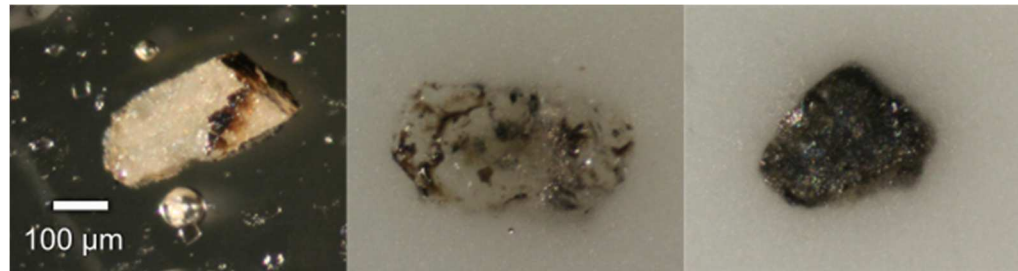


**Figure 20 Optical microscopy images of three different sandstone grains stabilized in epoxy on which we later performed force spectroscopy experiments.**

We have also worked with multiple millimeter in diameter pieces of clay minerals. In order to perform AFM analysis on these samples we first used epoxy to attach a piece of clay to a flat substrate, such as a metal disc, so that the cleavage plane was parallel to the substrate. Then we used a scalpel to cleave the mineral and used an optical microscope to identify locally flat areas of the sample. Figure 21 shows an optical image of a locally flat area that formed during cleaving (Figure 21A). Scanning on that area of the sample showed the stepped surface features of the clay (Figure 21B).

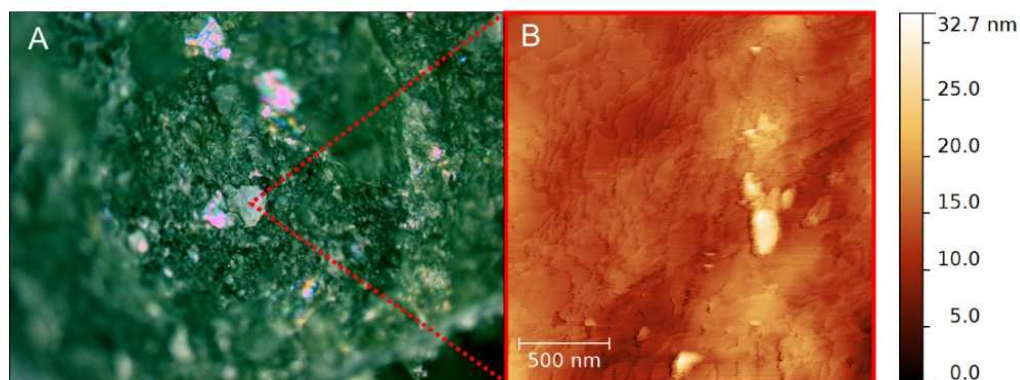


**Figure 21 Optical image (A) of a cleaved piece of illite mineral and AFM topography scan (B) of a localized area of the illite showing the stepped features of its topography.**

## **d. Bare Silica Colloidal Probe**

In order to make various functionalized tips suited to studying particular interactions we had to start with a basic model. Colloidal AFM probes are commonly utilized in force spectroscopy measurements to provide a spherical geometry, increased force interactions, and a stable surface. The spherical geometry is easier to model the relevant interactions and the increased force interactions are due to the large probe size in comparison to a sharp probe. Additionally, the colloidal probe will not become broken or blunted like a sharp probe, leading to a stable surface. We started by constructing these probes in our lab and testing them in various combinations of brines and substrates prior to functionalizing them with oil or GO.

### **d.1. Tip Holder**

We utilized an Olympus inverted microscope (model #: IX71) and an XYZ translation stage (Newport Corporation XYZ translation stage, model #: 460-XYZ and Siskiyou Corporation hydraulic micromanipulator, model #: MX6600R) to manufacture all the AFM probes. However, this necessitated the design of unique tip holders in order to move the probe within the two to four millimeter working distances of the microscope objectives. For most of the probes we sandwiched a chip between two glass microscope slides with a binder clip (Figure 22). While using this simple device, we were able to make AFM tips, submerge them in solvent for cleaning, and heat them in the oven, all while avoiding manipulating the few millimeters wide chip with tweezers, an action which can easily result in destroyed chips.

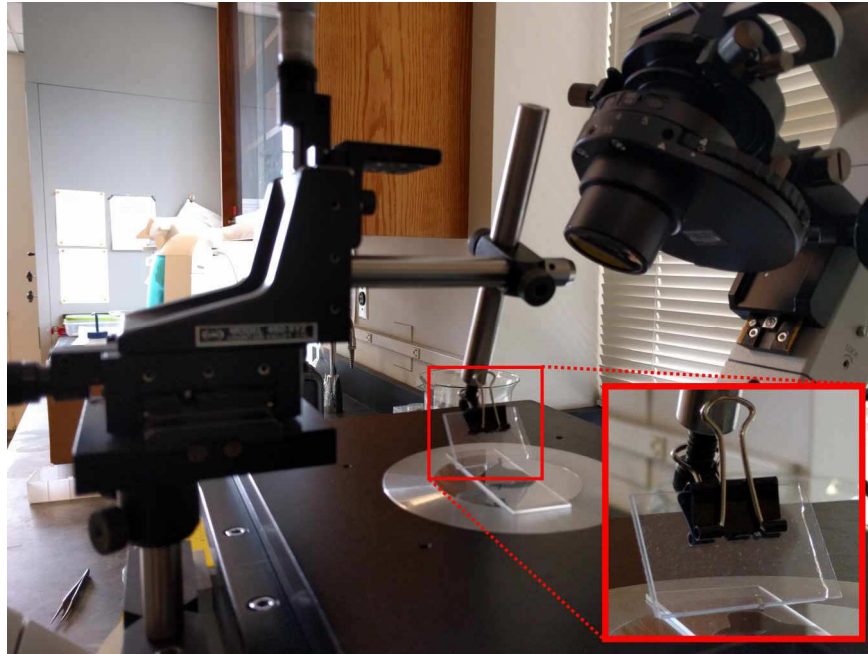


**Figure 22 Custom AFM probe holder attached to a translation stage on the Olympus inverted microscope. Inset box shows a magnified view of the probe holder.**

## d.2. Construction

Over the course of the experiments, we used a variety of components to construct the colloidal AFM probes including sphere materials, cantilevers, and epoxies (detailed in Materials). In all cases, we made the probes by attaching the chip to a translation stage on the Olympus inverted microscope, lowering the cantilever into a droplet of epoxy, supported on a glass slide, and then lowering the cantilever onto a glass slide covered in silica spheres. After the epoxy cured, we analyzed them optically using the Olympus microscope to determine that the sphere was attached and in some cases took scanning electron microscope (SEM) images (Figure 23A). In these cases we used Amray 1810 and Hitachi S-570 SEMs after sputter coating the probe with a gold/palladium coating (Anatech Hummer 6.2 sputter coater). In some cases, it was particularly important to

view the surface of the sphere. For this we scanned an NT-MDT TGT1 calibration grating with the probe. The AFM topography scan rendered in 3D (Figure 23B) shows both the curvature of the probe and the surface topography. To obtain a more quantitative roughness measurement we subtracted the spherical curvature from the AFM image using two second order polynomial fits along the  $x$ -axis and  $y$ -axis. Then we applied the same roughness measurement to the flattened surface (Figure 23C) that we used for all the substrates and found an RMS roughness of 1.88 nm. In comparison, seven of our substrates, mica, silicon, PMMA, PVA, PI, silanized mica, PS, have a roughness less than one third of the roughness of our probe. Three substrates, PEI, HOPG, acrylic, are somewhat smoother than the probe, and two substrates, LDPE, HDPE, are rougher than the surface of the probe. Therefore, in force spectroscopy experiments performed with these probes and substrates, we would expect the least topography induced adhesion artifacts from the seven smoothest substrates and the most artifacts from the two roughest substrates.

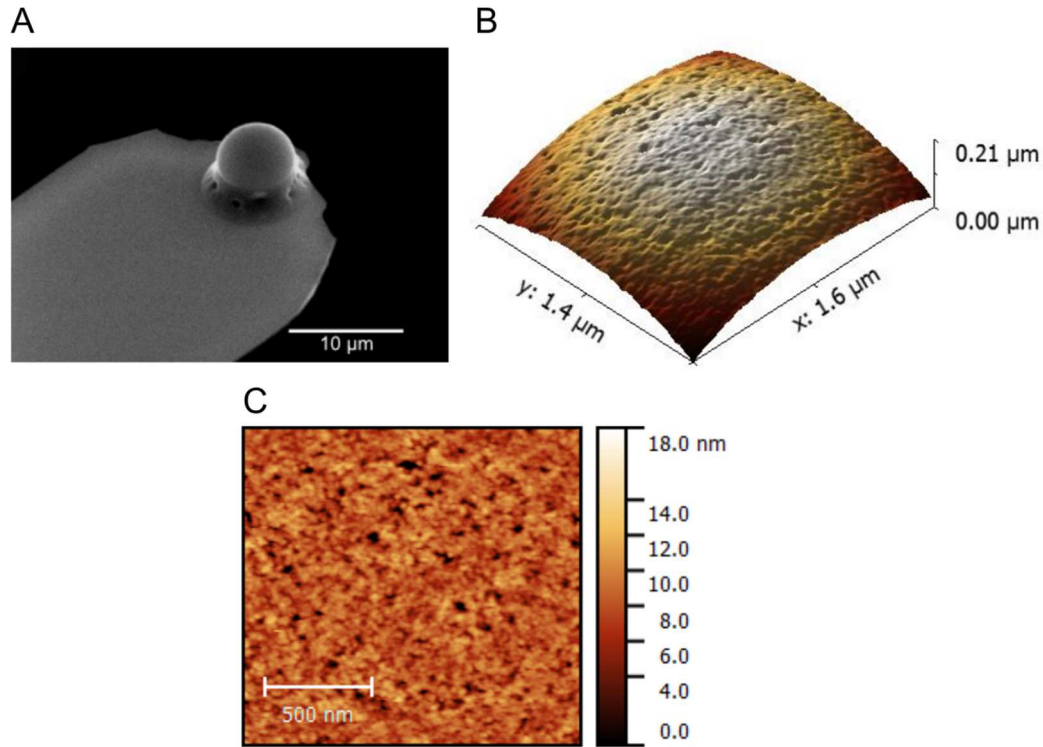


**Figure 23** Scanning electron microscope image of a bare silica sphere probe constructed in our lab (A) and a 3D representation of a calibration grating scan of the surface of a silica sphere probe (B). We subtracted the spherical curvature from the AFM topography image to make a new flattened image (C) to which we applied a roughness analysis.

### d.3. Force Spectroscopy: Model Substrate

For our initial control experiments, we performed force spectroscopy measurements on cleaved mica substrates. Observing the effect of various salt solutions on the mica/bare probe force interactions is a crucial first step to understanding the behaviors of more complicated systems.

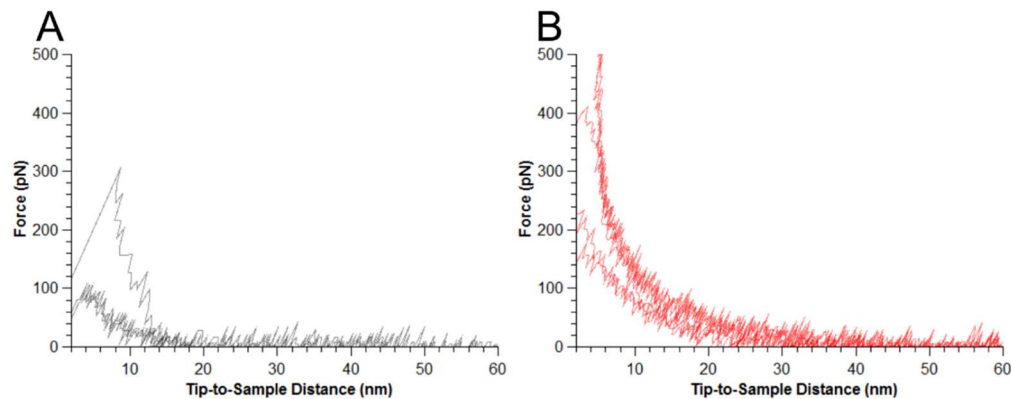


**Figure 24 Processed approach curves from a commercial silicon nitride tip on a mica substrate in 10 mM NaCl (A) and 1 mM NaCl (B).**

By simple brines we refer to liquid cell solutions made with a single salt type, such as sodium chloride. We performed an initial experiment on mica with a sharp tipped silicon nitride probe. A few of the processed approach curves are included in Figure 24. They show repulsion, indicating that both the tip and mica have the same charge. Additionally, the exponential nature of the force as a function of tip/sample separation distance decays more rapidly with the 10 mM NaCl solution (Figure 24A). This is expected by electric double layer theory and serves as a control for our experiment, showing that we are able to take liquid cell measurements that vary as a function of salt concentration.

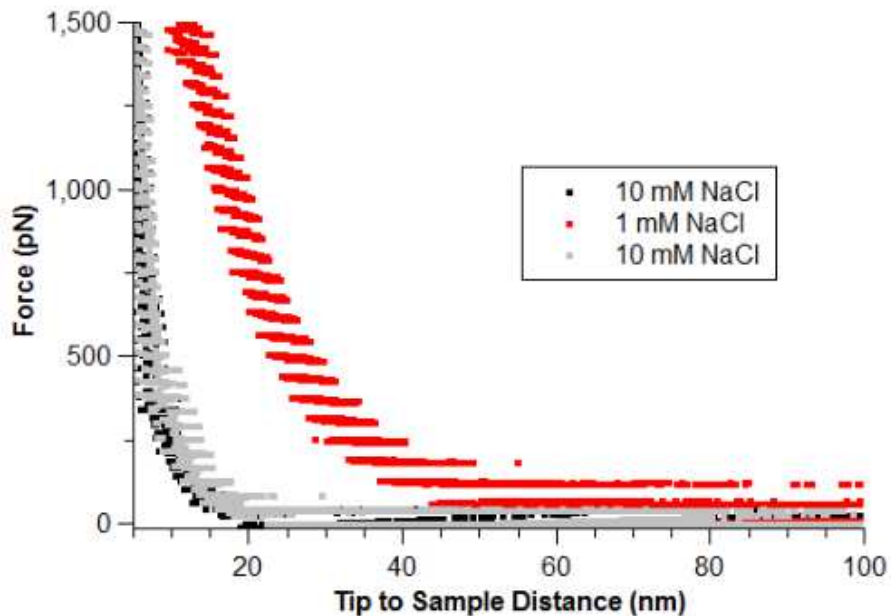


**Figure 25** Force curves taken with a custom bare silica sphere probe on a mica substrate in the following brine solution order: 10 mM/1 mM/10 mM NaCl, indicated by black, red, and grey scatter points, respectively.

We then performed measurements with a bare silica sphere probe on mica. By taking the measurements in 10 mM/1 mM/10 mM NaCl solutions we are able to show the reproducibility of our measurements. In Figure 25, both data sets from the 10 mM NaCl experiments overlap, as represented by the black and grey scatter points. This shows that our bare silica probe is both reproducible and that our rinsing procedure has fully removed traces from the 1 mM NaCl that was used in the liquid cell between the 10 mM NaCl measurements. Both the 1 mM NaCl and 10 mM NaCl curves show electrostatic repulsion which varies as a function of salinity.

For complex brines we used recipes based on the salt composition of a particular oil reservoir “A”. We refer to these as formation liquid (4 M) for the ion composition found naturally in the reservoir and low salinity brine (28 mM) to simulate the

reduction in ion concentration caused by the injection of low salinity water into the reservoir during secondary recovery. These experiments were performed with a colloidal silica probe. Details of the resulting approach and retract curves are provided in the following sections. The six experiments (M-1, M-2, M-3, M-4, M-5, M-6) are denoted by the mica (M) substrates and chronological order of the experiments.

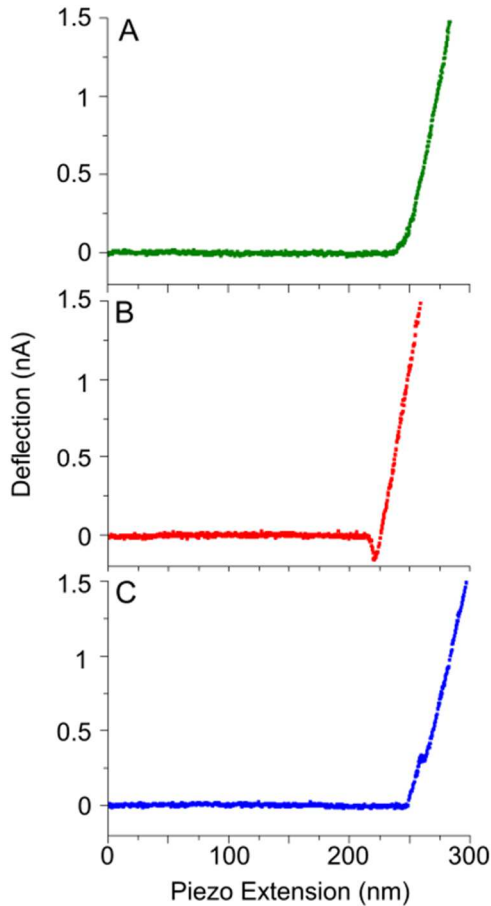


**Figure 26 Examples of features used to categorize approach curves in the complex brine experiments: repulsion (A), attraction (B) and other (C). In “C”, the curve transitioned directly from the no-deflection region to the constant compliance region without noticeable repulsion or attraction, i.e. snap-down.**

Based on the calculated Debye lengths for the salt concentrations in these two brines, measuring electrostatic repulsion is expected to be very challenging. Even for the low

salinity brine, the Debye length is very small, 1.8 nm. Although some of our curves exhibited an upwards deflection of the cantilever upon approach, the exponential fits that we tried to apply to the data did not fit the trends that we observed. Therefore, we conclude that our experimental results did not contain expected indications of electrostatic repulsion in the approach curves. Despite this, there were noticeable variations between the curves which we have quantified in the plot below by grouping the curves into three categories: Repulsion, Attraction, and Other. These are distinguished by upward deflection of the cantilever upon approach to the surface, downward deflection of the cantilever, and no distinct gradual deflection of the cantilever which might indicate the effect of forces, respectively.

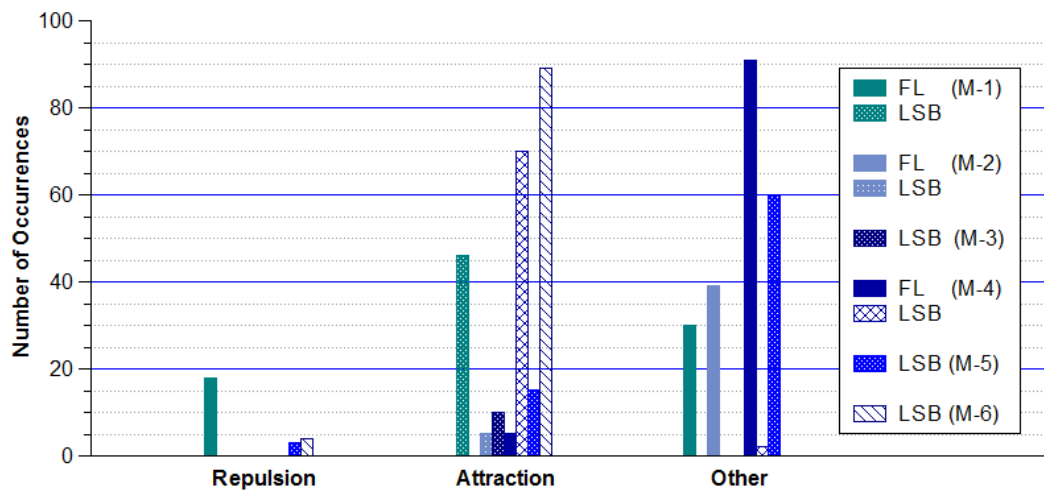


**Figure 27 Initial approach curve features for bare silica probe on mica experiments (M-1, M-2, M-3, M-4, M-5, M-6).** The x-axis indicates the type of initial feature (Figure 26) observed in the curve and the y-axis indicates the number of each occurrence that were observed for an experimental set. The columns are labeled a separate color for each experimental set with the data from the formation liquid tests (FL) designated by solid columns and the low salinity brine tests (LSB) designated by textured columns.

As Figure 27 indicates, most of the curves could be categorized as exhibiting Attraction or Other. This makes sense due to the high salt concentration of the brines. Interestingly, we see some repulsion in some of the formation liquid curves in M-1. The cause of this repulsion is unknown. It should not be due to electrostatic forces because the salt concentration is far too high.

In contrast to the approach data, we saw clear salinity-dependent differences for the adhesion in the retract curves (Figure 28). In the three experiments involving higher salinity formation liquid (M-1, M-2, M-4), we saw virtually no adhesion. However, when we followed each of these tests with the low salinity brine, all exhibited adhesion. We additionally performed three tests using only the low salinity brine (M-3, M-5, M-6). In all cases, the low salinity brine adhesion was greater than any adhesion from the formation liquid results. The lack of a systematic difference between the single and multi-brine experiments shows that the formation liquid is not modifying the surface chemistry of the substrate in any way which might affect the adhesion.

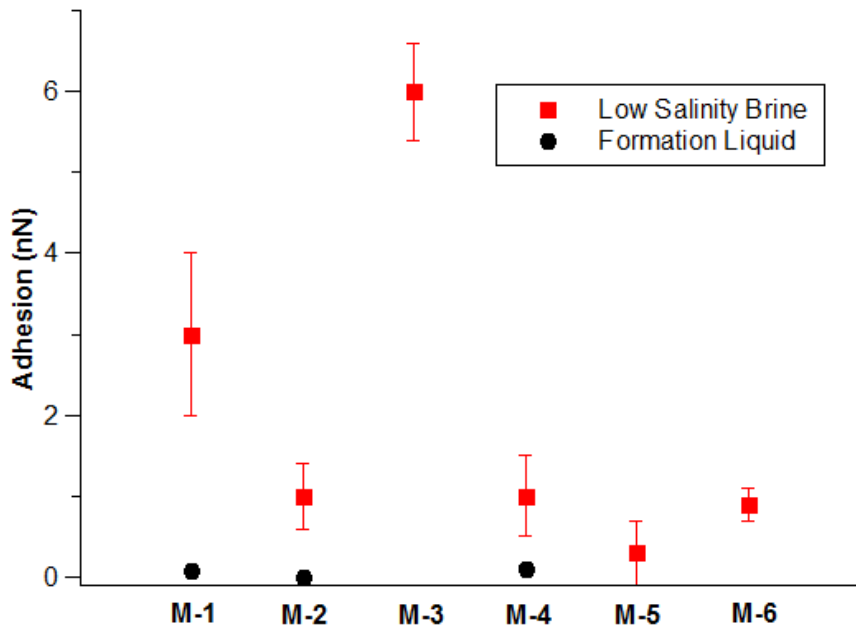


**Figure 28** Scatterplot of average results of adhesion between the bare silica probe and a mica substrate in two different brines for six experiments (M-1, M-2, M-3, M-4, M-5, M-6). In three experiments (M-3, M-5, M-6), only the low salinity brine was used. Error bars show the standard deviation of the measurements.

#### d.4. Force Spectroscopy: Rough Grain

After performing measurements on mica, a flat and model mineral surface, we began using individual mineral grains as substrates. This change introduces the complications of a rough surface topography and varied surface chemistry. These features are dependent on which grain is chosen, if it is a homogeneous mineral, if it is partially coated in clay particles, etc. Therefore, by working with rough grains we have modified our experiments to make them more similar to the interactions in an oil reservoir.

The large microsphere interacts with multiple topographical features during its descent to the substrate. This results in an approach curve with many features as well. Since there is no one surface it is difficult to determine a Debye length or calculate the

magnitude of the forces as the probe approaches. However, we can categorize the results based on the first interaction that the probe experiences, in the same way that we categorized the approach curve results in Figure 27, i.e. Repulsion, Attraction, and Other. Since this would be the first interaction that an oil droplet would experience as it approaches the mineral we think this is a justifiable way to analyze the data. Additionally, it is necessary to take measurements on multiple parts of the grain, to obtain a more generalized view of the complex surface. In this particular set of experiments, we collected multiple curves from each of five areas. Figure 29 shows the results of two experiments (R-1, R-2), denoted by the “R” in rough mineral grain substrate and chronological order. In both cases, the lower salinity brine results in more cases of repulsion than the formation liquid. In some of the experiments, we took twenty five force curves on a  $5\times 5$  grid. To show the varied forces at each location, we have color-coded the following grids from R-2 (results included in Figure 29). Both the low salinity brine and formation liquid grids were taken on the same mineral grain. The variation that occurs among the curves collected at different grid points is shown in Figure 30.

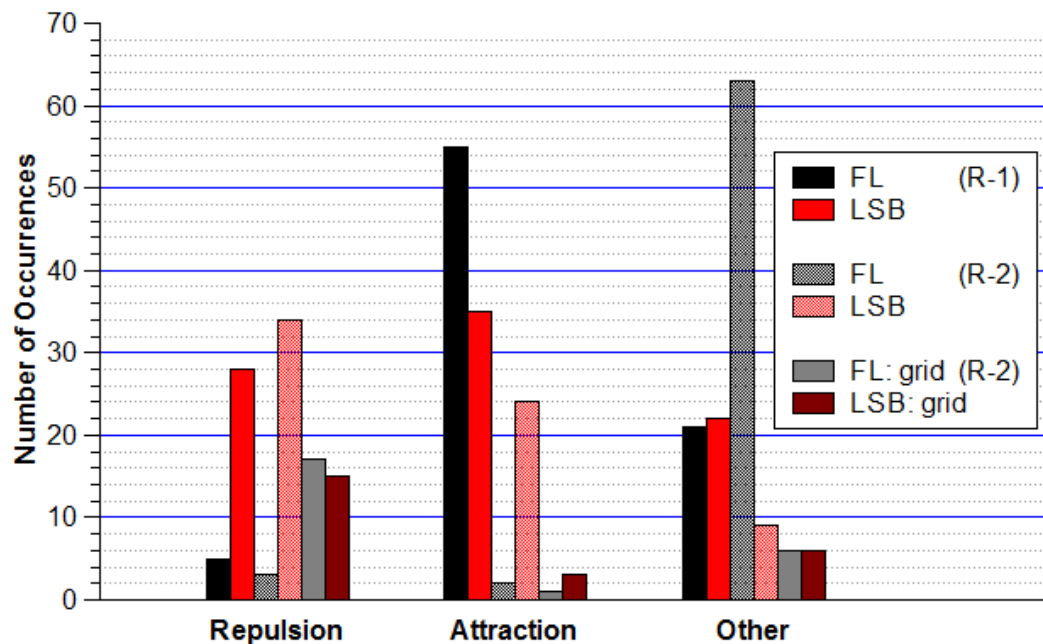


**Figure 29** Column plot indicating the number of specific features in approach curves (Figure 26) between bare silica probe and mineral grain in two different brines: formation liquid (FL) and low salinity brine (LSB). The x-axis indicates the type of feature and the y-axis indicates the number of times that feature occurred for an experimental set. The data includes two different experiments (R-1, R-2), in which multiple measurements were conducted at each of a few locations on the substrate. An additional set of R-2 data was collected over a grid of points and is designated (grid) in the plot legend.

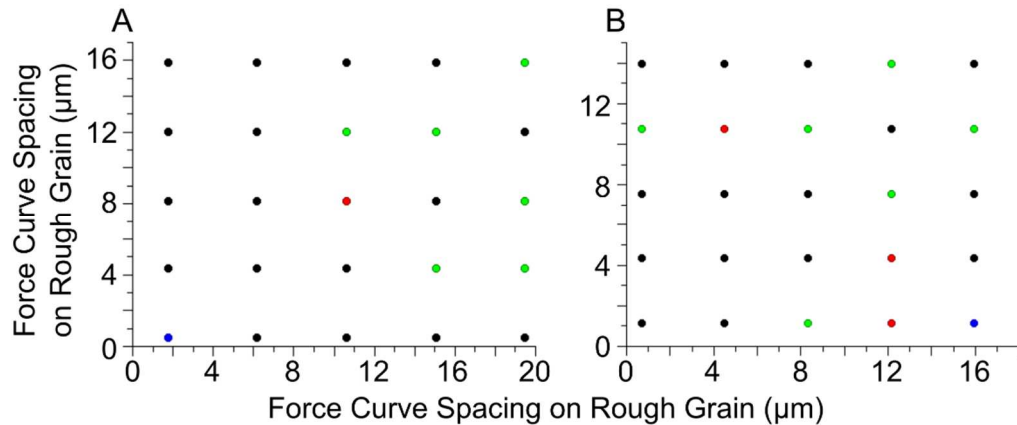


**Figure 30** Plots indicating the relative location of each force curve in a grid of points for experiment R-2. Each location is color-coded to indicate the features present in its approach curve (Figure 26). Curves were taken in formation liquid (A) and low salinity brine (B). The colors indicate repulsion (black), attraction (red), no force (green), and curves that were discarded (blue).

In contrast to the salinity dependence that we observed in the approach curves (Figure 29), the corresponding adhesion results show no clear salinity dependence between the two experiments (R-1, R-2). Additionally, they exhibit large variations at each of five locations where the data was collected (Figure 31). This variation could be due to the complex topography and chemical composition of the sample. We could even be dislodging clay particles, changing the topography with each curve. The plots in Figure 32 indicate the relative adhesion difference among different locations of the mineral grain by the area of the circles, showing clear variation as a function of location. These correspond to the grid points on the approach curves for R-2 (Figure 30).

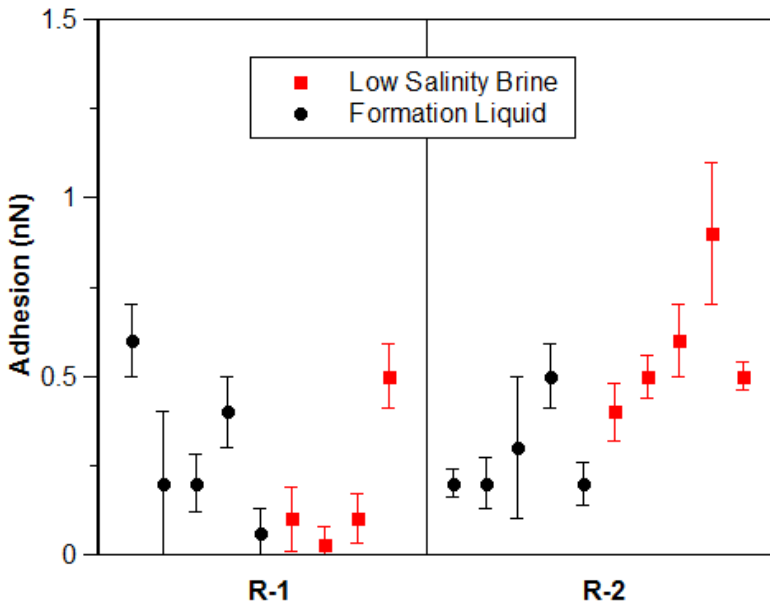


**Figure 31** Average adhesion values (and standard deviation) between a bare silica probe and a mineral grain for two experimental sets (R-1, R-2). Points are color coded to indicate brine salinity and offset horizontally to indicate average values for multiple curves taken at each of 19 locations. The results are arranged chronologically from left to right along the x-axis.

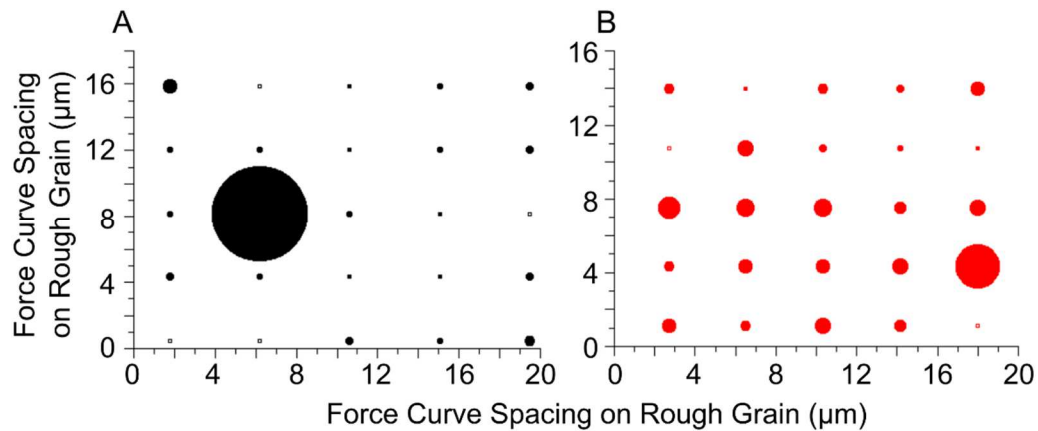


**Figure 32** Location dependent adhesion indicated by increasing circle area ranging from 0 nN adhesion (empty circle) to 4.6 nN adhesion (largest circle) in formation liquid solution (A) and low salinity brine (B) for the R-2 experiment.

The development and characterization of the bare silica colloidal probe paves the way for our functionalization experiments. During the characterization, we showed the

surface features of the probe (Figure 23) and proved that our experimental setup could reproducibly collect salinity dependent electrostatic repulsion data consistent with electric double layer theory (Figure 25). Additional experiments with more complex brines demonstrated salinity dependent trends in both the approach (Figure 27) and retract (Figure 28) curves on mica substrates. When we transitioned to using rough mineral grain substrates, we saw similar salinity dependent results in the approach curves (Figure 29), but no consistent salinity dependence in the retract curves (Figure 31). Additionally, as the adhesion points collected on a grid indicate (Figure 32), there is noticeable variability in the response of the adhesion to different locations on the mineral substrate. This is expected due to the varying topography. These results provide useful background information to the development of our custom functionalized probes.

## **Chapter 3: Crude Oil Functionalized Colloidal Probe**

### **a. Development**

To explore the interactions between crude oil and rock interfaces in the aqueous environment of a petroleum reservoir, we performed force spectroscopy measurements on rock surfaces using custom oil-coated probes in an AFM liquid cell. Over the course of our research, we employed two types of probes: wet oil and dried oil probes. To construct a wet oil probe, we employed the colloidal probe manufacturing procedure described in Experimental Methods, but added one extra step: we dipped the colloidal probe into a droplet of crude oil on a glass microscope cover slide. In this process, we aimed to coat the spherical probe only, not the cantilever, and conducted the wet oil probe experiment on the same day.

Because we encountered problems using the wet oil-coated probes (detailed in later sections), we also developed a dried oil probe technique. In this method, we dried freshly-coated wet oil probes in an oven. A variety of oven times and temperatures were tested to determine the optimal drying conditions. To determine if the oil was completely dry, we used optical images to look for oil interference patterns, which should develop as the oil layer thins (Figure 33).

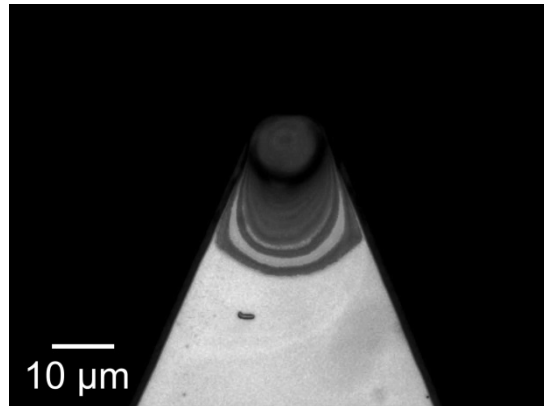


**Figure 33 Optical image of probe coated in dried crude oil clearly displaying interference patterns on the cantilever surface.**

Later, we used a more quantitative technique developed by one of the other students in our lab, William Dickinson, to determine if the oil had dried. Our technique was inspired by a principle established in beam theory and demonstrated experimentally by Cleveland et al.<sup>10</sup>: that a decrease in a cantilever's mass results in a downward shift in the cantilever's resonance frequency. We therefore measured the resonance frequency of a cantilever before and after the colloidal probe at the cantilever's end had been dipped in crude oil and at various times during the drying process. We interpreted the eventual stabilization of the resonance frequency, and thus the mass, as indication that the oil had dried (Figure 34).

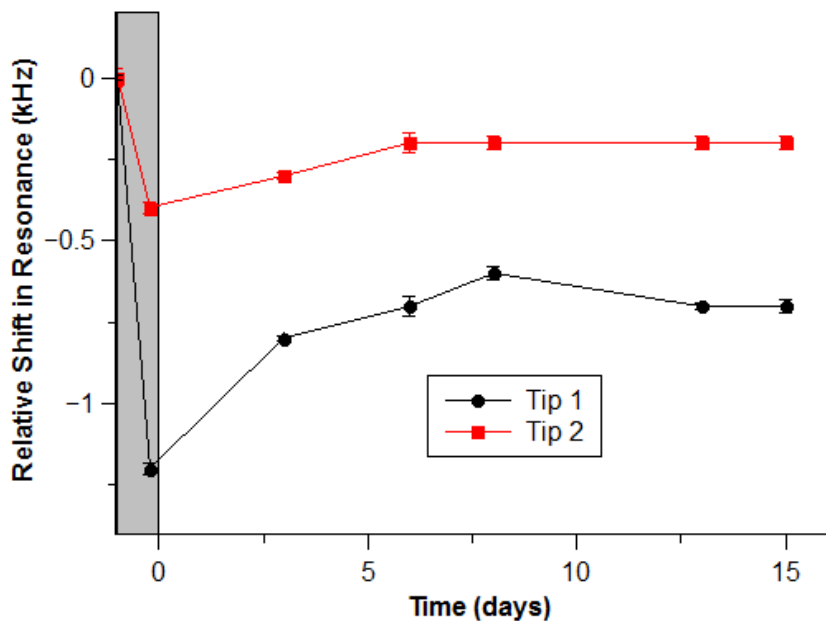


**Figure 34 Relative change in resonance value for two probes as a function of coating the probes in wet crude oil and then drying them. Resonance values for the bare silica probe and wet oil coated probe are in the grey box.**

This also provides a quantitative method for comparing the relative amount of oil on each probe. The much larger shift in resonance for Tip 1 (black) compared to that of Tip 2 (red) after being coated in wet oil indicates that more oil was applied to Tip 1. Knowing the relative amount of oil on a probe provides useful information during analysis: a thicker oil layer could result in (a) greater deformation of the probe's oil-coated surface after contact with the substrate, and (b) a different concentration of charged components on the oil surface, both of which can affect the force measurements.

Consequently, we used this method to quantitatively determine the dryness of the crude oil covered probes in later experiments. The three oils ("A", "B", and "C") used in our experiments were all provided by Shell Global Solutions International. We performed

many of our tests on mica substrates to reduce topography dependent complications in our data. However, in later experiments, we explored topography-dependent effects by performing measurements on individual sandstone grains. The preparation of the substrates and liquid cell solutions is detailed in Experimental Methods.

### b. Wet Oil-Coated Probe

In one set of our wet oil probe experiments, we used the same experimental conditions with three separate probes (experiments Wet-1, Wet-2, and Wet-3) so that the results would be easily comparable. We tested wet “A” crude oil and low salinity brine/formation liquid in sets of approximately 20 curves taken at each of five locations on a mica substrate. Of the resulting six data sets from two solutions for each of three probes, repulsion in the approach curve was only observed in the low salinity tests of one probe. Therefore, we relied on retract curve data to compare results among the different probes and solutions.

Figure 35A shows the average pull-off force (measurement technique demonstrated in Experimental Methods) at each location for each solution and probe. The error bars are the standard deviation of the averages values taken at each spot. In Wet-1, there is no systematic salinity dependent difference and little variation among the results. In contrast, Wet-2 initially displayed greater adhesion for the low salinity brine, but the adhesion gradually decreased almost to the level of the formation liquid adhesion value. In Wet-3, adhesion decreased for both salinities over time. As in Wet-2, the pull-off force for the low salinity brine was initially much higher than for the formation liquid, however, it gradually decreased to almost zero adhesion.

To review these shifts in adhesion in Wet-3 more closely, each individual force spectroscopy measurement in Wet-3 is plotted (Figure 35B) with boxes indicating the test groups presented in Figure 35A. Figure 35B shows that the first spectroscopy measurement in each formation liquid test group has a lower pull-off value than the following measurements. The low salinity brine results, which were collected after the formation liquid, show gradually decreasing adhesion that changes drastically among the first three test locations until it stabilizes at a near-zero force. We speculate that during first contact of the probe and substrate at each location the oil coating on the probe remains stable. Afterwards, the oil-coated probe ruptures the water film on the surface leaving behind a droplet of oil on the mica, and leading to increased adhesion in all following measurements as the oil coated probe interacts with an oil-coated substrate. The low salinity brine results show a decrease in adhesion at each of the first few locations. This shows the oil coating interacting with an increasingly smaller oil bridge as its oil coating gradually pulls off. Eventually, enough of the oil pulls off the surface to stabilize the adhesion measurement at near-zero force. This explanation is consistent with the work of Basu et al.,<sup>33–35</sup> who demonstrated various salinity and pH conditions in which wet crude oil might pull off a coated AFM probe to adhere to a substrate during a force spectroscopy experiment. They showed that when a wet oil coated probe interacts with a surface, the rupture of the water film on the substrate will lead to (a) a probe leaving oil behind on a surface and (b) greater adhesion than the pre-ruptured interactions. Together, these results suggest an unstable system with an oil layer that can vary each time the probe contacts the substrate. Due to the variable nature

of this probe, we sought a more robust coating that would retain the charged components of crude oil.

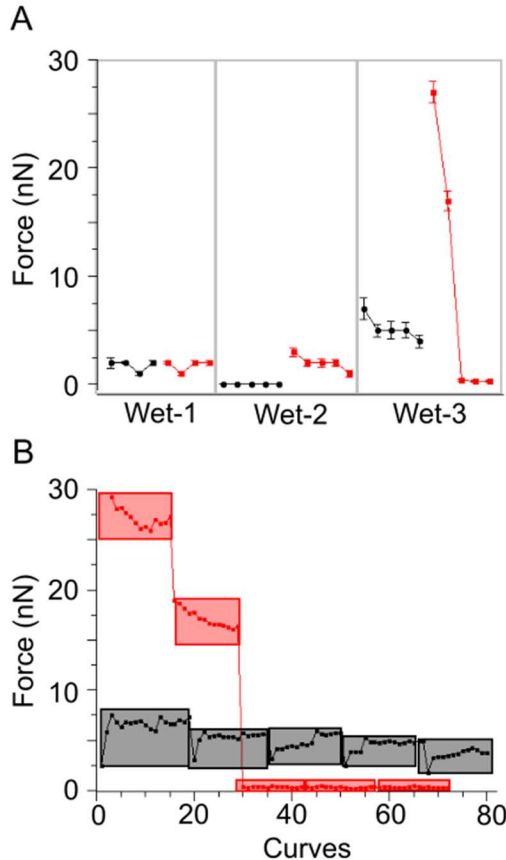


**Figure 35** Average pull-off force results from the retract curves of three experiments (Wet-1, Wet-2, Wet-3) with error bars to represent the standard deviations.

Experiments performed in formation liquid are designated with black circles and low salinity brine are designated with red squares. In each case, multiple measurements were taken at each of multiple locations on the substrate (A). Additionally, each individual measurement is plotted for Wet-3. The boxes indicate which points were collected on each substrate location (B).

### c. Dried Oil-Coated Probe

To explore the capabilities and limitations of our dried oil-coated probes, we tested them in a variety of systems of increasing complexity (each detailed in the following separate sections). We started by using flat mica substrates and simple brines (1 mM

and 10 mM NaCl) so that we could test the effects of three different crude oils, i.e. “A”, “B”, and “C”. Then we transitioned to more reservoir specific experiments by using mica, “A” oil, and brines modeled after the naturally occurring formation liquid and injection brine, i.e. low salinity brine. Formation liquid was present in the “A” reservoir before drilling and low salinity brine was used in the “A” reservoir oil recovery. Finally, we repeated the experiments on rough mineral grains from the “A” reservoir so that in our final results all materials—oil, brines, rock—were from the same petroleum reservoir.

### **c.1. Mica Substrate**

#### **c.1.1. Simple Salt Brines**

To study the effects of salinity and oil type on oil-substrate adhesion, we conducted the majority of our dried oil-coated probe experiments in both 10 mM and 1 mM NaCl brines on mica substrates. The flat surface of mica reduces the possibility of topography-induced artifacts. We compared approach curve results in these experiments, in which we could observe the interaction forces between probe and substrate prior to contact with the surface. This force data indicated how the charged components in the oil, i.e. those influenced by adjusting the injection liquid salinity, interacted with the probe and substrate. In contrast, adhesion measurements collected from retract curves are a function of both short range van der Waals and long range electrostatic forces. However, these results can be significantly affected by the

deformation of the oil-coated probe data. Since this deformation can vary greatly from curve to curve, adhesion data was deemed less reliable.

### c.1.1.1. “A” Oil Coated Probes

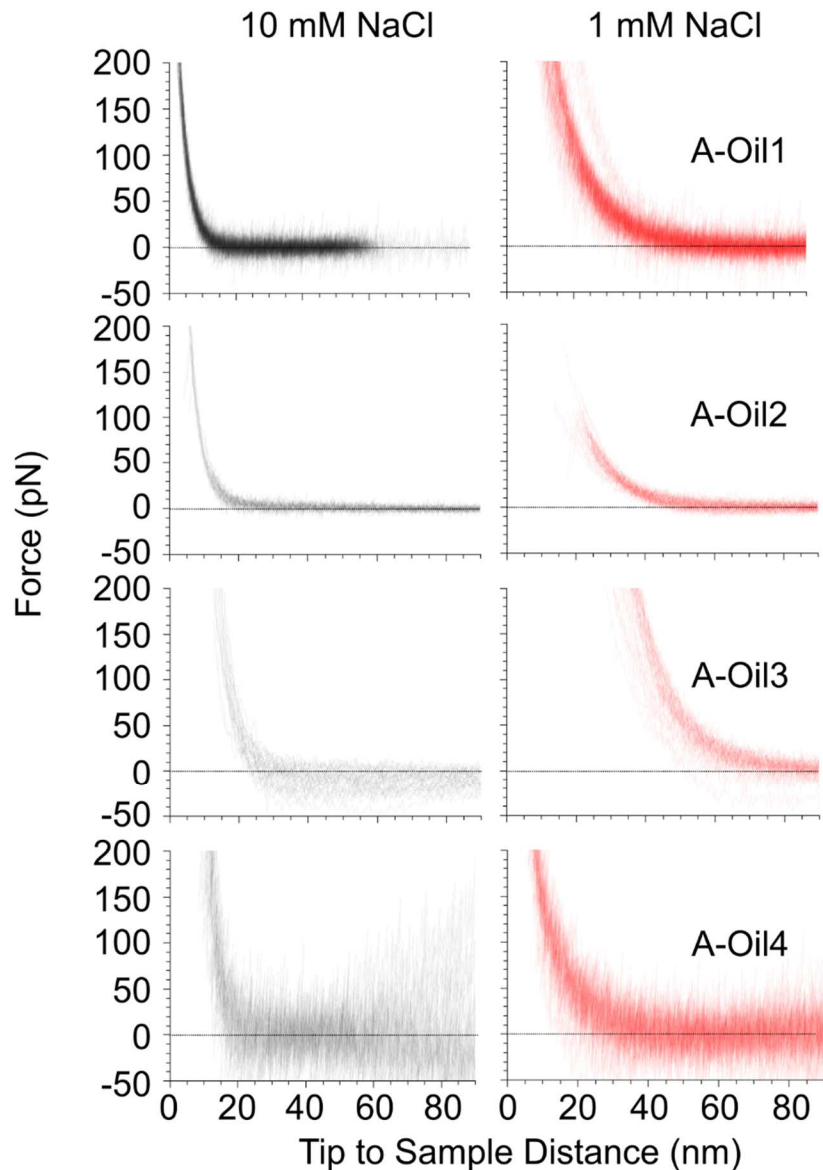


**Figure 36 Approach curves collected from four dried “A” oil coated probes in two different liquid cell solutions (1 mM and 10 mM NaCl) on mica.**

For the dried “A” oil, we conducted four experiments (A-Oil1, A-Oil2, A-Oil3, A-Oil4) with four different probes. All four probes exhibited electrostatic repulsion for both solution molarities. Since we know that the mica was negatively charged in these liquid cell solutions due to its isoelectric point,<sup>104</sup> this shows that the “A” crude oil was also negatively charged throughout the experiment. As expected by electric double layer theory, we see greater electrostatic repulsion (technique for measuring repulsion in Experimental Methods) in the lower salinity (1 mM NaCl) brine. This is manifested by the greater force (y-axis) at each point of the repulsive region along the x-axis, for the 1 mM compared to the 10 mM NaCl data (Figure 36). Additionally, there is some variation in the magnitude of surface charge on the different oil probes. Some start to exhibit repulsion farther from the surface than others. This may be due to the quantity of oil on the surface, which corresponds to the quantity of charged polar groups. Furthermore, more oil on the surface might lead to a thicker, deformable surface which becomes flattened after first contact with the mica substrate. A flattened surface would lead to interaction between two plane geometries instead of a plane and sphere, which would lead to greater interaction forces. These results show that our dried oil coated probe technique can measure the charged interactions between crude oil and a mineral surface as a function of distance and solution molarity. It also shows that these probes exhibit reproducible results over many measurements, making them versatile tools to explore the interactions in a petroleum reservoir.

### c.1.1.2. “B” Oil Coated Probes

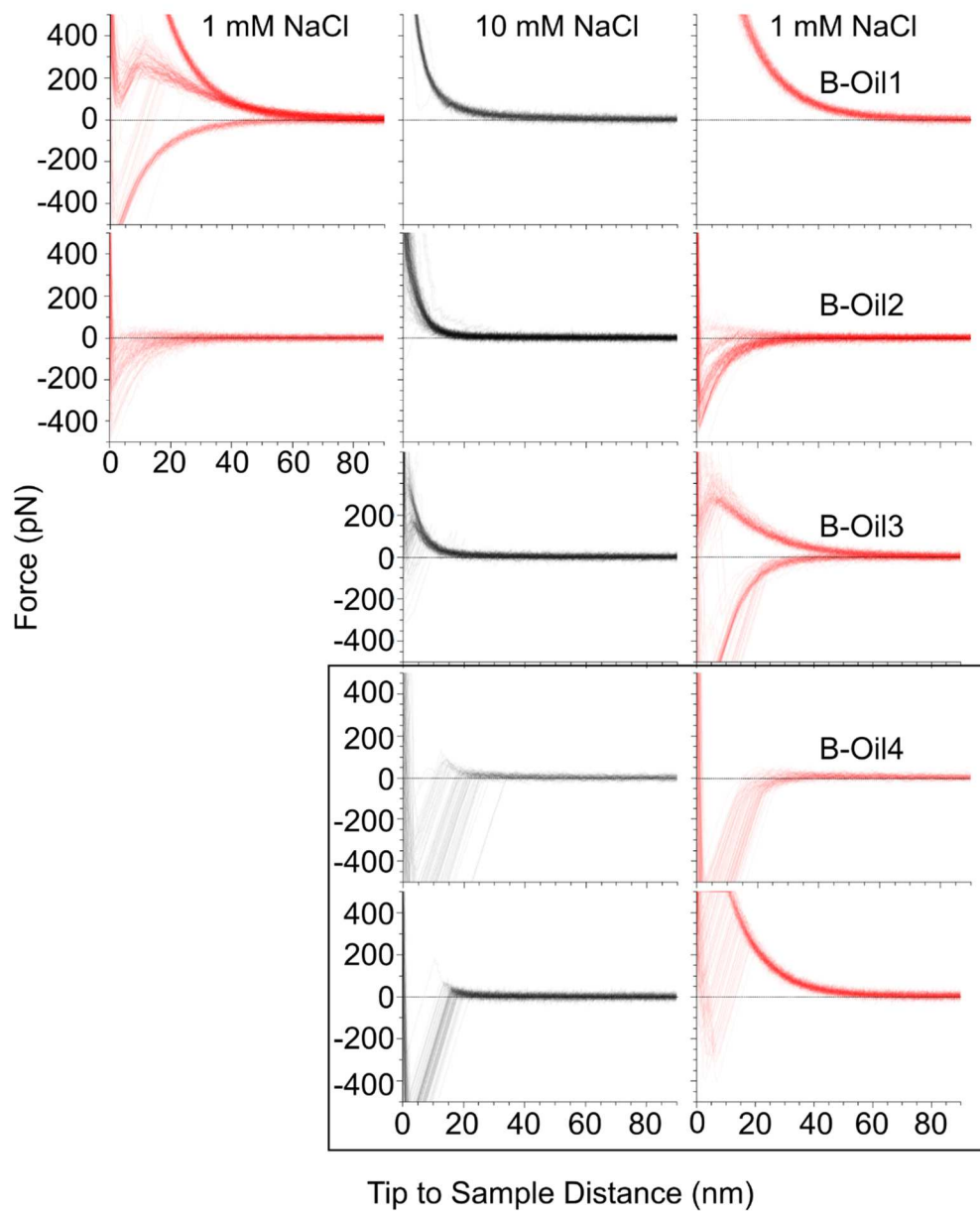


**Figure 37 Approach curves collected in four experiments (B-Oil1, B-Oil2, B-Oil3, B-Oil4) from four dried “B” oil probes in two different liquid cell solutions, 1 mM (red) and 10 mM (black) NaCl. The plot placement indicates the order in which the experimental data was collected: from left to right, showing that some probes were tested in the same solution molarity twice. The box around B-Oil4 shows the four experiments that were performed with the same tip in the order 10 mM/1 mM/10 mM/1 mM.**

In some of the experiments we performed with “B” oil, we alternated the order in which we used the solution molarities to determine if the order in which the probes were exposed to the different brines would modify their surface chemistries and affect the resulting forces. We performed measurements in the order 1 mM/10 mM/1 mM for two probes, 10 mM/1 mM for one probe, and 10 mM/1 mM/10 mM/1 mM in the last case (Figure 37). While long range attraction was observed for each probe, some approach curves displayed repulsion as well. For example, in the case of B-Oil1, the interactions first displayed attraction in 1 mM NaCl before transitioning to repulsive for the rest of the experiment. For B-Oil2, only attraction occurred in the 1 mM NaCl solution and only repulsion occurred in the 10 mM NaCl solution. B-Oil3 exhibited only repulsion at 10 mM and both long-range attraction and repulsion in the 1 mM NaCl solution. For B-Oil4, the forces were at first repulsive (10 mM NaCl), then attractive (1 mM NaCl), then repulsive again (10 mM & 1 mM NaCl).

These results are interesting for multiple reasons. In all cases, these are long range forces occurring farther than a few nanometers from the surface. This distance indicates that they are electrostatic in nature. The surface charge of the oil may therefore be changing during the experiment since we do not expect the mica's isoelectric point to change when exposed to these aqueous solutions. Also, the process causing a switch between attraction and repulsion is reversible. Furthermore, attraction only occurs in the 1 mM NaCl solution, indicating that the differing solution molarity is likely contributing to the changing surface charge. To obtain more information about what

might be occurring in these force curves, we performed the experiments using a third crude oil.

### c.1.1.3. “C” Oil Coated Probes

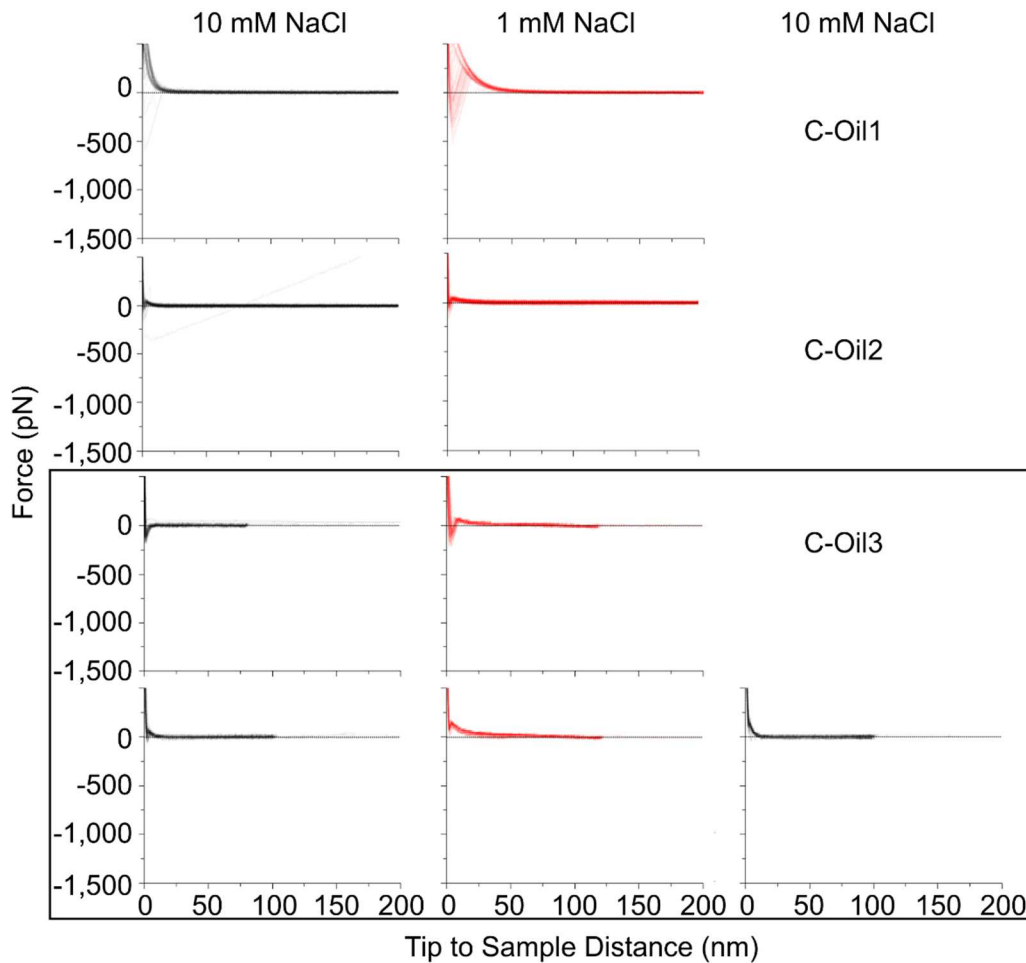


**Figure 38 Approach curves collected from three dried “C” oil probes in two different liquid cell solution molarities (1 mM and 10 mM NaCl). The order of the experiments is shown by the plot placement from left to right. For one experiment, C-Oil3, the same probe was tested five times in the following solution order: 10 mM/1 mM/10 mM/1 mM/10 mM NaCl. Its experiments are designated by the surrounding black box.**

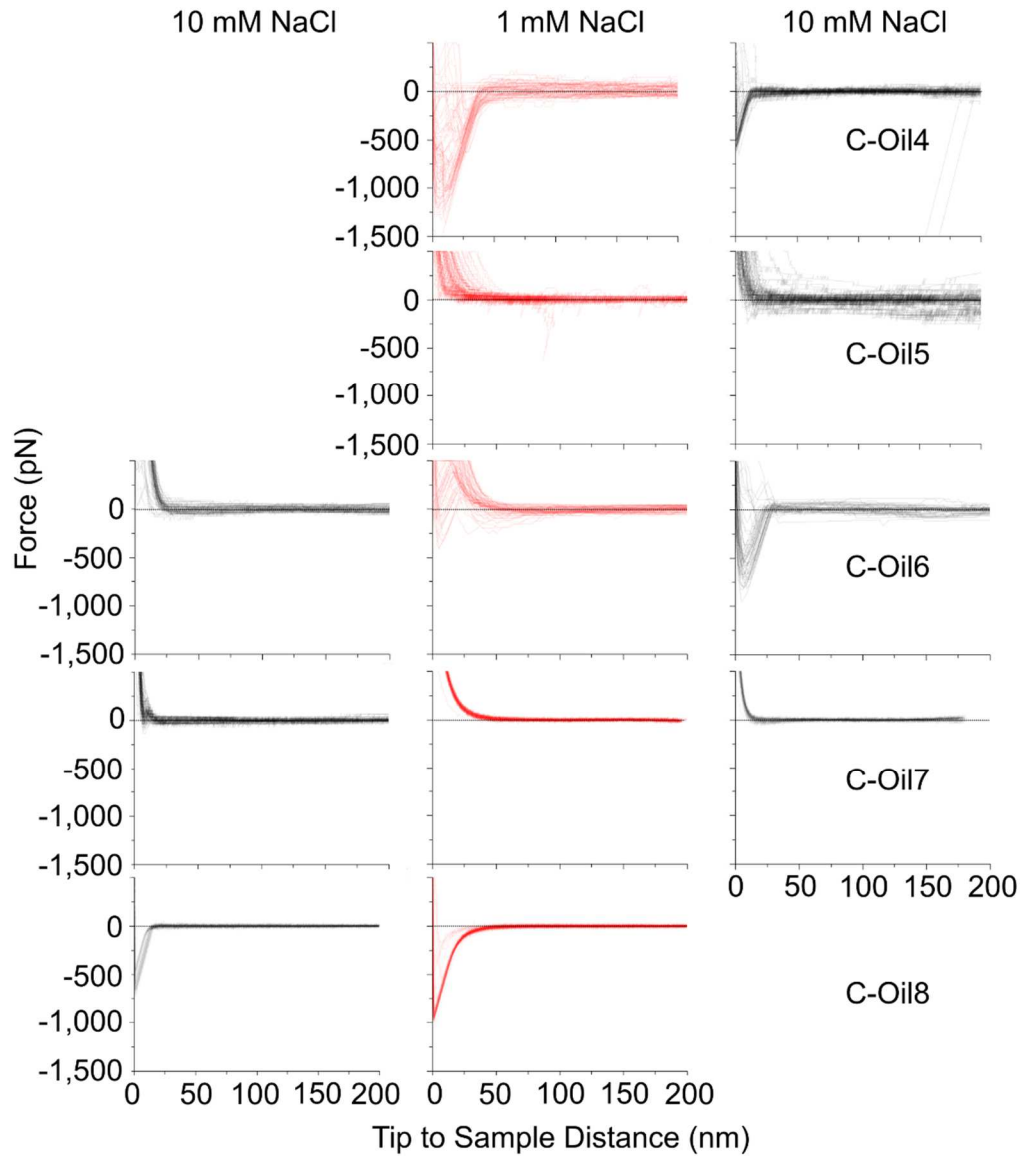


**Figure 39 Approach curves collected from five dried “C” oil coated probes in two liquid cell solutions (1 mM and 10 mM NaCl). The order of the experiments is shown by the plot placement from left to right.**

The eight dried “C” oil coated probes exhibited a variety of behaviors. Some probes exhibited repulsion that varied with solution molarity (C-Oil1, C-Oil2, C-Oil5, C-Oil7). In other cases, there were instances of both long range repulsion and attraction (C-Oil3, C-Oil6), while some probes showed only attraction (C-Oil4, C-Oil8). The difference of

these results from the lack of long range attraction in the “A” oil results indicate that oil recovery yields are directly affected by the types of crude oil and aqueous solution present in the reservoir. These results will be analyzed in greater depth in the Discussion.

### c.1.2. Complex Salt Brines

In our complex salt brine experiments, we aimed to keep the brine composition as close to that observed in a real reservoir as possible so that later injection well testing in the field could be compared to our data. In three experiments, we focused on products from a single reservoir: “A”. We used crude oil, a recipe for the formation liquid from the “A” reservoir, and a low-salinity brine recipe to simulate the injection liquid being used in the field. To reduce the possibility of topography-induced artifacts, we performed these three experiments on mica.

Of all our complex salt brine experiments, only some of the curves from the low salinity brine in one experiment exhibited any electrostatic repulsion, and of these curves, all forces were less than 17 pN. Based on the salinity of the brines, the expected Debye length for the low salinity (28 mM) brine should be less than 2 nm and even smaller for the formation liquid (4 M). Although a Debye length of less than 2 nm is not impossibly small to measure with an AFM under the right circumstances, e.g. if the surface is highly charged, it is still an extremely difficult experiment. Therefore, our low force values are not surprising.

Due to the near-complete lack of repulsion in the approach curves, we relied on the retract curves to compare forces among these experiments (MicaC-1, MicaC-2, MicaC-

3). The experiments are denoted by the mica (M) substrate, the “C” in complex brines and the chronological order of the experiments. In two cases, the low salinity brine produced greater adhesion, and in one experiment there was no observed salinity dependence (Figure 40). Greater adhesion as a function of salinity can sometimes occur when high salinity leads to greater shielding of the repulsive electrostatic double layer, making the attractive van der Waals interactions the dominant force. However, these results showed greater adhesion for low salinity, which is contrary to our expected outcome. Additionally, the only experiment in which we recorded any type of repulsion was the low salinity approach curves in MicaC-1, which showed no difference between the solutions.

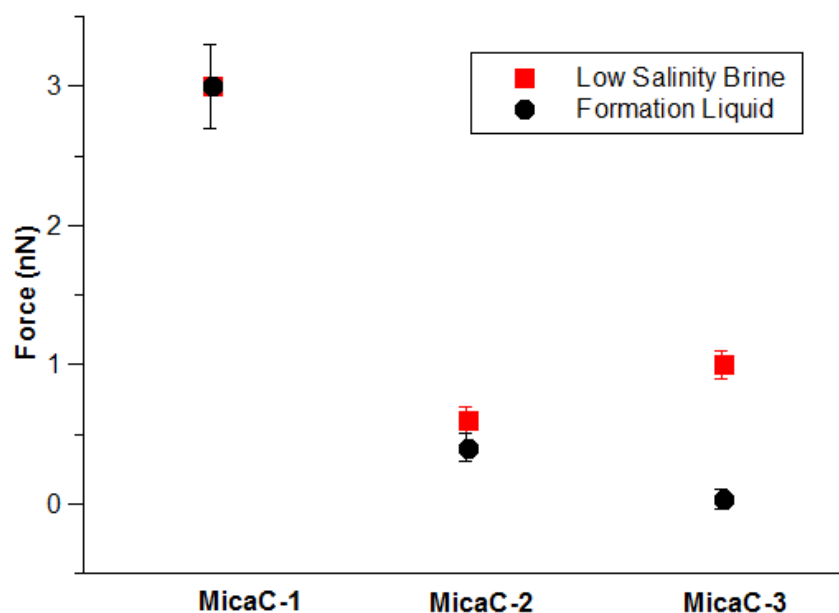


**Figure 40 Salinity dependent trends in adhesion between dry oil-coated probes and a mica substrate for three different experiments (MicaC-1, MicaC-2, MicaC-3).**

In MicaC-3, additional results were collected over 25 grid points and plotted, with the magnitude of the adhesion indicated by the relative area of each circle (Figure 41). The similar size of all the circles for each salinity indicates a homogeneous distribution of force over the mica surface and a clear salinity dependence. Since a mica substrate was employed, we expected the results to be similar on multiple areas due to the lack of topography. It is therefore unsurprising that both the multiple measurements averaged from a few locations (Figure 40) and the grid of measurements (Figure 41) both showed the same salinity-dependent trend. The consistency of these two methods for collecting data are important for two reasons: (1) they confirm that the mica substrate is as homogenous as we expect, and (2) they highlight the importance of sampling measurements over a grid to check for topography-dependent effects, which become more relevant when testing on a more heterogeneous substrate, e.g. a sandstone grain.

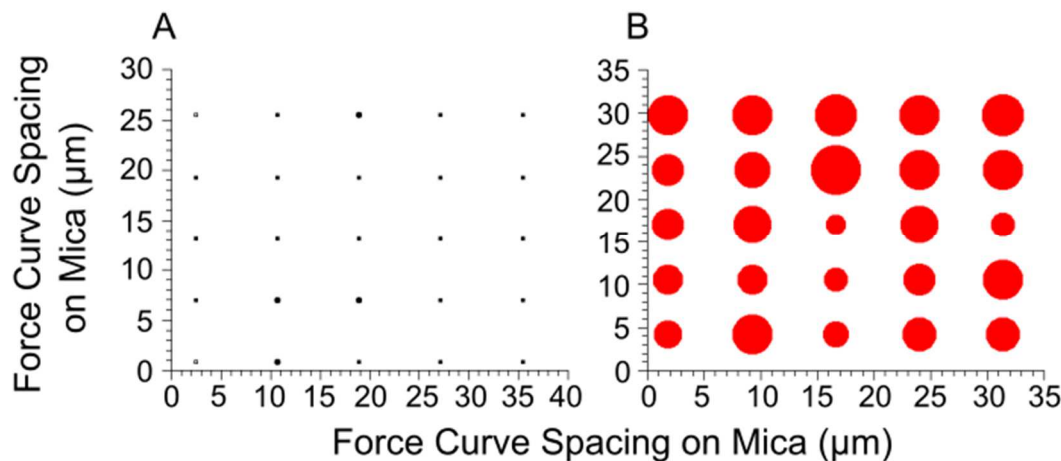


**Figure 41** The plots use the circle area to indicate the relative difference in adhesion for experiment MicaC-3 for the formation liquid (black circles in “A”) and low salinity brine (red circles in “B”) results. The adhesion ranges from 0 nN (empty circle) to 2.4 nN (largest circle in “B”).

## c.2. Rough Mineral Grain Substrate

By developing the dried oil coated probe, we aimed to construct a tool that could be used to systematically test the interactions between oil and mineral from a particular oil well in order to introduce a new method for predicting the best water injection fluids to use in a reservoir. After developing the dried oil coated probe for this purpose and proving its usefulness on flat mica substrates, we began preliminary testing on rough mineral grains. Our first results set the groundwork for this technique and addressed some of the unique challenges of performing force spectroscopy measurements on these complex samples.

To perform our tests, we used crude oil, mineral grains, formation liquid, and low salinity brine all from the same “A” oil reservoir. The surface topography of the native mineral grains is more varied than mica. Consequently, when the colloidal probe approached a mineral grain, the probe could encounter a different contact area with each location on the sample. The situation is further complicated by the presence of clay particles, which could potentially coat the surface of the grains. In addition, although the dried oil probe has a more stable surface than the wet oil probe, it could deform in different ways based on the type of flat, curved, or jagged surface features that it encounters. These added challenges to the experimental setup necessitate a thorough description of the types of variation that we found in the curves and how we categorized and quantified them.

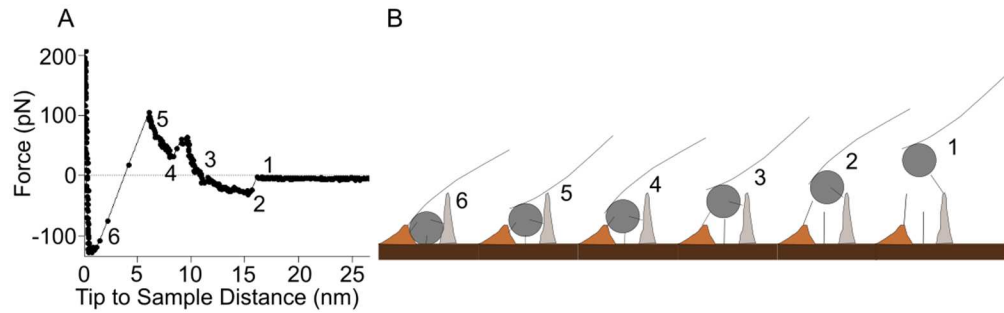


**Figure 42 Sample approach curve (A) taken with dried oil coated probe on a mineral grain. Schematic (B) of possible surface topography that could have contributed to each area of repulsion and snap-down in “A”. Both “A” and “B” have corresponding numbers to indicate what features might lead to each part of the approach curve. The arrows indicate the repulsion and attraction forces working on the probe from each surface feature.**

In some cases, the rough topography of the mineral grains resulted in clearly distinctive interaction regions of the curves. For example, Figure 42A exhibits an approach curve between a dried oil coated probe and a mineral grain substrate. There are three different regions of repulsion that the probe encountered during its approach prior to surface contact (Figure 42A, areas 1, 3, 5). Additionally, there are three clear snap-downs (Figure 42A, areas 2, 4, 6). Figure 42B is a sketch of sample features that the probe might encounter to result in this type of force curve.

Electrostatic repulsion and van der Waals attraction have different distance dependences. Therefore, with a rough surface the probe would move through areas with greater or lesser repulsion and attraction based on how close it was to various features. The presence of these interactions is more pronounced in some cases (Figure 42), but in other cases a curve may appear smooth but still be impacted by the unexpected geometry, as indicated by its lack of the expected exponential trend. Further complications can arise if the interaction between a jagged point on the sample and the

probe results in such a weak electrostatic interaction that the dominant force is van der Waals attraction. In this case, any salinity dependent trend in the electrostatic forces would be concealed.

Since the mineral samples are from an actual reservoir, understanding their complex interactions is crucial to understanding the behavior of a natural oil/mineral system. Due to the varied interactions between the probe and substrate, we categorized the different results rather than comparing the magnitude of the forces. Regardless of whether the curve exhibited stepped data (Figure 42) or a smooth curve in the approach, we categorized the results by which feature—repulsion, attraction, or no deflection until surface contact—occurred first in the curve, because this would be the first interaction that the oil droplet would encounter in the reservoir.

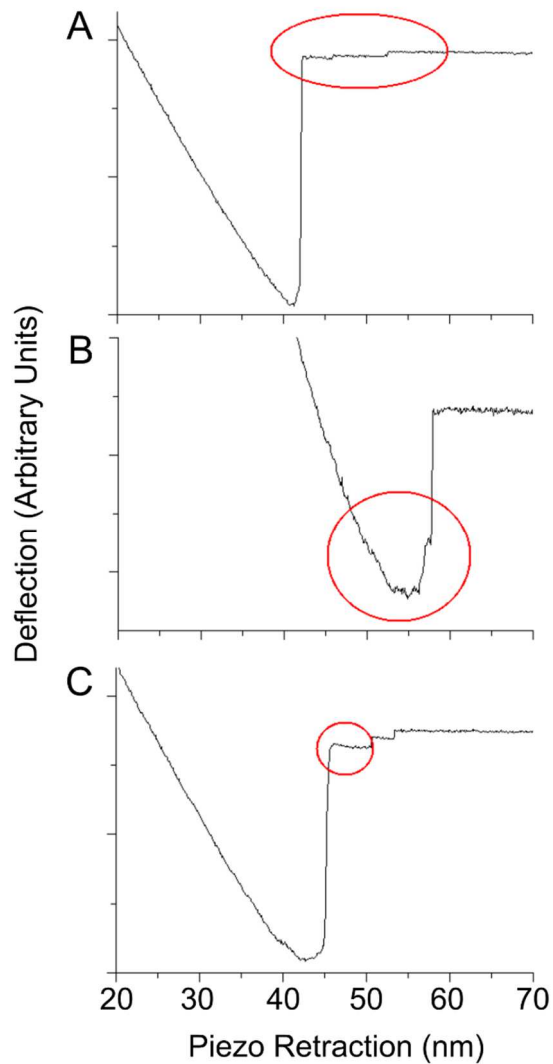


**Figure 43 Various features observed in the pull-off curves of force spectroscopy measurements taken on rough mineral grains. Features include steps (A), multiple pull-offs (B), and unexpected repulsion (C).**

When a probe is retracted from the mineral substrate, various results are also possible.

For example, the probe can release gradually from the surface, resulting in stepped features (Figure 43A), multiple pull-offs (Figure 43B), or stepped features with unexpected repulsion (Figure 43C). Despite these variations, we are still able to

quantitatively measure the maximum deflection of the cantilever for the adhesion values.

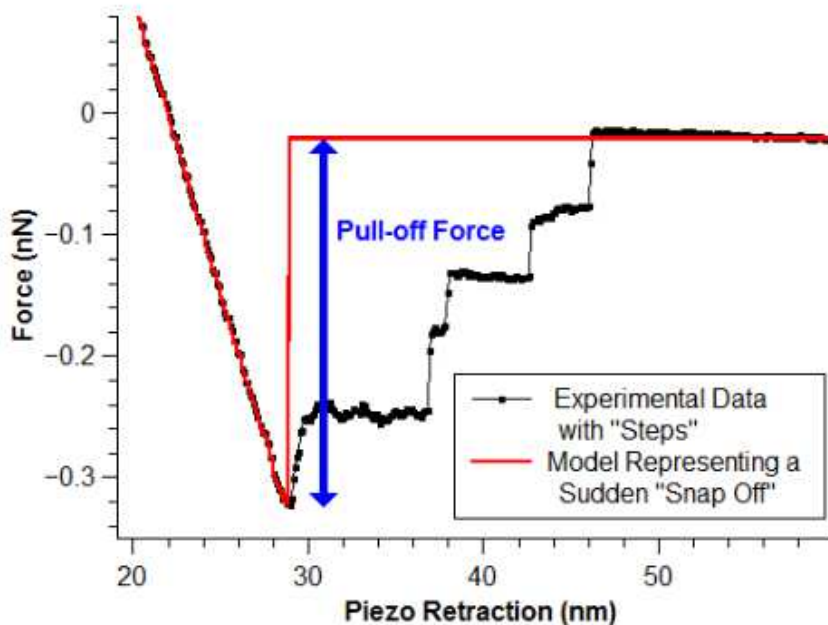


**Figure 44 Complex retract curve between a probe with dried “A” oil coating and an “A” mineral substrate in 10 mM NaCl solution (black) and a model retract curve exhibiting a clean and sudden snap-off (red).**

Figure 44 provides examples of an experimental stepped retract curve (black) and a model retract curve with a clean snap-off (red). In both curves, there is a maximum downward deflection of the cantilever from the position of the relaxed cantilever. We measured this maximum downward deflection (blue arrow, Figure 44) and used it as a comparison of the adhesive pull-off force between probe and sample. Using the same definition for both the model and complex retract curve is practical because in both cases this value quantitatively indicates the amount of adhesion it would take to remove an oil droplet from the substrate surface.

### c.2.1. Simple Salt Brines

We performed three experiments (RoughS-1, RoughS-2, RoughS-3) using simple salt brines (1 mM and 10 mM NaCl), dried “A” oil probes, and rough “A” mineral grain substrates. The experimental names denote the “Rough” mineral grains, the “S” in simple salt brines and the chronological order of the experiments. It was difficult to apply simple exponential fits to the repulsion in these approach curves, so we compared the effects of salinity dependence in these experiments by calculating the percentage of curves that exhibited repulsion. Table 1 shows that in all three experiments, fewer curves exhibited repulsion in the 10 mM NaCl solution than the 1 mM NaCl solution. Electric double layer theory predicts that the electrostatic repulsion should be diminished for higher salinity solutions. If the force diminishes beneath the sensitivity limit of our cantilever, it would be undetectable. This occurrence could explain the lower percentages of repulsion for our 10 mM NaCl experiments.

**Table 1 Percentage of curves exhibiting repulsion in 10 mM and 1 mM NaCl liquid cell solutions. The total number of curves tested for each solution molarity is included in the Curves column.**

Experiment	10 mM	1 mM	Curves
RoughS-1	23%	100%	50-53
RoughS-2	44%	93%	61-62
RoughS-3	97%	100%	38-61

We also measured the adhesion in these curves and plotted the results to show the average adhesion at each location where data was collected on the substrate (Figure

45). These results show no difference in the magnitude of adhesion as a function of salinity. However, they do show greater variability in the 1 mM NaCl measurements. Since the 1 mM NaCl approach curves show more instances of repulsion than the 10 mM NaCl results, there might be more instances of competition between the repulsive electrostatic forces and attractive van der Waals, leading to greater variation in the retract curves as the probe interacts with a rough topography.

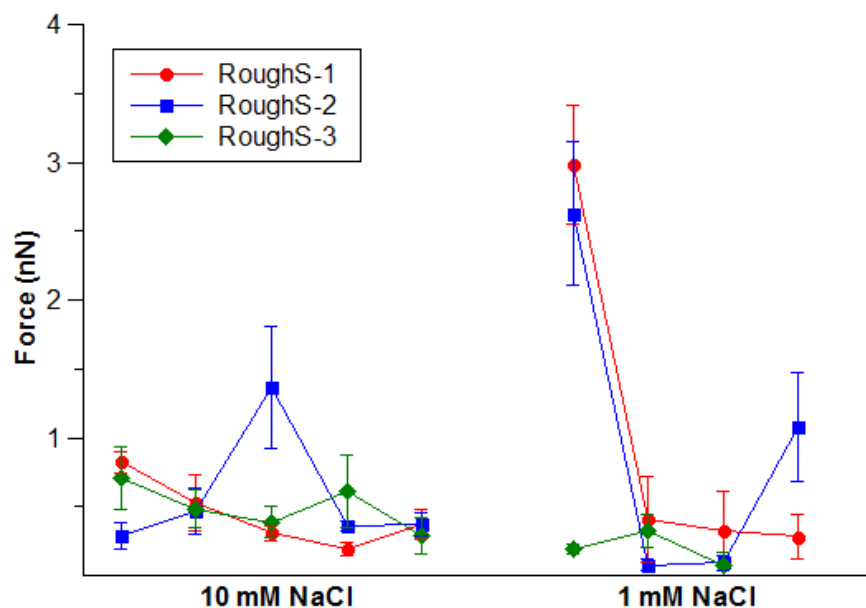


**Figure 45** Adhesion between dried “A” crude oil coated probes and mineral grain substrates in three experiments (RoughS-1, RoughS-2, RoughS-3). The average adhesion value at each of multiple locations on the mica is represented by scatter points and the standard deviation is represented by the error bars. The chronological order in which the data was collected is demonstrated by the left to right ordering of the data.

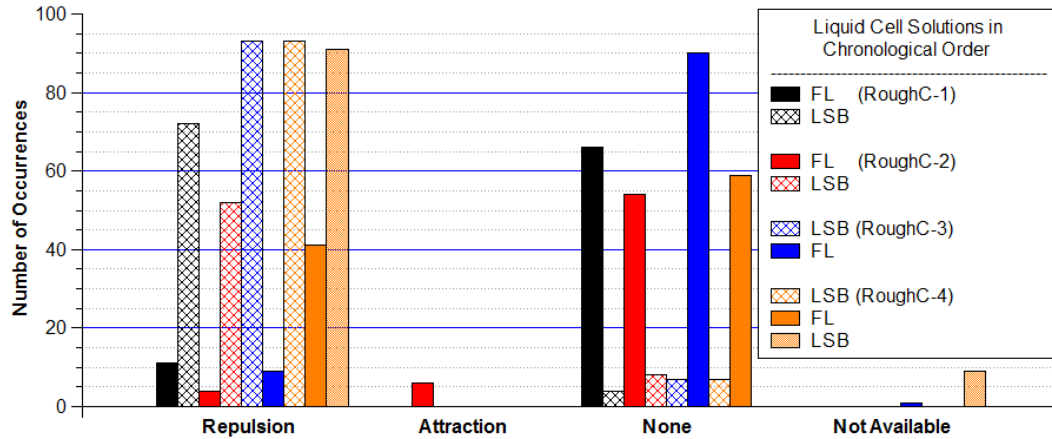
### c.2.2. Complex Salt Brines

The force measurements performed between a dried oil coated probe and a mineral grain in a complex brine present a unique combination of challenges. Since the

measurements were conducted in formation liquid (4 M, Debye length 0.15 nm) and low salinity brine (28 mM, Debye length 1.8 nm), we expected to, possibly, only observe electrostatic repulsion in the low salinity brine. Repulsion in the formation liquid would indicate an unexpected surface chemistry effect or that the probe encountered surface features that deformed or moved upon contact, e.g. clay platelets. Additionally, since the measurements were performed on rough mineral grains, we expected to encounter some curves with stepped features in their approach. Even if the features are not obviously stepped, they may still exhibit non-exponential behavior as the probe gradually moves through alternating regions of dominant electrostatic and van der Waals forces. Consequently, as in the experiments with simple brines, we categorized the approach curves based on the type of feature that first developed during the approach.

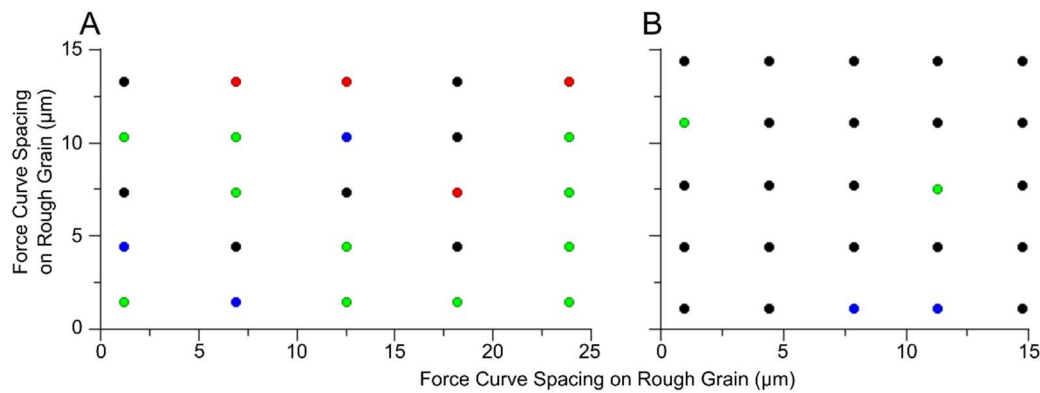
In total, we performed four experiments (RoughC-1, RoughC-2, RoughC-3, RoughC-4) using dried “A” oil coated probes, “A” mineral grains, and complex salt solutions. The experimental names are denoted by the “Rough” mineral grains, the “C” in complex salt brines, and the chronological order of the experiments. For two of the experiments, we tested the formation liquid first, then the low salinity brine. In another experiment, we tested the low salinity brine first, then the formation liquid. In the fourth experiment we used low salinity brine, then formation liquid, then low salinity brine. In each case, we performed approximately twenty force measurements in each of four or five locations. As expected, repulsion occurred more frequently in the low salinity brine (textured columns in Figure 46) than in the formation liquid (solid columns in

Figure 46), a trend that occurred regardless of the order that the solutions were used in the experiment. These results were even reproducible after cycling through low salinity brine-formation liquid-low salinity brine (orange columns, Figure 46).



**Figure 46 Initial features in the approach curves for experiments RoughC-1, RoughC-2, RoughC-3, RoughC-4. These are the results of measurements performed at each of five locations in both formation liquid (FL) and low salinity brine (LSB).**

Additionally, in RoughC-2 we performed one extra set of measurements spanning a 5 by 5 grid of curves to observe how much the results varied over the rough surface of the mineral grain (Figure 47). Overall, the results followed the same trend as the measurements taken on four or five isolated locations: more repulsion was observed in the low salinity measurements. However, the grids also show the varied response of different areas of the rough mineral surface. Consequently, these results suggest that performing measurements on a grid provides a more accurate picture of the interactions on a rough mineral grain.



**Figure 47 Approach curve features at each grid point for RoughC-2 including formation liquid (A) and low salinity brine (B). The colors indicate repulsion (black), attraction (red), no force (green), and the curves which were discarded (blue).**

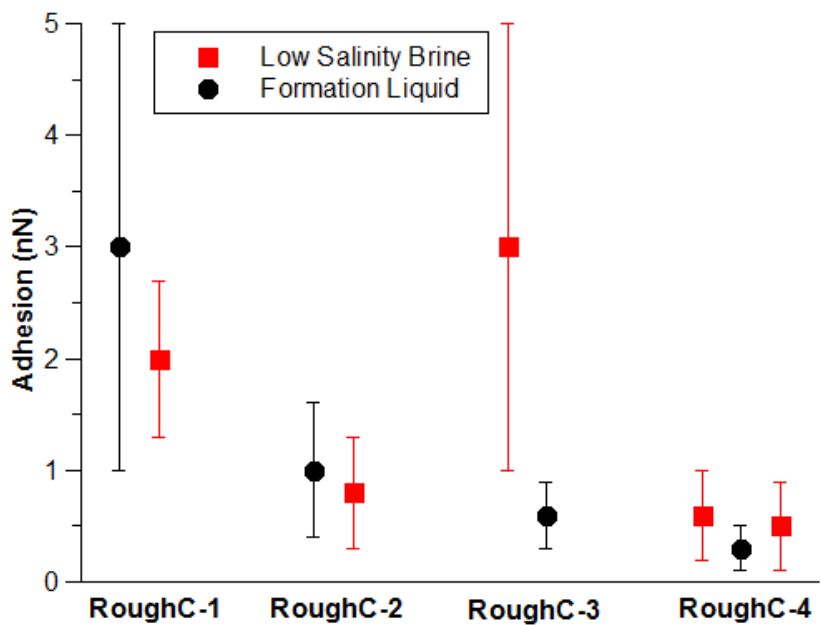


**Figure 48 Adhesion between four dry oil-coated probes and a mineral grain substrate with the average value of curves taken at five locations each for experiment (RoughC-1, RoughC-2, RoughC-3, RoughC-4) and salinity.**

The approach curve results displayed a consistent dependence on brine salinity across four different experiments. In contrast, their corresponding retract curves exhibited the greatest adhesion in the first set of measurements for each probe regardless of the order

of solution salinity (Figure 48). To determine the reason for both the large standard deviation in the data and the changing trends in the adhesion, we performed additional analyses. First, we explored possible reasons for the large standard deviation by plotting the retract data for the 25-curve grid collected in RoughC-2 (Figure 49, based on approach curve results in Figure 47).

The magnitude of the adhesion is indicated by the circle area at each grid point. Although the formation liquid (Figure 49A) exhibits greater overall adhesion than the low salinity brine (Figure 49B), there is noticeable variation among the points. Therefore, the large standard deviation likely reflects the probe's interaction with the rough surface features.

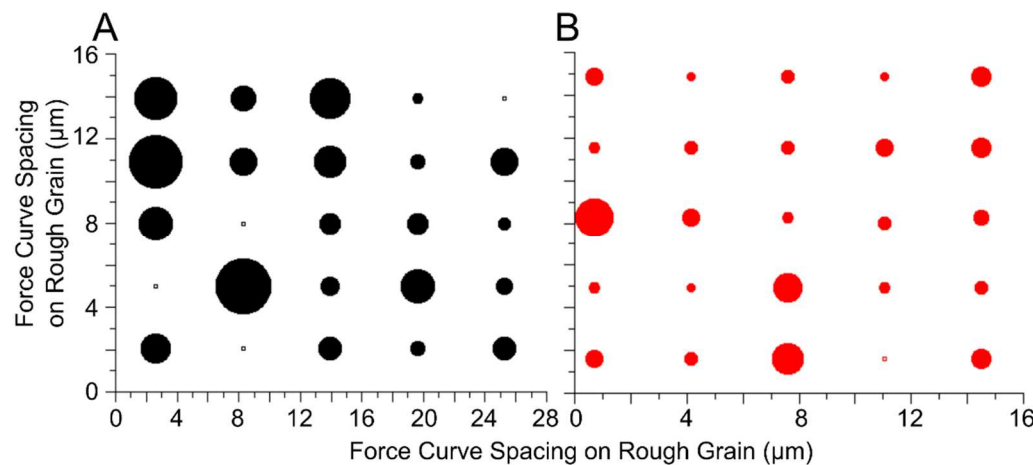


**Figure 49 Grid plots show the results of experiment RoughC-2 for the formation liquid (black circles in “A”) and low salinity brine (red circles in “B”) with adhesion ranging from 0 nN (empty circle) to 2.5 nN (largest circle).**

Next, we performed an additional analysis on the adhesion results to determine why the greatest adhesion occurred in the first data set of each experiment. We suspected that this result was due to the probes changing over time after repeated interactions

with the surface features. To test this, we plotted the individual force curve results in the order that they were collected.

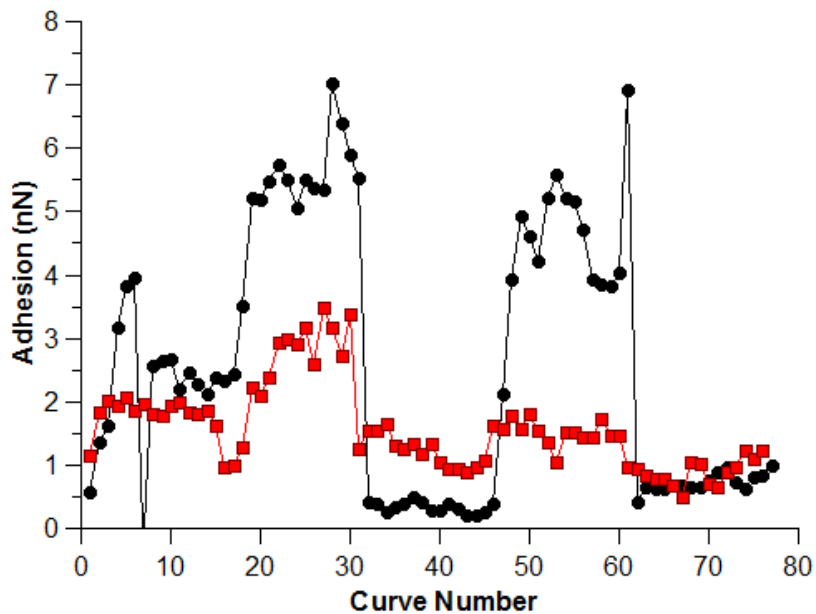


**Figure 50** Adhesion for each force spectroscopy curve of experiment RoughC-1 between the dry oil-coated probe and an “A” grain. The black circles indicate formation liquid data and the red squares indicate low salinity brine data.

As shown in Figure 50, RoughC-1 exhibits very different results at each of the five locations, which can be observed as regions of alternating higher and lower adhesion. Also, there is a decreasing linear slope to the low salinity liquid data, which suggests that the probe is changing throughout the experiment, perhaps by picking up clay platelets. The formation liquid results exhibit such a large standard deviation in the data that we did not perform any additional analysis to compare the amount of slope between the salinities.

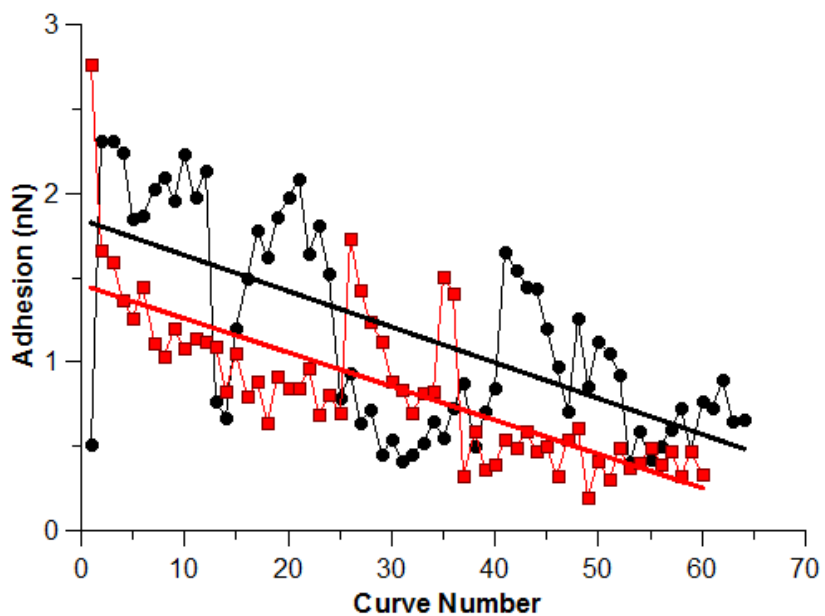


**Figure 51** Adhesion for each force spectroscopy curve of RoughC-2 between the dry oil-coated probe and an “A” grain. The black circles indicate formation liquid data and the red squares indicate low salinity brine data. Linear fits in corresponding colors have been applied to show the gradually decreasing adhesion over the course of the experiment.

Similarly, experiment RoughC-2 also showed a decreasing adhesion as the liquid cell experiment progressed (Figure 51). RoughC-2 exhibited a smaller standard deviation than RoughC-1. Trying to draw salinity dependent comparisons by removing the tilt from these data sets is useless because we are unable to determine if the resulting vertical offset is due to truly greater adhesion in the formation liquid or if it is a function of the changing probe surface over time. To confirm that gradually decreasing adhesion did not occur in all experiments, we also tested the slope on mica in two experiments and found slope values that were an order of magnitude smaller and sometimes positive, indicating that the probes produce more consistent results on a mica substrate.

If the negative slopes observed in RoughC-1 and RoughC-2 were due to the probe picking up particles or losing oil and becoming less sticky throughout the measurements, then drying the probes for longer might produce a harder, less sticky surface that would yield more consistent results. In addition, reversing the order in which we used the solution liquids could indicate if there truly is a salinity dependence. To test these theories, we started by analyzing the results from RoughC-3 and RoughC-4, in which the experiments were performed with the solution molarity orders reversed. Additionally, in experiments RoughC-3 and RoughC-4, the results were collected in 10 by 10 grids.

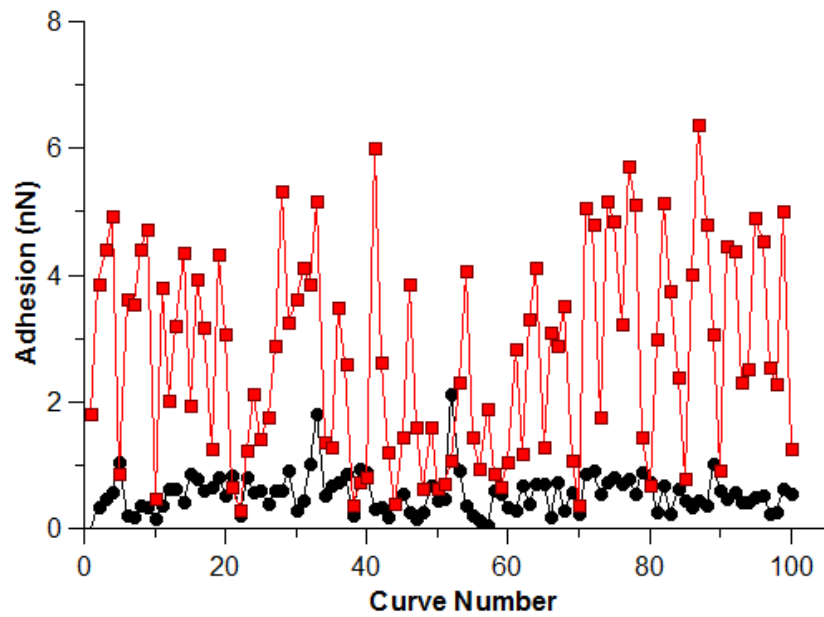


**Figure 52 Individual adhesion measurements in two solution molarities for the dried “A” oil coated probe on mineral grain (experiment RoughC-3). The black circles indicate formation liquid data and the red squares indicate low salinity brine data.**

In RoughC-3, there was greater adhesion for the low salinity brine with no negative slope for either salinity (Figure 52). We know that the difference in these results is not

a function of random surface topography because we kept the sample immobile during brine exchange, thereby collecting results for both brines on the same grid points. We also analyzed the RoughC-4 results (Figure 53), which were collected on the same mineral grain as RoughC-3 (Figure 52). By applying linear fits to the adhesion vs. curve progression data, we observed a slight downward slope for the first low salinity (red) and a nearly zero slope for the remaining two data sets (black, blue). Therefore, both RoughC-3 and RoughC-4 showed greater average adhesion in the first low salinity brine than in the formation liquid.

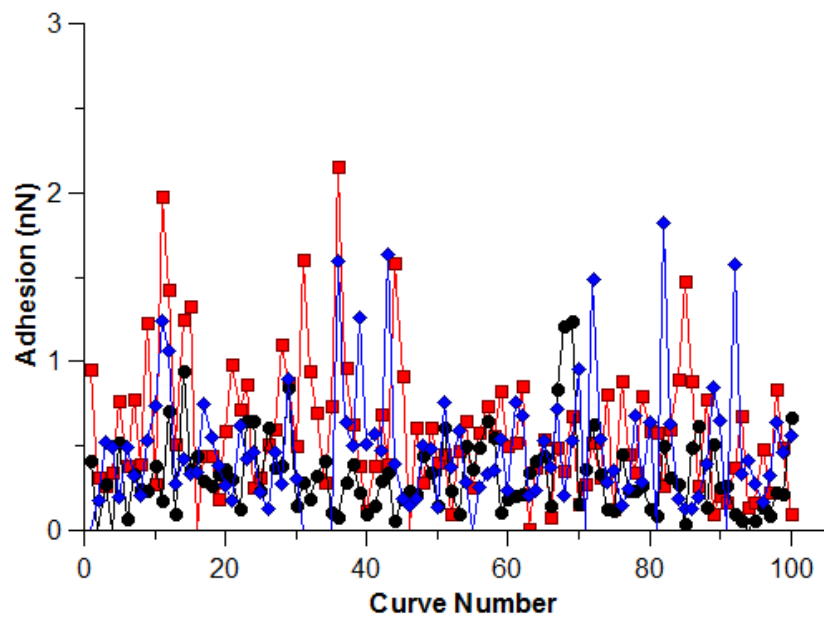


**Figure 53 Individual adhesion measurement for two solution molarities using a dried “A” oil coated probe on a mineral grain (experiment RoughC-4).** The black circles indicate formation liquid data, the red squares indicate low salinity brine data, and the blue diamonds indicate a repeated experiment using the low salinity brine data. The total experiment was performed in the order low salinity brine, formation liquid, repeated low salinity brine.

In RoughC-4, where another set of low salinity data was collected after the formation liquid data, the distinction is not as clear (Figure 48 and Figure 53). Therefore, we sought other methods besides average and standard deviation to determine if there was a difference in the formation liquid and second set of low salinity data for RoughC-4. We compared the results in Q-Q plots, which provide a more systematic way to compare distributions in a histogram (Figure 54 and Figure 55). To construct the Q-Q plots, we sorted the adhesion results in ascending order along each axis: the sorted adhesion values for the first low salinity data set are shown on the  $x$ -axis, and the sorted adhesion values for the third low salinity data set are shown on the  $y$ -axis. Each measurement is therefore considered to be a quantile. In this setup, two data with a similar histogram shape will produce a linear plot with a slope of one. For our data, we observed that both low salinity data sets have a similar shape, as the slope of their Q-Q plot data is 0.9 (Figure 54). In contrast, when we compared the low salinity data sets to the formation liquid, the slope is approximately 0.6 instead (Figure 55).

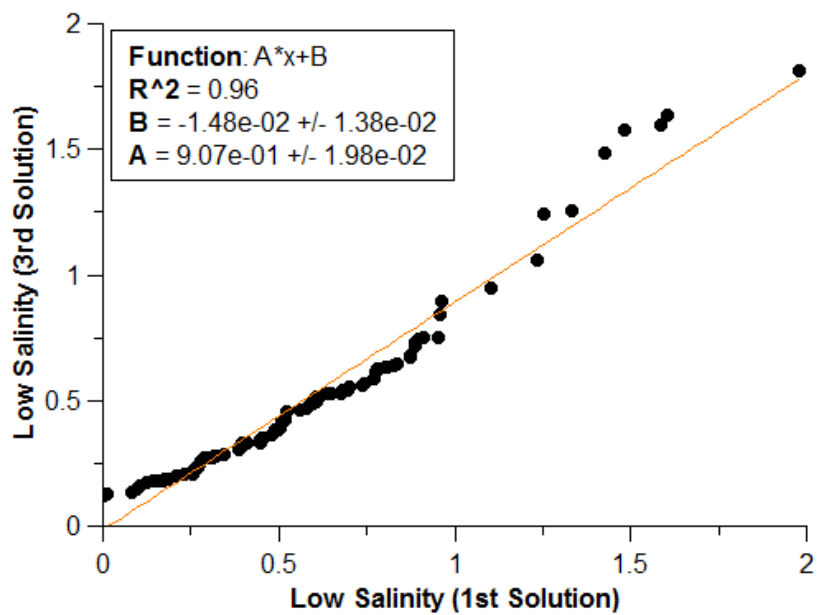


Figure 54 Q-Q plot of the first and second data sets collected in low salinity brine in experiment RoughC-4.

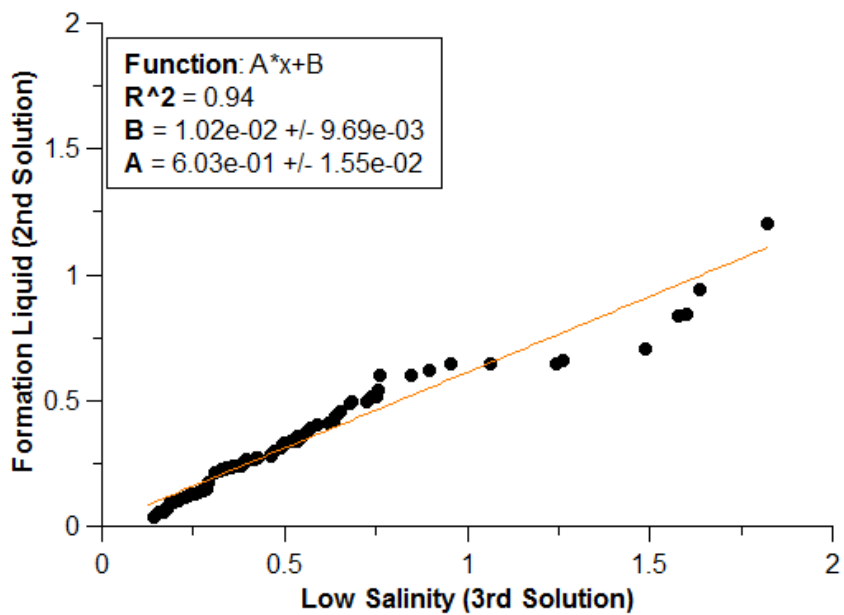
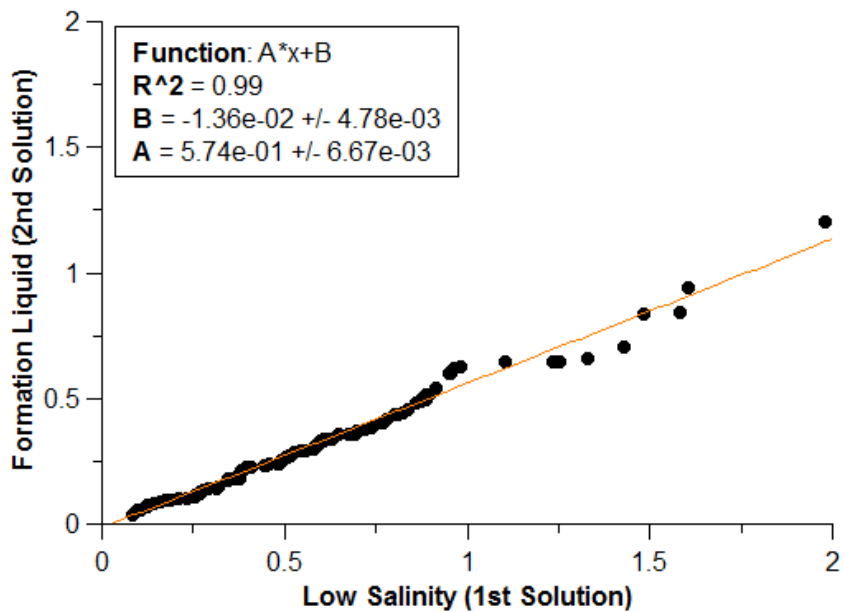


Figure 55 Q-Q plots comparing each low salinity brine data set to the formation liquid data set in experiment RoughC-4.

These results suggest that both sets of low salinity brine data are similar to each other and distinct from the formation liquid (in RoughC-4). When compared to their average adhesion values, we conclude that the low salinity brine results trend towards exhibiting greater adhesion than the formation liquid.

In summary, our results show greater adhesion for the formation liquid than the low salinity brine in two experiments (RoughC-1 and RoughC-2) and the reverse trend in two other experiments (RoughC-3 and RoughC-4). To determine potential causes of these differences, we compared the experimental conditions more closely. RoughC-3 and RoughC-4 were performed on the same mineral grain, while RoughC-1 and RoughC-2 were each performed on separate grains. This means that differences in topography or surface chemistry could have affected the adhesion results. Additionally, the probes in RoughC-3 and RoughC-4 were dried for longer periods of time than those in RoughC-1 and RoughC-2, as we used the cantilever's resonance in RoughC-3 and RoughC-4 to determine the oil's readiness. This suggests that the probes in RoughC-1 and RoughC-2 may have had softer, stickier oil layers that were more likely to change over the course of the experiments. Also, the data for RoughC-1 and RoughC-2 was collected in only four or five locations with 20 curves per location, while the RoughC-3 and RoughC-4 data was collected on a 10 by 10 grid of 100 locations with one curve per location. This difference could have also led to differences in the results due to the heterogeneity of the surface texture.

Relating these results to their corresponding approach curves provides a clearer picture of the interactions. In all four experiments, we saw more instances of repulsion in the

approach curves for low salinity brine than for the formation liquid, suggesting that the long range forces are similar despite any differences in mineral grain or oil layer dryness. In contrast, we observed variation in adhesion: gradual changes in the adhesion of two experiments (RoughC-1 and RoughC-2) and consistent results for the other two (RoughC-3 and RoughC-4).

If the probes in RoughC-1 and RoughC-2 were picking up clay platelets throughout the experiments, we would probably see similar results: a gradually reduced adhesion as the probe became progressively coated in clay and increasing repulsion as the clay particles on the probe repelled the clay particles on the substrate. However, these trends would also occur if the probes were gradually losing part of their oil coatings throughout the experiments: gradually decreasing adhesion from a reduced oil coating, but similar repulsion because even a thin layer of oil would retain the polar components necessary to make a charged, repulsive surface.

Overall, our results indicate more instances of repulsion in low salinity brine compared to formation liquid for the “A” reservoir by exhibiting reproducible approach curve data on multiple mineral grains with multiple dried “A” oil probes. In contrast, it is difficult to draw a firm conclusion on salinity dependent adhesion in an oil reservoir based on our preliminary results. However, these experiments highlight multiple experimental limits for adhesion measurements in this system. When testing such a rough surface with force spectroscopy, performing measurements in a grid pattern should provide a more accurate representation of the interacting forces. Additionally, using a resonance method to determine when the oil layer on the probe is dry is a more

robust way to prepare the tips that likely contributed to the more reproducible adhesion results we observed in RoughC-3 and RoughC-4.

## **d. Discussion**

### **d.1. Wet vs. Dried Oil Probes**

To test the differences between wet and dried oil coated probes, we performed experiments with “A” oil, complex salt brines, and mica. For both types of probes, we saw very few instances of repulsion due to the high salinity of the brines, so we used retract curves for comparison. For the wet oil, there was no consistent trend and two of the probes exhibited gradually decreasing adhesion over the course of the experiment (Figure 35), suggesting that the oil layer was gradually pulling off the surface. For the dried oil, two probes exhibited greater adhesion in the low salinity brine and the third probe showed no difference (Figure 40). The dried oil probes were relatively stable as evidenced by the standard deviation values that are small enough to clearly indicate a salinity dependent adhesion in Figure 40. Additionally, in the one experiment where we collected curves in a grid on mica, we saw similar interactions at each grid location (Figure 41). The dried oil probes also showed consistent, salinity dependent electrostatic repulsion between the probe and the mica substrate (Figure 36), indicating that the drying process retains the charged nature of the oil and allowing us to study the salinity-dependent features of its charged surface as it interacts with a mineral.

## d.2. Oil Comparison

To test how different crude oils might lead to different oil extraction results as a function of injection liquid composition, we performed comparison experiments between the three crude oils. Since the experiments were all conducted with 1 mM and 10 mM NaCl brines, the Debye lengths were large enough for us to clearly identify electrostatic repulsion in the approach curves (Figure 36). Therefore, we focused our comparison on the approach curve results and found interesting oil-dependent variations (summarized in Figure 56 and detailed in Figure 36, Figure 37, Figure 38, and Figure 39).

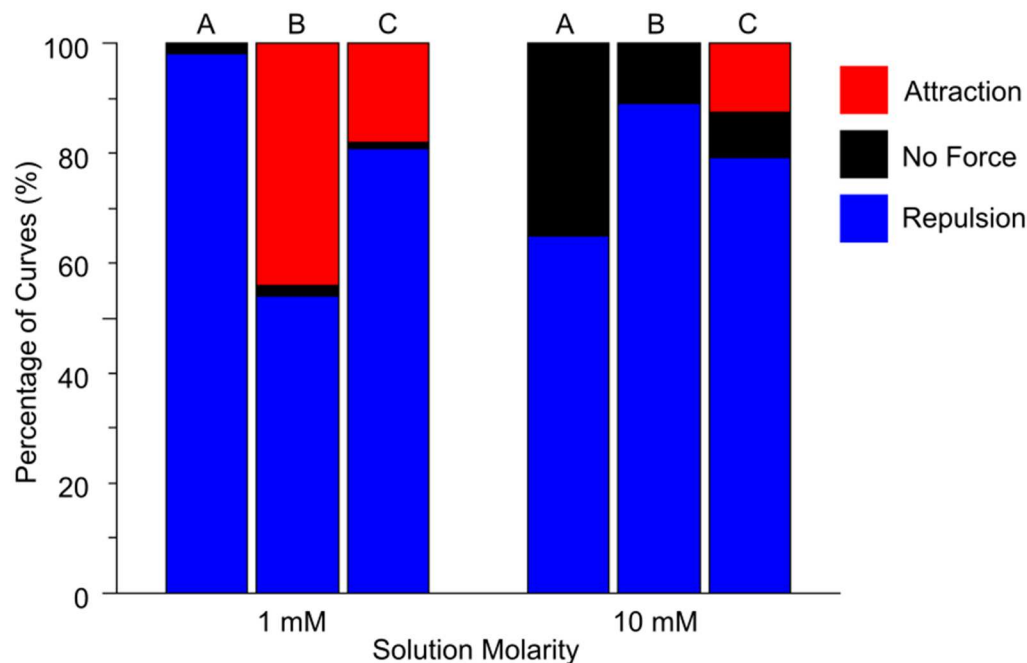


**Figure 56** Percentage of approach curves from each of three crude oil varieties that exhibited long range Repulsion (blue) or Attraction (red) in dried oil coated probe experiments. Curves in which the electrostatic force was too weak to detect are indicated by “No Force” (black). The “A”, “B”, and “C” crude oils are indicated by labeled columns. The experiments were performed in 1 mM and 10 mM NaCl solutions.

For the dried “A” oil, we observed electrostatic repulsion in both salinities (Figure 56), with greater repulsion in the lower salinity brine (Figure 36). For the “B” oil (Figure 37), we observed electrostatic repulsion in the 10 mM NaCl results (Figure 56), while the 1 mM NaCl results showed both repulsion and attraction (Figure 56). For the “C” oil, we observed both attraction and repulsion without a clear dependence on solution molarity (Figure 38, Figure 39, and Figure 56).

Only the difference in oils can explain these varying results. The dissimilarity in the results is not an obvious function of the drying technique, because for each oil, we dried some probes using optical observation of the interference patterns and some probes using resonance testing. The results are not an obvious function of the age of the oil samples because the experiments were conducted over a period of years and there was no chronological trend to indicate that the oil behaved differently as it aged. Additionally, the same type of mica was used across all experiments.

These differences give us information regarding the characteristics of the different oils and their behavior in the tested aqueous environments, but determining the true nature of these changes is impossible because prior handling and chemical composition of the oil samples is proprietary. However, based on the types of variations that we have observed, we can speculate on possible causes. Two important questions that stem from the “B” oil results include: (1) how can the 1 mM NaCl solution yield repulsive and attractive curves and (2) why does the 10 mM NaCl solution only yield repulsive curves? For the “C” oil results, the most important question involves how some probes

can exhibit attraction and others exhibit repulsion with no clear dependence on a particular aqueous solution.

The most likely explanation for the trends exhibited by both of these oils is that there are multiple interconnected variables. We assume that the three oils have different compositions. Additionally, by dipping the probes in different quantities of oil and drying them for different drying times, each probe may contain a different composition of molecular components from the oil on its surface. These differences may result in varied isoelectric points, surface charge distributions, or unique chemical interactions between the oil surface and salts in the aqueous solutions.

Long-range repulsion and attraction indicate the presence of electrostatic forces, but because the isoelectric point of mica is approximately pH 3,<sup>104</sup> we expect its surface charge to remain negative in the approximately pH 5–6 pH range of these solutions. Additionally, the quantity of oil on each probe was orders of magnitude smaller than the liquid cell solution. Therefore there is no evidence to suggest that the crude oil modified the solution pH. This means that the surface charges of the “B” and “C” oils must be changing during the experiment. Since the isoelectric point of most crude oils is between pH 3 and pH 7,<sup>84,105–107</sup> which includes the pH range of our aqueous solutions, this gives further evidence that the varying isoelectric point could be contributing to the curve changes. Additionally, asphaltenes, a polar molecular component of crude oils, have been documented to have isoelectric points between pH 2 and pH 4 in the same range of NaCl solutions that we used.<sup>108</sup> Therefore, if some

probes exhibited a greater concentration of asphaltenes on their surfaces than others, this might explain the differences between probes that we see for the same oil.

Although charge reversal of a surface, due to ion concentration of the aqueous solution rather than pH change, is more often encountered with multivalent ions,<sup>64,109</sup> it can also occur in monovalent solutions.<sup>110,111</sup> Some researchers speculate that charge reversal can occur when ions bond so firmly that they effectively change the surface charge.<sup>112</sup> Others indicate that charge reversal could be due to changing the surface charge density.<sup>113</sup> We cannot disprove charge reversal as a contributing factor for the results of these particular oils, since we do not know their composition. However, other researchers who have studied the effect of 1 mM NaCl and 10 mM NaCl on crude oil and hydrocarbons indicate that there was no change in the isoelectric point for their samples.<sup>105,114</sup> In contrast, other researchers did see a shift in the isoelectric point of asphaltenes within the range of NaCl solution molarities that we studied.<sup>115</sup> This is relevant, since asphaltenes are one of the types of polar molecules that we expect to contribute to the charged surface of the dried oil coated probe.<sup>70,116,117</sup>

Another route of investigation involves determining if the zeta potentials of all crude oils respond to changing solution molarity in a way expected by double layer theory, i.e. a decrease in salinity should lead to a larger force via less screening and a more negative or positive zeta potential for a negatively or positively charged surface, respectively. In NaCl solutions, some researchers have found these expected trends to be true for crude oils,<sup>85,105,118–120</sup> coal tar creosote,<sup>121</sup> and bitumen.<sup>122</sup> In contrast, other researchers<sup>123</sup> have shown that asphaltenes exhibit a nonlinear dependence of zeta

potential on solution molarity. Their tests were performed in aqueous solutions of neutral pH of varying NaCl compositions between 0.1 mM and 100 mM. Although the tests showed a negative zeta potential for all the molarities, the most negative zeta potential value occurred for the 1 mM solution, leading to a “U” shaped trend in which the higher and lower salinities all exhibited less negative, i.e. closer to zero, zeta potentials.<sup>123</sup> This result is not unique, as other researchers have also showed that asphaltenes exhibited a nonlinear dependence of magnitude of the zeta potential on solution salinity for the same range of NaCl solutions.<sup>115</sup>

Beyond the previously listed theories, there could also be unexpected ion<sup>124–126</sup> or chemical interactions occurring between the NaCl solution and oil component molecules<sup>127</sup> on our probes. For example, some researchers have shown experimentally that in a 1 mM NaCl solution hydroxyl ions can lead to a negative surface charge on a nonpolar oil.<sup>128</sup> Additionally, the distribution of surface charges on the substrates or probes might lead to areas of differing surface forces.<sup>129</sup> A combination of these different effects seems the most likely cause of the differences we observe between the oils. However, the complete reason remains unknown. Regardless, of the exact cause of these differences, the fact that our dried oil coated probes can distinguish them strongly indicates that these probes would be very useful in oil recovery prediction.

### d.3. Probe Use on Mica vs. Mineral Grain

We also compared the force interactions between a single oil (“A” oil) and several different substrates, e.g. mica and a variety of rough mineral grains, to determine the effect of the mineral substrate on oil recovery. In the approach curves, we saw very few

instances of repulsion on mica, but for the rough mineral grain, we saw some instances of repulsion, especially for the 28 mM low salinity brine (Figure 46). The more common occurrence of repulsion on mineral grains may have been due to a greater charge on the mineral grain surfaces, or it could have resulted from a greater contact area, e.g. if the probe was landing in depressions or valleys on the grains where it experienced a greater contact area compared to a planar surface.

When we tested for salinity-dependent adhesion between various substrates by interpreting retract curves, our results ran contrary to expectations. We saw greater adhesion for the low salinity brine than the formation liquid in two of three experiments on mica (Figure 40), while the only two reliable rough mineral results also displayed greater adhesion for the low salinity brine (Figure 48). We considered the other two rough mineral grain experiments unreliable because the adhesion gradually decreased throughout the testing. These similar adhesion results on both the mica and mineral grain are interesting because they are contrary to what we might expect. If electrostatic forces were much stronger than van der Waals attraction, we would expect a reduction in repulsion via the higher-molarity formation liquid. This would allow van der Waals attraction to become dominant, leading to an overall increase in the magnitude of the adhesion observed in retract curves. Instead, we saw greater adhesion in the low salinity brine for both substrates.

Since we have a limited number of results, these experiments would need to be repeated to fully confirm the observed trends occurring for this particular “A” reservoir and its components, i.e. oil, mineral, brines. However, our current results show that it is

possible to detect long range repulsion between the oil coated probe and mineral substrate in particular aqueous environments. These experiments exhibit some interesting, unexpected, and reproducible trends that should be beneficial in furthering the understanding of salinity dependent interactions in a petroleum reservoir.

### e. Conclusions

In our efforts to aid in the development of custom injection liquids for higher oil recovery yields, we successfully developed oil-coated atomic force microscopy probes to detect the force interactions between an oil droplet and a mineral surface in an aqueous environment. We demonstrated that a dried oil probe is superior to a wet oil-coated probe, since the oil layer on a dry probe was shown to be less likely to pull off the probe during force measurements. This development provides a more stable oil layer for detecting probe-to-substrate contact in approach curves, making quantitative electrostatic measurements possible. We also demonstrated that, for our “A” oil probes in simple salt brines, the dried oil probe retained the polar components and corresponding surface charge of the wet oil probe. We then showed salinity-dependent repulsion with the dried oil probe that was consistent with trends expected by electric double layer theory. Furthermore, using these dried oil coated probes, we also showed variations in forces as a function of crude oil type, which is expected since different reservoirs respond differently to the same injection liquids. These results, which were conducted on mica for consistency, were reproducible over multiple probes.

In later tests, we explored the effects of a rough mineral grain surface using oil from the “A” reservoir. Approach curve results exhibited more instances of repulsion for the

low salinity brine than the formation liquid, suggesting that a low salinity injection liquid might be beneficial to oil recovery by repelling unattached crude oil from the mineral surfaces. Retract curve results were split. Two probes showed gradually decreasing adhesion throughout the entire experiment, so we were unable to determine a salinity dependence. However, the two probes that were dried for a longer time and presumably had more stable coatings both showed greater adhesion in the low salinity brine. This trend is unexpected but interesting, since it indicates that using low salinity brine in the “A” reservoir would have mixed results, causing free-floating oil to be repelled from mineral surfaces but allowing attached oil to remain firmly adhered to the surface. However, since only a few tests were conducted on mineral grain samples, more experiments are needed to provide a more conclusive result. Overall, we have developed a tool to test oil recovery techniques, proven its reproducibility on mica substrates, and provided promising preliminary results on native mineral samples.

## **Chapter 4: Graphene Oxide Functionalized Probe**

### **a. Development**

#### **a.1. Overview**

The strength of GO combined with the low density and versatility of polymers has driven research in GO-polymer nanocomposites for many years.<sup>130,131</sup> Further advances to utilize these materials to their full potential requires an increased understanding of the interactions between the GO flake and polymer matrix. For example, by choosing GO-polymer combinations with the greatest interfacial attraction, the bond between matrix and filler can be maximized, allowing the positive attributes of both materials to be combined.

Previous work in our lab<sup>132</sup> has shown a qualitative difference in the GO-polymer interaction for various polymers by using a peeling test, in which GO is sandwiched between two flat materials. When the materials are peeled apart, the GO will preferentially adhere to the material with which it has the greatest bond. Performing a series of these experiments with different materials provides a ranking of which GO–material combinations exhibit the greatest interfacial attraction. To compliment and further enhance this test, we conducted force spectroscopy on polymer surfaces using a novel probe coated in GO flakes, allowing us to measure the interfacial forces between GO and the polymer as a function of separation distance. In the process of developing this probe, we tested its effectiveness, identified its limitations, performed force measurements on various polymers, and compared the results. While the previous

peeling test studies focused only on poly(methyl methacrylate) (PMMA) and polyvinyl alcohol (PVA), our current work investigated two additional polymers: acrylic and polyimide (PI). By comparing the results of the peeling test to the GO probe test, we confirmed the probe's effectiveness and developed a more comprehensive understanding of the forces present in the internal structure of several potential GO-polymer nanocomposites.

## **a.2. Manufacturing and Characterization**

### **a.2.1. Probe Design**

We manufactured the probes as detailed in the Experimental Methods: in short, we used quick set epoxy to attach silica microspheres to tipless dynamic mode cantilevers (nominal spring constant: 40 N/m). The high stiffness of the dynamic mode cantilevers was chosen to allow for the measurement of the substantial van der Waals forces that attract a multi-micron diameter colloidal probe to a substrate in air. With a softer cantilever, the piezoelectric device would not be able to retract far enough to overcome the adhesion between the probe and substrate. Even in cases where the adhesion was not quite this strong, the deflection of the laser along the photodiode was still great enough to be outside the linear response region of the detector, underrepresenting the force measurements.

After manufacturing the silica colloidal probes, our first challenge involved attaching the GO to the probe surface. GO and silica have similar isoelectric points, approximately pH 3.5 and pH 2, respectively.<sup>133,121</sup> Therefore, both the GO flakes and

the silica sphere are expected to have a negative surface charge in an aqueous GO dispersion. The resulting electrostatic repulsion effectively prevents the GO flakes from coming close enough to the silica to experience van der Waals attraction. Metwalli et al.<sup>134</sup> described a functionalizing agent, (3-trimethoxysilylpropyl) diethylenetriamine, which we used to apply a positive charge to the silica surface when it was dipped into the GO-water dispersion. The resulting positive charge on the functionalized silica caused the negatively charged GO to be electrostatically attracted to the probe, coating it in GO.

Due to its caustic nature and hydroscopic properties, we were careful to use the amine in a fume hood and store the bottle in a vacuum desiccator. To functionalize the probes, we started by combining 1.98 g Millipore water with 20 µl of the amine. We then applied 10 µl of the diluted mixture to a cover slide on the Olympus inverted microscope. Using our translation stage and custom tip holder, we submerged the bare silica sphere probe into the droplet so only the end of the cantilever was in the liquid for 30–38 minutes, lowering the probe as necessary to keep it submerged as the droplet evaporated. After coating the probe in amine, we placed the probe in a 110 °C oven for 15 minutes. Afterwards, we removed the probe from the oven and dipped it in a droplet of GO dispersion for 30 minutes. To remove residual water, we placed the tip in a vacuum desiccator for at least an hour and then stored probes in AFM probe boxes until use.

### **a.2.2. Surface Topography: Effect of Rinsing**

After functionalizing our silica probe and immersing it in the aqueous GO solution, we needed to confirm that the GO was coating the surface of the probe. We first scanned a calibration grating containing vertically oriented sharp probes in order to visualize the surface of the probe in question (Figure 57A).<sup>135</sup> Both the bare silica probes and amine coated probes exhibited bumpy textured surfaces (Figure 57A, B). However, the topography of the GO-coated probes varied. In some cases, the surface acquired a wavy, wrinkled appearance after the GO was added (Figure 57C). However, in other cases there was no obvious difference in topography even after using the same procedure. Therefore, we assume that the visual differences are a function of the thickness of the layer of GO coating the probe surface.

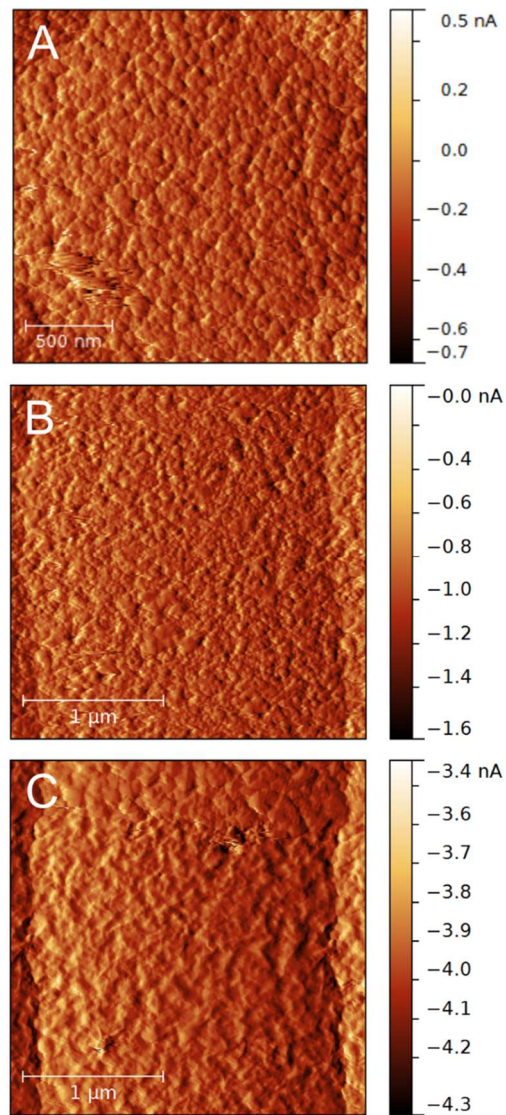


**Figure 57** AFM DFL images of the surface of a bare colloidal silica probe (A), the same probe coated in amine (B), and coated in GO flakes (C). These scans indicate that the topography of the probe surface is not noticeably changed by adding the amine layer.

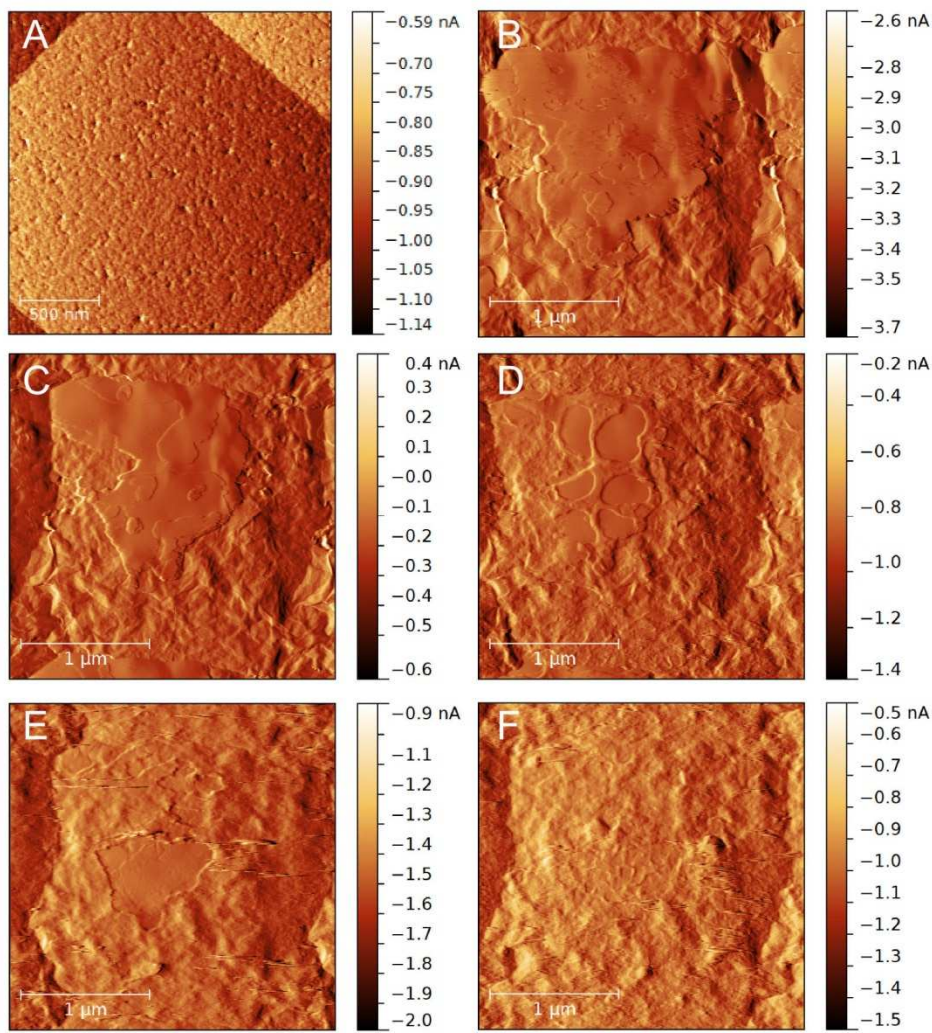


**Figure 58 DFL images from contact mode of a bare silica probe (A), the same probe after being coated in GO (B) and each subsequent rinsing to remove loosely bound GO (C-F).**

Another probe developed a thick, many-layered coating of GO with a stepped plateau area and a wavy background appearance (Figure 58B). To remove this large collection of flakes, we dipped the probe in a droplet of Millipore water for 10 minutes, dried it in the vacuum desiccator and scanned it again (Figure 58C). By alternating rinsing for 30 minutes each and scanning (Figure 58C through Figure 58F), we were able to

gradually see the thick, multi-layered collection of flakes pull away and the wrinkled surface remain. This rinsing technique shows that the amine-GO bond was stronger than the GO-GO bond, allowing the GO closest to the amine coated surface to remain attached to the probe as more loosely connected GO layers were removed.

### a.2.3. Surface Topography: Effect of Peeling

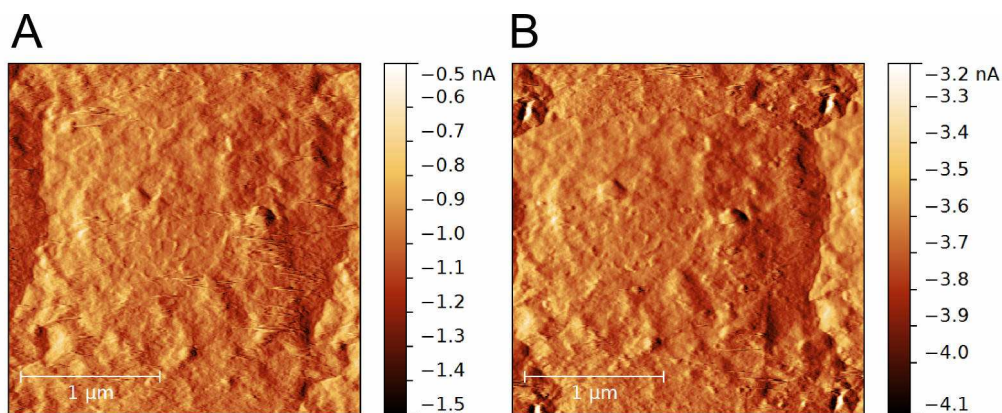


**Figure 59 Probe before (A) and after (B) force spectroscopy experiments on PDMS. The surface features remain unchanged.**

Since we were able to rinse off excess layers of GO with one sample probe, we sought to test the stability of the GO-amine layer during force spectroscopy experiments. Essentially, we wanted to determine if we could peel the GO off the probe surface. To test the adhesion of the GO-amine layer, we brought the GO probe into contact with the relatively deformable surface of polydimethylsiloxane (PDMS) (Sylgard 184 Silicone Elastomer, Dow Corning). Bringing a relatively stiff substrate into contact with a deformable surface causes the deformable surface to act similarly to adhesive tape: the contact area increases as the deformable substrate conforms to the other surface within the range of van der Waals attraction, leading to a strong bond between

the surfaces. In our case, the adhesion between the PDMS surface and our probe was so great that we had to manually retract the probe past the remaining 5  $\mu\text{m}$   $z$ -range of the piezoelectric device to remove it from the surface. Afterwards, we scanned the sharp-tipped calibration grating again and found that the probe surface looked very similar before and after the force experiments (Figure 59), showing that despite contact with the deformable and adhesive PDMS surface, no clear changes to the surface of the GO coated probe resulted.

#### **a.2.4. Force Interactions: Effect of Probe Material**

Although scanning a calibration grating was an effective method for identifying a GO coating on some of our probes, the GO layers in other cases were too few to yield a visual difference in the AFM scans. For these cases, we sought a more rigorous technique to conclusively show that using our coating procedure would produce a GO coated probe every time. To do so, we performed separate force spectroscopy measurements with the same probe with a bare silica sphere, an amine coating, and a GO coating. Changing interactions between the same substrate and probe provided evidence that the probe acquired new coatings of amine and GO throughout the experiments.

For this set of experiments, we used silanized mica as a substrate because (a) its flatness was expected to yield the most reproducible results, and (b) its nonpolar surface conferred via functionalization was not expected to accumulate layers of adsorbed

water from the environmental humidity, which would lead to increased adhesion due to capillary forces.

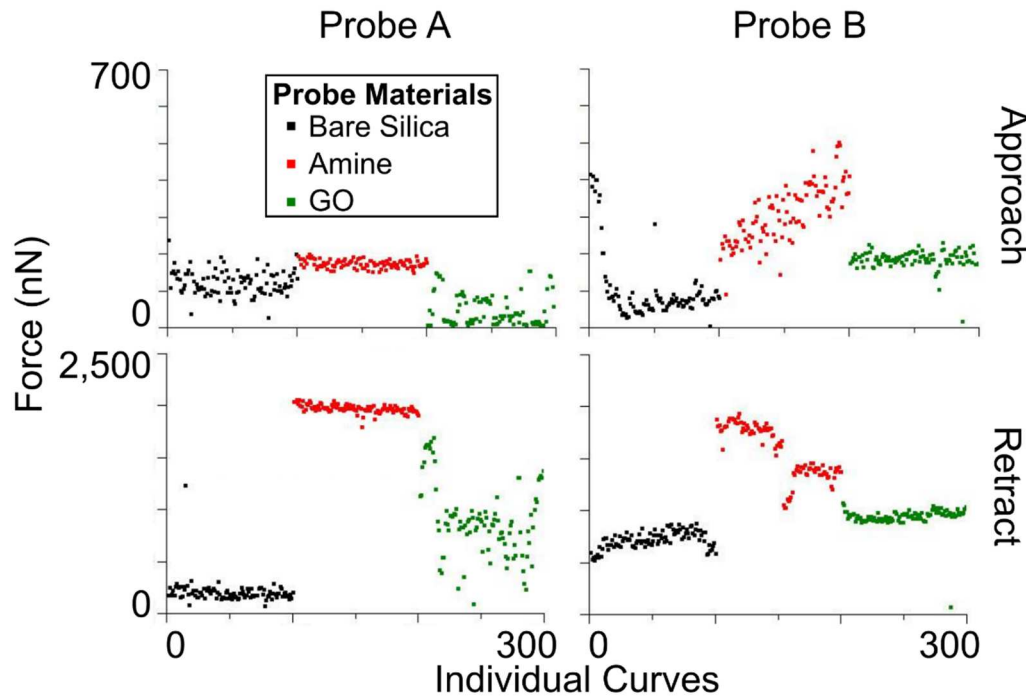


**Figure 60 Force spectroscopy results of the snap-down (Approach) and pull-off (Retract) force for three probe surfaces (bare silica, amine coated and GO coated) on silanized mica. The Approach and Retract curve results are arranged in designated rows and the results from two different probes (A, B) are arranged in columns. In all cases, the y-axis indicates force (nN) and the x-axis indicates the individual force curve measurements.**

We performed force spectroscopy using two probes (A, B), with 100 force curve measurements conducted for each probe material: bare silica, amine coated, and GO coated. Figure 60 shows the resulting snap-down and pull-off force for each curve. These results show a consistent change in the retract curve pull-off and approach curve snap-down due to probe coating. When the probe was coated in the amine, its attraction to the silanized mica increased in the approach and retract curves. Then, immersion in the GO dispersion caused the attraction to decrease to a similar value as the bare silica

probe. The exact reason for why a nonpolar silanized mica surface would experience greater attraction with the amine than the bare silica or GO coating is unknown. These measurements were collected in air, so the inherent differences of the positively charged amine and negatively charged silica and GO, in aqueous solutions, are not relevant to this particular situation. Additionally, these trends cannot be solely due to differences in surface roughness among the probe materials. For example, if the amine molecules were long enough to create a deformable layer on the surface of the probe, then we would expect to see greater adhesion in the retract curves for the amine due to increased contact area between the amine-coated probe and the silanized mica. However, this phenomenon would not explain the increased snap-down in the approach curve measurements. The difference may reside in the molecular structure of the materials, leading to a difference in van der Waals interactions. Such differences would affect both the approach and retract curve results in similar ways, i.e. greater van der Waals attraction would lead to both greater approach curve snap-down and retract curve pull-off values. Regardless of the mechanism that led to these trends, the trends themselves show conclusively that our procedure resulted in different probe coatings of amine and GO over the course of the experiment.

### **b. Force Spectroscopy Results**

Once a GO coating was confirmed on a probe, we conducted force spectroscopy measurements on multiple substrates. For each of three GO-coated probes, we performed 100 force curves on each substrate in the following order, as detailed in

Experimental Methods: silanized mica, HOPG, PS, LDPE, HDPE, mica, PVA, PEI, PMMA, and PI. One possible problem that can result from obtaining measurements on so many substrates is that the probe might become contaminated early in the experiment and influence the rest of the results. To minimize this risk, we performed measurements on the nonpolar substrates first, since the polar substrates are more likely to attract contaminants and water from the air. For all the substrates, it was necessary to place them in a humidified environment for a few days to reduce electrostatic surface charge, which was dominant on the new substrates. Without this step we found it very difficult to land the probe on the substrates and perform force measurements. Since this is seldom an issue with sharp tipped probes, we attribute this challenge to the unusually large size of the colloidal probe for use in air. Typically, colloidal probes are employed in liquid environments, where the forces are damped by the surrounding medium, so that their size will lead to forces that are large enough to detect in aqueous solutions. Additionally, the act of peeling the polymer off a substrate might lead to a charge buildup on the surfaces.

In order to compare results between probes, which possessed slightly different sphere diameters and spring constants, we devised a method for normalizing the data based on silanized mica force data. We chose silanized mica for this purpose because it is the flattest and most rigid nonpolar substrate of our experiments. The method involved normalizing the approach data from each GO probe by dividing each snap-down value by the average snap-down on silanized mica. Following normalization, we calculated the average snap-down value for all three probes on each substrate. We then repeated

the procedure for the retract curve pull-off measurements and plotted the resulting data from the approach and retract curves in Figure 61. Since silanized mica exhibits the smallest standard deviation of all the substrates, this confirms that it was an ideal choice on which to base the normalization procedure.

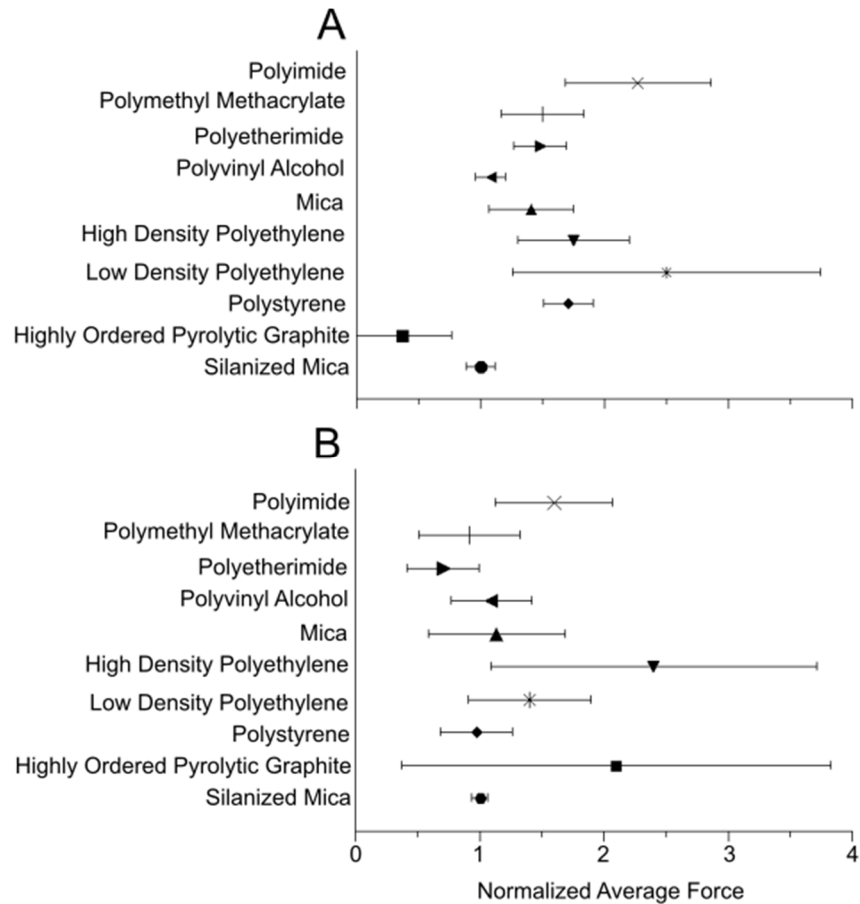


**Figure 61 Normalized and averaged approach snap-down (A) and retract pull-off (B) curve data for interactions between three GO probes and ten substrates. The error bars represent the standard deviations of the averages.**

We investigated both the approach (Figure 61A) and retract (Figure 61B) curve data to obtain a more complete picture of the interactions since each is influenced by different features. For example, pull-off values vary for deformable or rough samples due to greater variation in contact area, while the snap-down values may show very little

topography-induced variation because the surface's chemical composition, and resulting long range forces, remain the same. We observed this expected difference in our data. In most cases (HOPG, PS, HDPE, mica, PVA, PEI, PMMA) the standard deviation in the retract curve data was larger than the corresponding results in the approach data. HOPG and HDPE exhibited the greatest pull-off force and standard deviation of all the samples, which is likely because these were two of the roughest samples. HOPG showed localized flat areas with many rigid edges and steps, while HDPE exhibited many ribbed surface features (see Experimental Methods).

Although these substrates were all placed for the same amount of time in a humidified environment to reduce their electrostatic charge, it is possible that the charge was not reduced evenly on all substrates. One example of this might be LDPE, a nonpolar substrate that exhibited the greatest standard deviation in its approach curves. Because LDPE is nonpolar, the distribution of electrostatic charge on its surface may have remained uneven, leading to the variation of its snap-down forces. In contrast, its average pull-off force and standard deviation were lower, which might have occurred if the sample was discharging when the probe made contact with each localized area of the grid. After discharging, the resulting pull-off force would be a function of the van der Waals attraction rather than the electrostatic charge. This could lead to a lower force and smaller standard deviation.

The approach curve data revealed another anticipated trend: the smallest snap-down force occurred between the nonpolar HOPG and the polar GO probe. Similarly, the nonpolar silanized mica also exhibited less attraction than the other substrates. Among

the polar polymers, PI showed both the greatest snap-down and pull-off forces, indicating that it was relatively highly attracted to the GO. This is in contrast to PEI, PMMA, and mica, which all displayed similar snap-down results but more variation in their snap-off forces.

Of the two literature reviews addressing the enhanced mechanical properties of nanocomposites, there were few references to our particular GO-polymer combinations.<sup>130,131</sup> This is not surprising since polar GO nanoparticles are not expected to easily incorporate into any of the nonpolar polymers (PS, LDPE, HDPE) that we tested. However, we explored the interactions between these nonpolar substrates and our GO probe to provide a context for how the interactions in a polar-nonpolar material system would differ from a polar-polar material system. Additionally, since silanized mica, mica, and HOPG are not polymers, we would not expect to find references addressing them in GO nanocomposite research. We tested these materials to provide rigid surfaces with well-defined surface chemistries, i.e. model substrates. For these reasons, the literature reviews we found related to PVA, PEI, and PMMA. Furthermore, the high temperatures at which we cured PI reduce GO,<sup>136–140</sup> so polymer nanocomposites testing the interactions of unreduced GO-PI are uncommon. Multiple researchers have used thermal imidization techniques to cure the PI in GO-PI nanocomposites at a variety of temperatures. Some use the range of 210–250 °C,<sup>141–145</sup> while others used 300 °C and higher.<sup>146–153</sup> Some authors even explicitly state that the GO is being reduced within the nanocomposite due to this elevated temperature.<sup>154–159</sup> In one case, researchers used a lower temperature chemical

imidization process and documented the increase in mechanical properties for the GO-PI nanocomposite.<sup>160</sup> Due to the limited amount of research involving unreduced GO-PI nanocomposites, we chose this combination to further explore the interactions.

**Table 2 Summarized literature references of improvements in the mechanical properties of polymers due to the addition of GO flakes.**

Polymer	Filler Content	Improved Strength	Tensile Modulus	Young's Modulus
<b>PVA</b> <sup>131,161–163</sup>	0.7 wt% GO	76%	62%	
	3 wt% GO	70%	128%	
<b>PEI</b> <sup>164</sup>	3 wt% GO	_____	≈ 32% (storage modulus)	
<b>PMMA</b> <sup>131,165</sup>	1% w/w	decreased	decreased	
<b>PI</b> <sup>160</sup>	0.12 wt%	_____	25%	

Our assumption is that greater interfacial attraction/adhesion between a polymer and GO should lead to improved mechanical properties. In examination of the comparative interfacial strengths in peeling tests, Cai<sup>99</sup> demonstrated the following interfacial force ranking: GO-PVA > GO-PMMA > GO-PEI. Compared to the mechanical properties of GO-polymer nanocomposites listed in the literature (Table 2) Cai's results also show that the greatest GO-polymer interaction occurs for PVA. Her results are not as easy to directly compare for PEI and PMMA because the improved tensile strength value was not available for PEI. In contrast to the literature references, our approach curves indicate that the attraction between the GO-PVA is less than for the GO-PMMA and GO-PEI. The retract curve results suggest that there is slightly greater adhesion for the

GO-PVA than GO-PMMA and GO-PEI. In both the approach and retract results, the PEI and PMMA have similar responses. Since our probe can clearly distinguish different interaction forces as a function of GO-polymer combination, the discrepancy between our results (PVA, PMMA, PEI) and other published results suggests that some other experimental variable could have obscured the force differences among these particular substrates. Some experimental aspects that might have affected the results include the contact time, e.g. in a nanocomposite, the GO is in contact with the polymer prior to mechanical tests being performed. Also, since the polymer in a nanocomposite cures while in contact with the GO flake, the interactional forces involved in the curing process could depart from the surface forces probed here.

### c. Peeling Test Results and Discussion

To complement the findings of the GO probe test, we also conducted peeling tests on various polymer substrates. The peeling test essentially involves applying GO flakes in a single layer to a flat substrate via spin coating. Then, a layer of polymer is applied via drop casting or heat press and cured. Each set of conditions is dependent on the substrate and polymer employed. We worked with three principal substrates that all exhibited flat surfaces: mica, silanized mica, and silicon. For polar surfaces, we used mica and silicon with a 200 nm thermal oxide layer. Although silicon is not as flat as mica, it was necessary for some peeling tests because it did not cleave like mica when some polymers were peeled off. Mica silanized with (Tridecafluoro-1,1,2,2-Tetrahydrooctyl) Trichlorosilane (see Experimental Methods) provided a hydrophobic

surface. We typically use HOPG as a model hydrophobic surface, but we found that HOPG layers remained adhered to the polymer surface after peeling. Since mica cleaves in larger lateral sheets than the HOPG, it is easier to remove from the polymer in one piece.

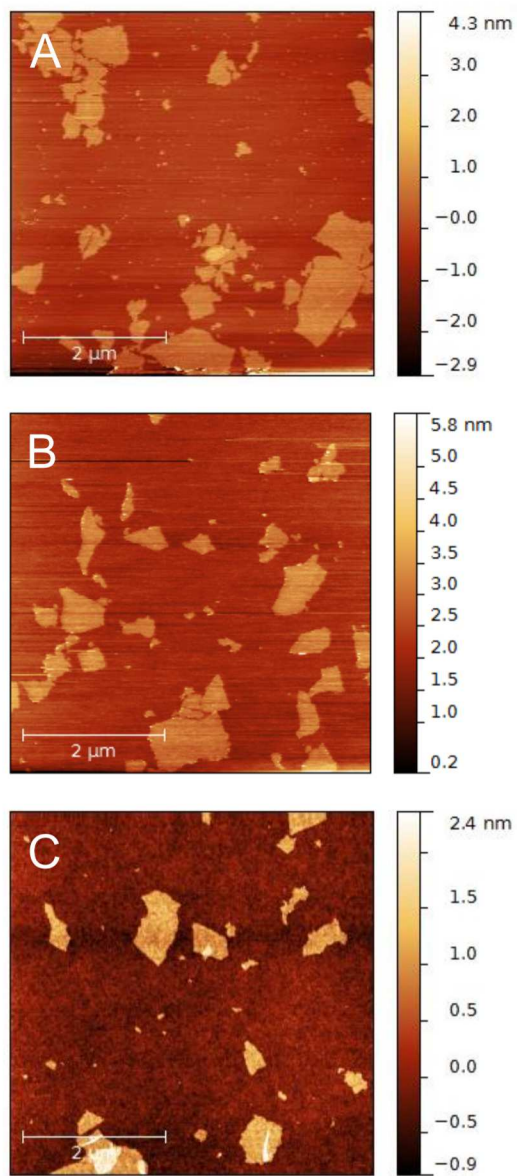


**Figure 62** These AFM topography scans show the distribution of GO flakes on mica (A), silanized mica (B), and silicon (C). In these scans, “B” uses GOi, while “A” and “C” use GOh.

GO was produced as described in Experimental Methods and spin-coated onto the desired substrate (Figure 62). Either an acrylic emulsion or PI was then applied to the GO-coated substrate. The acrylic was applied by drop casting onto the substrate, then

curing in ambient conditions for various amounts of time. Once cured, the acrylic was peeled from the substrate, and both the polymer surface and substrate surface were scanned. The acrylic side of the acrylic-substrate interface exhibited a bumpy surface texture (Figure 63) that remained consistent regardless of curing time. In contrast, the PI surface was smooth. After each peeling test, we scanned the substrate and polymer to identify if the GO flakes had been peeled off with the polymer or remained attached to the substrate.

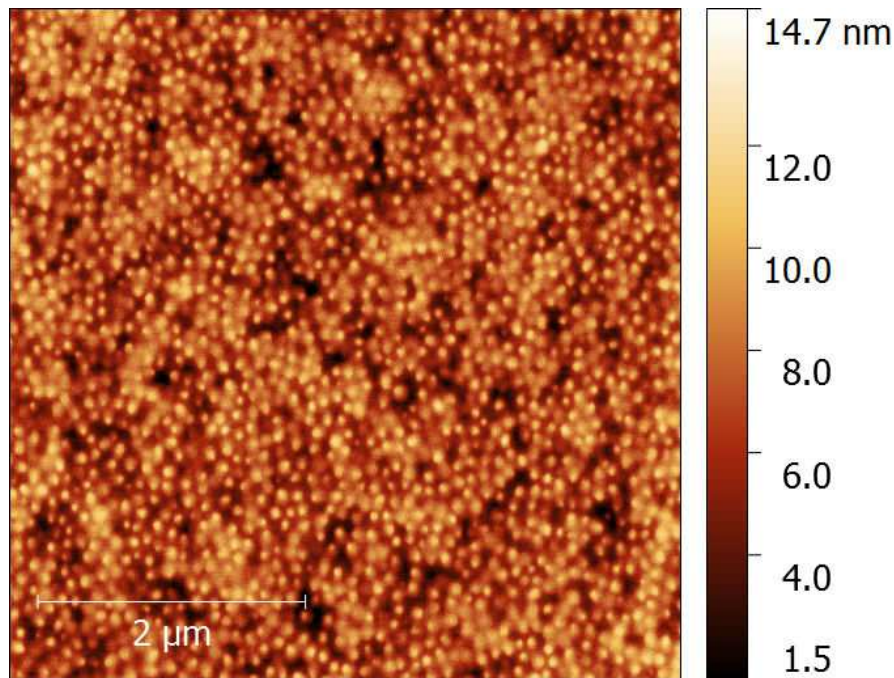


**Figure 63 AFM topography scan of the very bumpy surface of the acrylic polymer closest to a mica substrate after curing.**

To ensure that the acrylic and PI results could be compared, we needed to employ the same type of GO in both tests. The high temperature required to cure PI is also sufficiently high to yield reduced GO (rGO).<sup>137,139</sup> Since PI must be in contact with the GO during curing, all PI peeling tests were essentially performed with rGO. We

therefore needed to use rGO for the acrylic tests as well, so we heated the GO-coated substrate in an Ar environment in order to reduce the GO and prevent oxidation.

### c.1. Acrylic

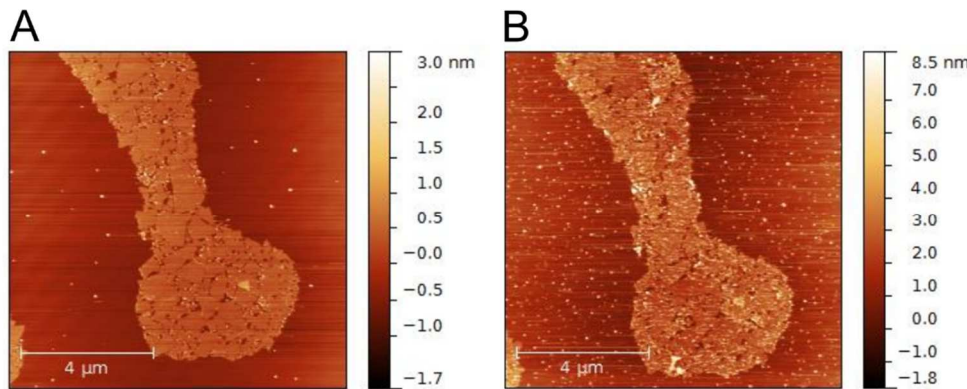


**Figure 64 GO on mica substrate before (A) and after (B) peeling. The exact same flakes are present in both AFM topography images with the addition of droplets of polymer residue.**

In peeling tests with the acrylic polymer, the flakes remained attached to the substrate after peeling for the following flake-substrate combinations: GO-mica (Figure 64), rGO-mica (Figure 65), and GO-silanized mica (Figure 66). Figure 64 shows a representative sample of this result, in which the same GO flakes were observed before and after peeling off the acrylic. One flake was lifted off the substrate in the GO-silanized mica case, implying that the GO-silanized mica forces may be slightly weaker than in the other cases (Figure 66). In all cases, acrylic residue also remained on the substrate after peeling. Figure 65A shows rGO on mica prior to acrylic application. After applying and peeling off the acrylic, polymer residue remained on the substrate (Figure 65B, C). This rGO sample exhibited a greater concentration of flakes on the

mica prior to peeling and more prevalent acrylic residue following peeling than did the GO sample (Figure 64). This suggests that the acrylic was attracted to the rGO. However, the exact reason is still unknown. Additionally, in all cases that exhibited acrylic residue on the substrate after peeling, we can assume that the bond between the acrylic and substrate was greater than the bond between the acrylic molecules. Otherwise, the acrylic molecules should not have separated from each other to leave a residue on the surface.

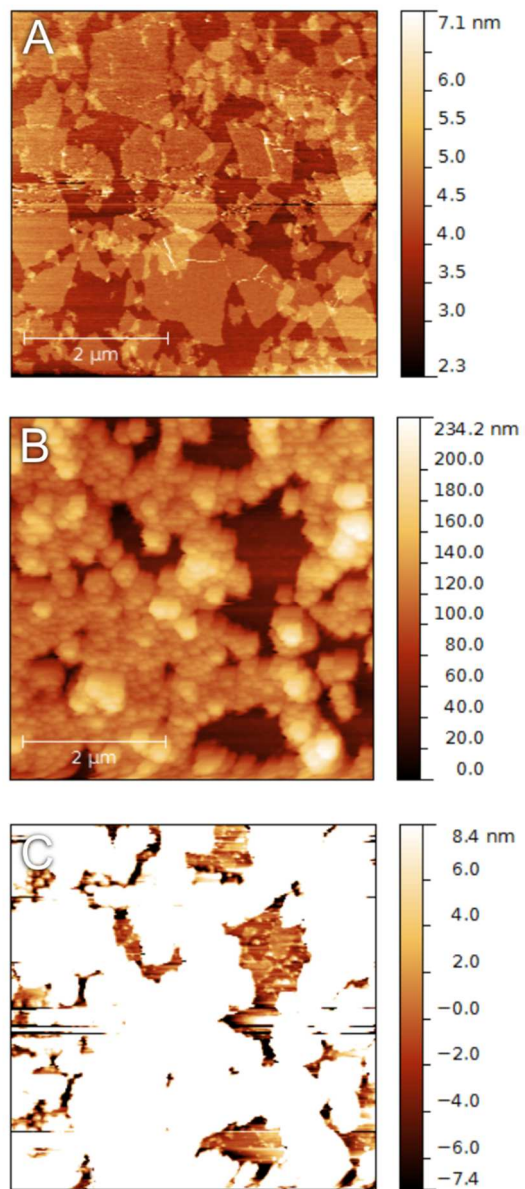


**Figure 65** GOi distributed on mica and then heated in an Ar environment to convert the GO into rGO (A). AFM images in “B” and “C” are the same scan but with the contrast adjusted to make shorter features (rGO flakes) visible in the background (C) underneath the extensive acrylic residue.

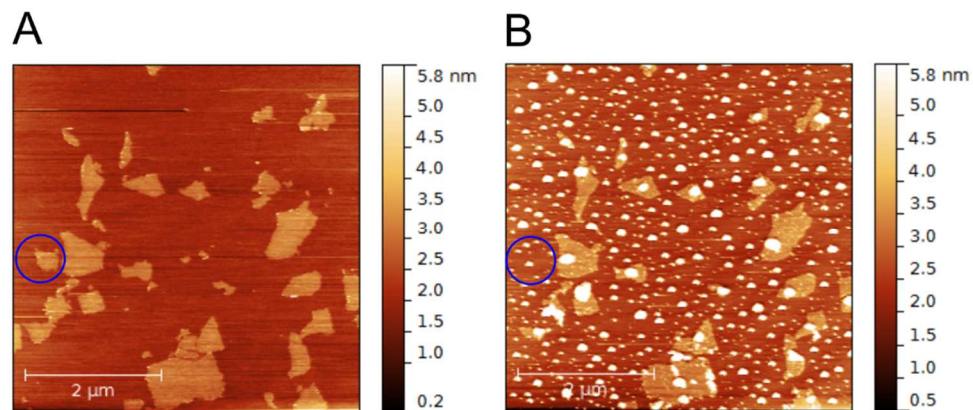


**Figure 66** GOi on silanized mica before (A) and after (B) peeling. Only one flake is clearly missing (circled in blue). There is also a lot of polymer residue remaining on the surface.

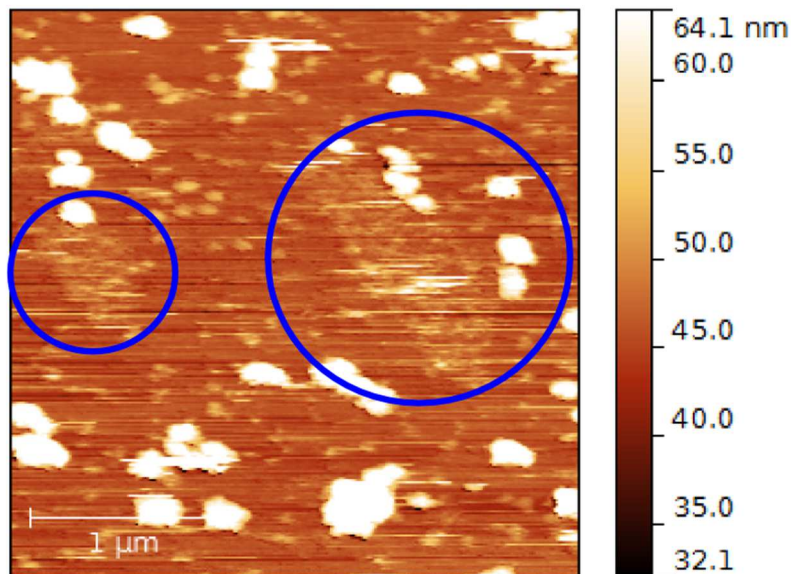


**Figure 67** Silicon/GO substrate after peeling acrylic. Faint flake-like shapes are visible in the blue circles in addition to acrylic residue.

In the case of GO on silicon, the peeling test results were less conclusive. The background of some images showed faint flake-shaped features (Figure 67), but they were not as clearly defined as results from the other peeling tests with acrylic. There

was no elevated heat in the GO-acrylic peeling test process, so the flakes should not have been degraded via reduction or oxidation. Therefore, these images probably reflect GO flakes covered with a thin layer of acrylic. If this is the case, it would suggest that the GO-silicon bond is greater than the GO-acrylic bond.

These peeling test results on acrylic are particularly interesting because they do not show any instances of polymer peeling the flakes off the substrate, other than a single flake in the GO-silanized mica scenario (Figure 66). This is regardless of the polar or nonpolar nature of the substrate or flakes. This reproducible phenomenon suggests that some other process besides surface chemistry must be affecting the interaction. The globules of acrylic residue that remained on the surface of all substrates after peeling may be the result of (a) limited contact area between flake and acrylic and (b) weak interactions within the acrylic mixture. Since most of the residue left on the substrates seems to be localized patches that look similar to the spherical bumps on the surface of the acrylic (Figure 63), it seems possible that the acrylic is composed of separate components or phases that can be separated. Regardless of the mechanism, these tests show very low adhesion between GO and acrylic and suggest that this combination would be a poor choice for developing a reinforced nanocomposite.

### c.2. Polyimide

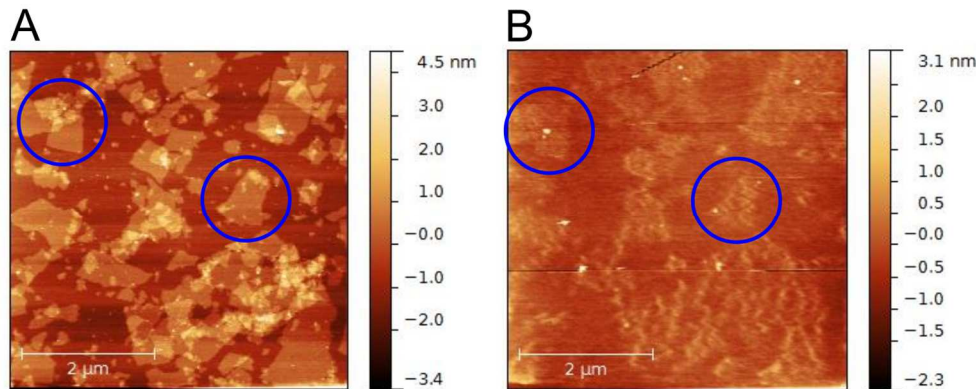


**Figure 68 GO on silanized mica substrate before (A) and rGO after (B) peeling off a PI film. The GO was reduced to rGO in the polymer during curing. Blue circles indicate the same features in both scans.**

In contrast to the acrylic peeling tests, flakes remained on the substrate in some PI peeling tests (rGO-silanized mica) but not in others (rGO-mica, rGO-silicon). These results show that the rGO-silanized mica bond is greater than the rGO-PI, rGO-mica, and rGO-silicon bonds. Since the rGO lost most of its functional groups via reduction, it makes sense that this mostly nonpolar material would bond more closely to the nonpolar silanized mica compared to the more polar PI, mica, and silicon.

Interestingly, the rGO that remained on silanized mica after peeling has a different appearance than observed in other tests: although the shapes of many flakes appear the same before and after peeling, the flakes appear distorted and blurry after peeling (Figure 68). Whole GO flakes were observed prior to PI application (Figure 68A), therefore, whatever happened to change their appearance must have occurred while curing the PI. Like all the PI peeling test samples, this PI-rGO-silanized mica sandwich

was cured at elevated temperatures in ambient pressure and atmosphere. It is possible that oxygen moved either between the substrate and polymer or through the polymer film, oxidizing and breaking apart the flakes. However, the exact reason for the change in shape is still unknown because in the case where PI peeled the rGO flakes off of mica, no change in the flake appearance was observed (Figure 69A).

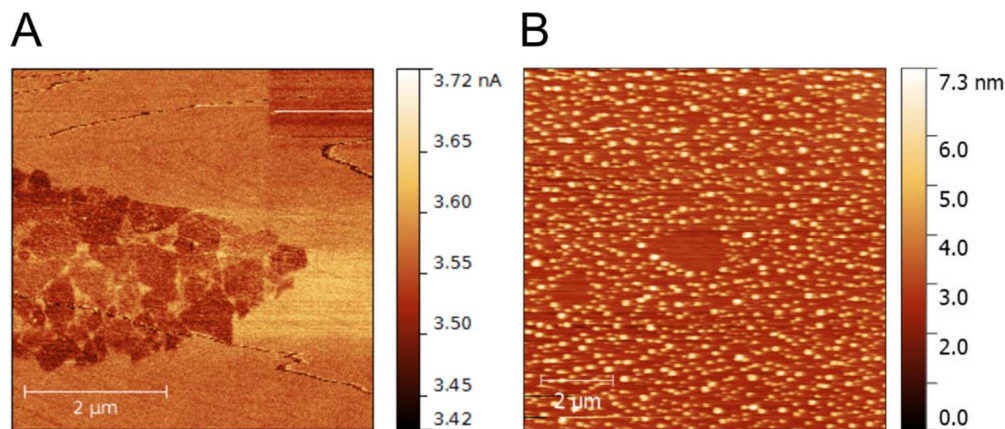


**Figure 69 Force modulation magnitude image of rGO flakes embedded in PI after being peeled off mica substrate during peeling test (A). There is a lack of rGO on silicon after peeling off the PI. Only visible droplets of polymer remain on the surface (B).**

When PI was applied to GO-coated mica and peeled off, embedded rGO, which was reduced in the polymer, was observed in force modulation scans of the PI (Figure 69A). This shows that the rGO-polyimide bond is greater than the rGO-mica bond. In contrast to the flakes on silanized mica, these embedded flakes appear similar in shape to the original flakes. If oxygen caused the flakes to break apart in the silanized mica sample, it is possible that embedding the flakes in PI held the rGO sheets together.

When the peeling test was conducted with PI applied to GO-coated silicon, where the GO was reduced in the polymer, the silicon substrate exhibited polymer residue but no

noticeable flakes (Figure 69B). Additionally, some clearly visible flake-shaped areas without residue indicate where larger flakes were peeled off. This shows that the rGO-PI bond is stronger than the rGO-silicon bond.

In summary, the relative bond strength among the PI peeling test combinations was: rGO-silanized mica > rGO-PI > rGO-mica  $\approx$  rGO-silicon. It makes sense that the nonpolar silanized mica and the rGO, which has few functional groups to make it polar, would have greater adhesion with each other than with the polar PI. This resulted in the rGO flakes remaining attached to the substrate. Since the mica, silicon, and PI are all polar, the preference of the rGO for the PI suggests that the PI is less polar than both the mica and silicon or that it conforms more closely to the rGO, resulting in an increased contact area and greater adhesion. Additionally, PI residue remained only on the silicon substrate after peeling, not on mica or silanized mica, showing that the PI-silicon bond is greater than the PI bond with any of the other substrates.

#### **d. Peeling Test/Probe Comparison**

Both the peeling tests and GO probe tests confirmed that the interaction forces in some GO-material combinations are greater than others. We explored the interactions with PI in both tests. However, we used rGO in the peeling test due to the heat required to cure PI and we used GO in the force spectroscopy experiments where the PI could be cured separately from the GO. Consequently, differences in the polarity of GO vs. rGO must be taken into consideration.

In the peeling tests, the order of adhesive pull-off preference occurred as follows: rGO-silanized mica > rGO-PI > rGO-mica. In the force spectroscopy tests with a GO-coated probe, the order of snap-down and pull-off preference occurred as follows: GO-PI > GO-mica  $\geq$  GO-silanized mica (Figure 70). These results are consistent. In the peeling tests, the nonpolar rGO displayed greater adhesion to the nonpolar silanized mica than to the polar PI and mica. In the GO-probe experiments, the polar GO was attracted more to the polar PI and mica surfaces than to the nonpolar silanized mica. Both rGO and GO exhibited a greater affinity for PI than mica.

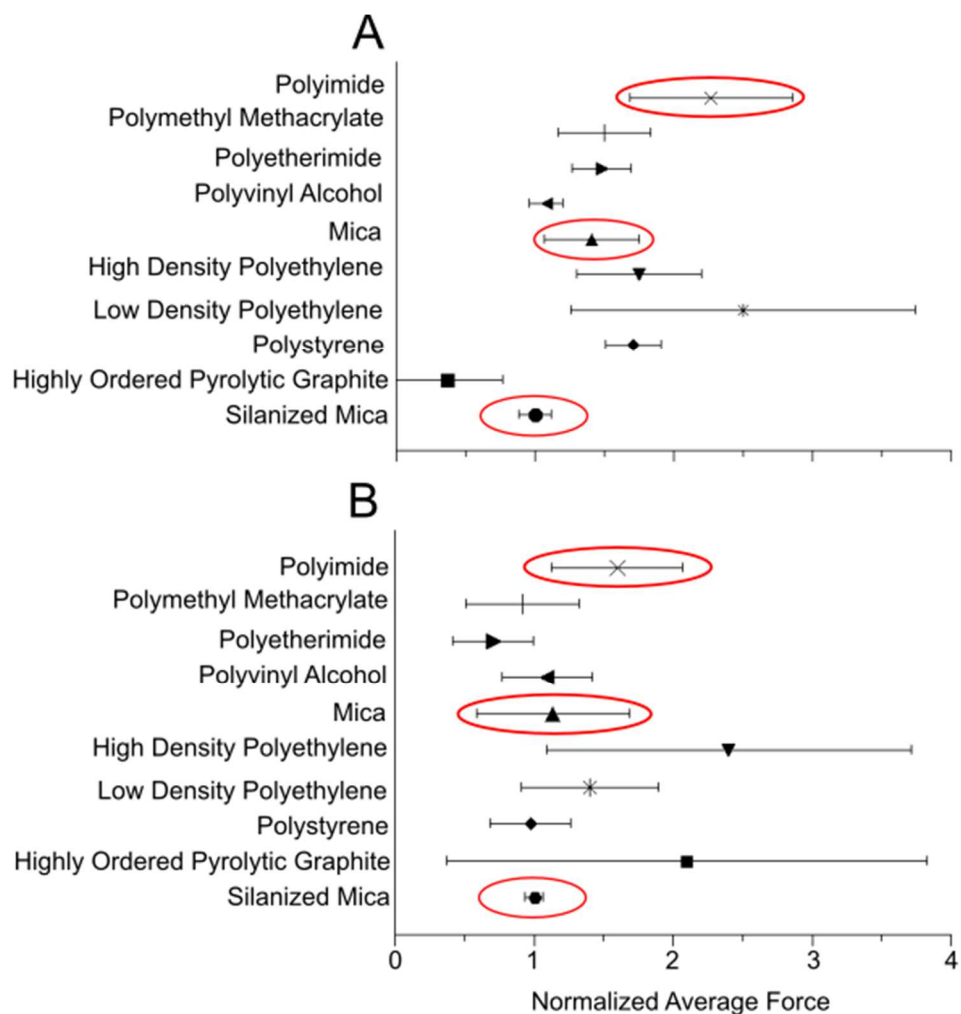


**Figure 70 Approach (A) and retract (B) force spectroscopy data using a GO probe (from Figure 61) with silanized mica, mica, and polyimide results circled to highlight differences.**

In our lab's previously published work, the peeling test results indicated that the relative interaction strength among materials was GO-PVA > GO-mica > GO-PMMA > GO-HOPG.<sup>132</sup> Here, our force spectroscopy snap-down results showed that PVA, mica, and PMMA all experienced a greater attraction to GO relative to the GO-HOPG interaction (Figure 70A). We argue that preferentially comparing our approach curve results to published peeling test results in this instance is justified. In the retract

curve measurements, the HOPG exhibited the greatest standard deviation, which suggests that the spherical probe encountered varying surface features that could have interfered with the actual force measurements. In contrast, the approach curve results exhibited the interaction forces without the influence of topography. In our experience with peeling tests, which presumably represent nanocomposite systems, the GO flakes conformed to the steps in the HOPG and so would not experience the same variability in adhesion that resulted from the hard contact of the GO coated spherical probe with the steps. Beyond the clear preference of GO for PVA, mica, and PMMA over HOPG, the error bars in our force spectroscopy results make it difficult to clearly indicate an interfacial attraction ranking between mica and PMMA. However, both exhibit greater attraction than PVA.

We have proven that the GO probe is effective at identifying the difference in interfacial attraction among multiple surfaces, and that these results are consistent with peeling test results. Therefore, if the difference between mica and PMMA samples is slighter than among HOPG and PI, then the experiments may need to merely be repeated to reduce the standard deviation of the results. Additionally, as discussed in the force spectroscopy section above, there may be some isolated substrates that lead to inherent differences between the peeling test and functionalized probe that cause them to test slightly different interactions and experimental conditions, with differing final results. In these cases, using the combined approaches of the peeling test and GO probe should provide a more complete picture of the interactions than either method alone.

### e. Conclusion

By developing a custom GO-functionalized AFM probe, we have introduced a new tool that can help screen the best GO-polymer combinations for improving the strength of polymer nanocomposites. The technique is simple to implement: the GO is electrostatically attracted to the amine-functionalized colloidal AFM probe and remained robustly attached after 1000 force curve measurements. The results that showed clear preferences in attraction of the GO probe to certain substrates are consistent with prior peeling test results. In other cases, differences that were clearly distinguishable in the peeling tests were not obvious in the force spectroscopy results. Additional development of this method could allow ever more precise ranking of interfacial attraction magnitude among these and other substrates in the future. Also, differences between the peeling test and GO probe techniques might lead to some unavoidable dissimilarities in the results.

By performing additional peeling tests with new substrates and rGO, we were able to develop a more complete picture of the interfacial interactions. In addition, we identified limitations of our experimental work and have taken steps to address them by limiting topographical features and reducing electrostatic charges. With additional testing to further perfect the probes and identify limitations, we believe that this novel tool will become a remarkable asset in determining the best nanofiller-polymer combinations for improved nanocomposites. Future work using these techniques should focus on further repetition of experiments, probing interactions on other

polymer systems, and performing more peeling tests utilizing rGO. These steps should provide critical information in the development of new nanocomposite systems containing both GO and rGO.

## **Chapter 5: Alumina Platelet Probe**

### **a. Development**

#### **a.1. Overview**

Nacre, a component of mollusk shells, is a biological material with extraordinary toughness and strength. Harnessing the mechanical properties of nacre would revolutionize structural materials, both for buildings and biological implants. Consequently, the mechanical properties and biocompatibility of nacre have been studied for many years in an attempt to develop artificial nacre composites.<sup>166–169</sup> However, developing synthetic alternatives with the same properties has remained elusive.<sup>170,171</sup> Nacre could be considered analogous to a brick wall, in which “bricks” of calcium carbonate and “mortar” of polymer form the composite.<sup>167</sup> This configuration is thought to confer nacre with its exceptional mechanical properties.<sup>168</sup> It is therefore of great interest to better understand nacre’s components and their arrangement: the brick material, mortar material, size and shape of the bricks, interactions between brick and mortar, etc. For example, clay,<sup>172</sup> alumina fibers,<sup>173</sup> and alumina platelets<sup>174</sup> have been considered as bricks. Our work aims to improve our understanding of the adhesion between alumina platelet bricks and various types of polymer mortar in order to develop a composite that more closely matches the design and properties of native nacre. To this end, we developed an alumina platelet probe for the direct measurement, via force spectroscopy, of the interactions between an alumina platelet and various polymer substrates. Although alumina spheres are available to

create colloidal alumina probes,<sup>175</sup> we chose to work with platelets in order to mimic the flattened morphology found in nacre.

## a.2. Construction

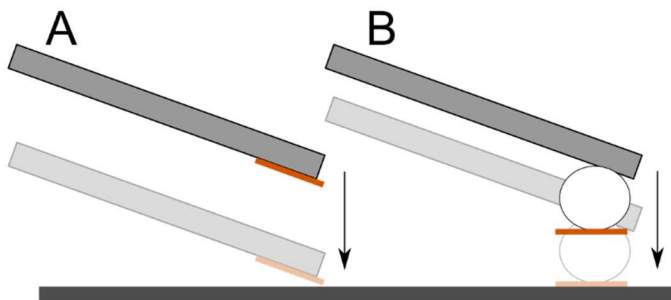


**Figure 71 Graphic indicating the contact between two designs of alumina platelet probe: the angled platelet probe, i.e. where the platelet is flush with the cantilever, (A) and the parallel platelet probe, i.e. attached to a colloidal probe (B).**

Functionalizing an AFM probe with a flat platelet that is several microns in diameter presents a special challenge. In a standard AFM setup, the cantilever is tilted as it approaches the substrate. The tilt degree depends on the AFM manufacturer. Therefore, only the edge of the platelet will contact the surface if a platelet is flush against the cantilever, i.e. angled platelet probe (Figure 71A). However, if a platelet is attached to a colloidal probe, it can be oriented parallel to the substrate, allowing the entire platelet area to contact the surface, i.e. parallel platelet probe (Figure 71B). Both of these attachment options provide opportunities for experimentation. The edge provides a smaller contact area so the spring constant need not be as large to pull the probe off the substrate. However, the contact area of the edge, which is necessary for quantitative comparisons of the force response between probes, is difficult to determine. In contrast,

the parallel platelet probe provides a more quantifiable contact area. Due to their different advantages, we worked to develop both types of probes.

Choosing a cantilever with a suitable spring constant represents an additional challenge. If the spring is too weak, the range required to retract the probe off the substrate is greater than the measuring capabilities of our AFM. For example, when the cantilever bends beyond small displacement angles, the sensitivity of the photodiode to the moving laser beam is no longer linear, i.e. no longer calibrated. Additionally, our piezoelectric device can only retract by a few microns. If the probe remains attached to the substrate so that it must be retracted beyond this range, then the laser beam will experience such large deflections that it will no longer contact the photodiode. In contrast, if the spring is too stiff, the cantilever force sensitivity will be hindered, making it impossible to measure weak interactions. The contact area of the platelets we employed exceeds that of a multi-micron diameter colloidal probe, which makes a much larger contact with the substrate, i.e. much greater force. We used a tapping mode cantilever (40 N/m) to construct the angled platelet probe shown in Figure 71A and are still determining the necessary spring constant for the parallel platelet probe in Figure 71B.

For both probe designs, it was crucial to first disperse alumina platelets onto a glass slide before making the probes, as the thin residual layer of water between the probes and glass surface made it easier to remove individual platelets and attach them to the cantilever. In contrast, on older samples that lacked a water layer, the alumina platelets remained strongly attached to the glass surface. For the parallel platelet probes, we

magnetically attached the SMENA tip holder to a translation stage mounted on an Olympus inverted microscope (Figure 72). This allowed us to attach the platelet in the same orientation as it would be used in the AFM: with the platelet parallel to the substrate.

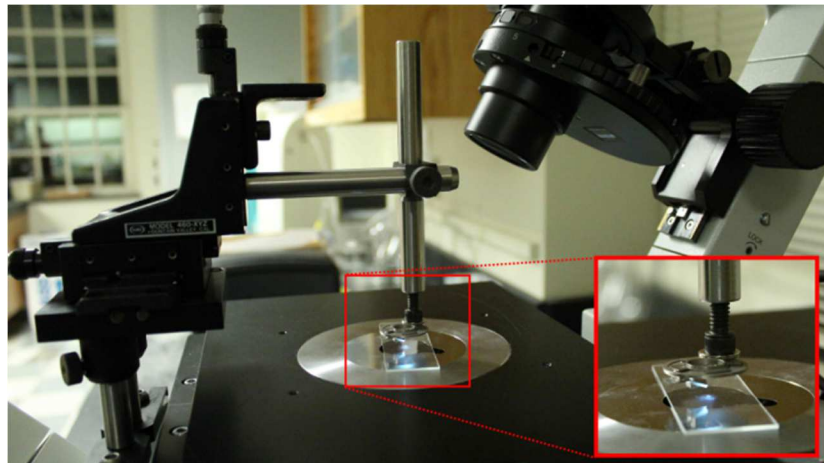


**Figure 72 Optical image of Olympus inverted microscope with translation stage and SMENA tip holder in orientation to construct an alumina platelet probe.**

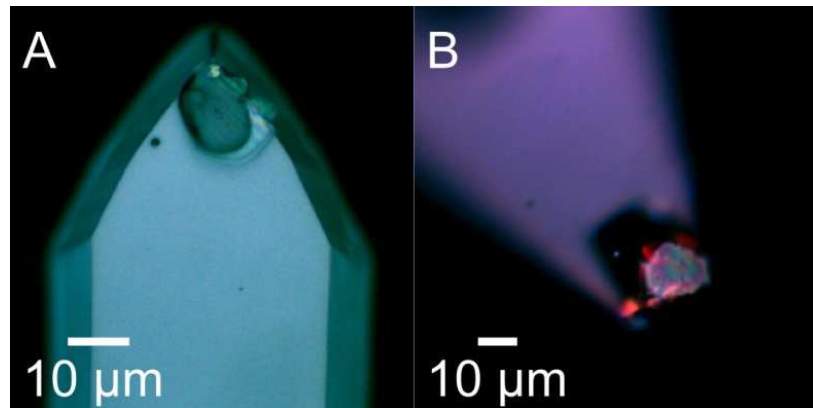


**Figure 73 Optical image of alumina platelets attached to AFM cantilevers with epoxy.**

Next, a nanoliter quantity of epoxy was required to attach the probe to the cantilever. We found that by mixing epoxy (Ace Hardware Quick Set epoxy), barely touching the epoxy with a human eyelash, and then dragging the eyelash over a glass cover slide,

we were able to find epoxy droplets on the surface with a much smaller width than that of the cantilever. We used the translation stage to lower the cantilever onto one of these small epoxy droplets, then retracted the probe, translated it laterally, and lowered it onto a single alumina platelet. Optical images of two probes are included in Figure 73. To confirm correct construction of the angled platelet probe design in Figure 71A, we scanned the probe on an NT-MDT calibration grating (TGT1). The resulting scan image clearly showed if the triangular end of the cantilever was touching the substrate (Figure 74A) or if the layered alumina platelet edge extended beyond the cantilever (Figure 74B). This scan was therefore used to confirm that the alumina probe was constructed correctly: with the alumina in a position to make contact with the substrate (Figure 74B).

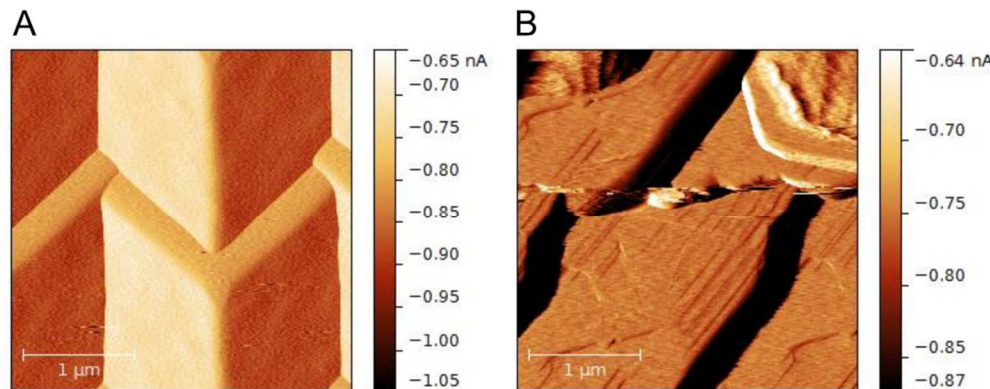


**Figure 74 Contact mode vertical deflection (DFL) images of the triangular end of a bare cantilever (A) and an alumina platelet probe (B).**

### a.3. Functionalization

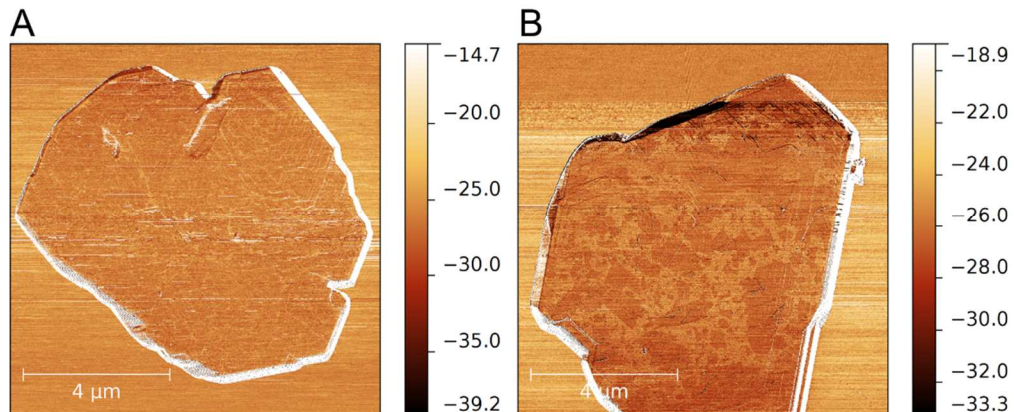


**Figure 75** AFM phase images showing an alumina platelet on a mica substrate (A) and a similar platelet which has been dipped in a GO dispersion (B). The second platelet clearly shows GO flakes attached to its surface with none on the surrounding mica.

In addition to constructing the alumina platelet probes, we also explored ways in which they might be functionalized. One option involved uniting GO with the alumina platelets, which could provide additional strengthening of the nanocomposite and provide alternative, potentially advantageous adhesion with other polymer matrices. Combining these two materials was a simple process: since the isoelectric point of the alumina platelet confers a positive charge to its surface when submerged in a GO/water dispersion,<sup>176</sup> the alumina and GO are naturally attracted to each other. To exhibit this interaction, we shook a bottle of alumina flakes dispersed in Millipore water (1 wt%) and spin-coated a sample (1 μL) onto a mica substrate (3 minutes, 3000 rpm). We then applied 1 μL of 0.046 wt% GO dispersion to the substrate, allowed it to remain on the surface for a few minutes, and rinsed the surface with 50 μL of Millipore water to remove any loosely bound GO flakes. Next, we spin-coated the substrate to remove

excess water (3 minutes, 3000 rpm). The order of this procedure is critical. By drop-casting the GO dispersion, we allow it to preferentially attach to the positively charged alumina and be repelled from the negatively charged mica.<sup>104</sup> Spin-coating at this stage would have indiscriminately applied the GO to the surface and alumina alike. Phase images from tapping mode scans show alumina platelets without (Figure 75A) and with (Figure 75B) GO flakes present, with GO flakes darker in contrast to the alumina platelets. Similarly, making a GO functionalized alumina platelet probe should be as simple as dipping the probe in a GO dispersion.

## b. Results and Discussion

### b.1. Force Spectroscopy

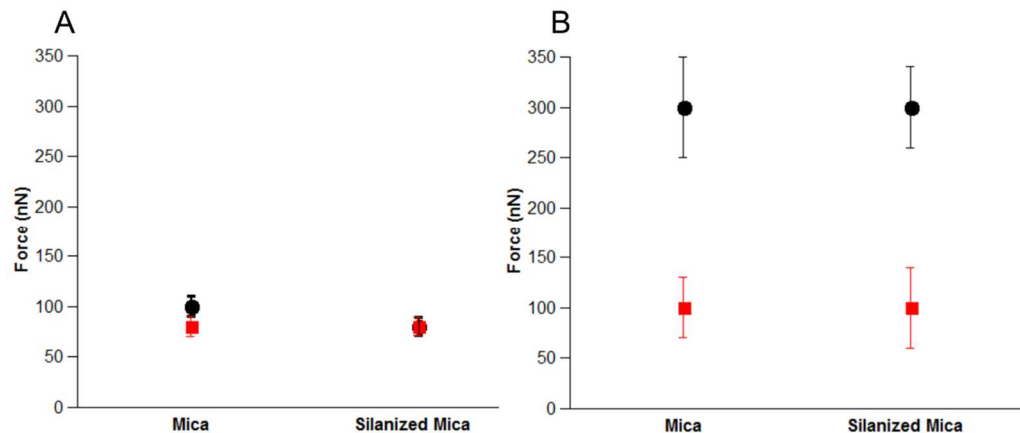


**Figure 76** Initial (A) and repeated (B) force spectroscopy measurements between angled alumina platelet probe and substrates. The black circles indicate the average retract curve adhesion and the red squares indicate the average approach curve attraction. The error bars are standard deviations of the averages.

After successful construction of the angled platelet probe (Figure 73A), we performed force spectroscopy measurements between the probe and two substrates: mica and

silanized mica. These substrates were employed to provide atomically flat surfaces with very different surface chemistry—polar and nonpolar, respectively. We performed the force spectroscopy measurements twice to provide initial and repeated measurements, utilizing the same piece of silanized mica and two different pieces of non-silanized mica. In each case, we collected 100 force curves in a  $10 \times 10$  grid pattern.

In both experimental sets (Figure 76), we saw no substrate-dependent difference in van der Waals attraction, as indicated by the same attraction force values for both substrates (red scatter points in Figure 76). However, changes in the measured approach curve attractive force were observed in the repeated measurements, i.e. the magnitude of the attractive force was greater in the repeated experiment than in the initial experiment. This is likely due to a greater contact area between the probe and substrate. In the contact mode scans performed before the force curves, we observed some small pieces of platelet break off the probe. This could have led to a greater contact area as small protruding pieces were worn off leaving behind a larger smooth area.

The magnitude of the adhesive force also changed after repeated measurements. The initial set of measurements exhibited adhesion values near 100 nN (Figure 76A) but in the repeated set they increased to 300 nN (Figure 76B). This increase in magnitude would also be consistent with an increased contact area resulting from small protruding pieces breaking off to leave a larger smooth contact area.

In the repeated measurements, another change occurred: there was no difference in the adhesion as a function of substrate type. This observation contradicts the results in our initial experiment, which showed greater adhesion for non-silanized mica than for

silanized mica. The reason for this change could be due to the new piece of non-silanized mica that we used for the repeated experiments. Perhaps there were slight differences in the surface forces for the two different pieces of mica, differences in the amount of surface charging, or different contaminants adsorbed from the air. Further repetition and control of the experiment should help clarify these questions.

## b.2. Friction Measurements

In an alumina-polymer nanocomposite, any stretching applied to the composite would result in shear or friction in the case of slippage between the platelet and polymer. Therefore, conducting friction measurements between a consistent, alumina platelet and multiple flat polymer substrates should provide direct, comparable evidence of which combinations would yield the strongest alumina-polymer bond in a shearing situation. This maximization of interfacial bonding would consequently inform the development of the strongest nanocomposites. To test this theory, we performed preliminary experiments comparing the friction between an angled alumina platelet probe (Figure 73A) and two substrates: mica and silanized mica. We chose these two substrates as a proof of principle experiment, as they are both rigid compared to a deformable polymer and display minimal surface topography, yet exhibit polar and nonpolar surface chemistry, respectively.

Prior to the experiment, we stored both substrates in a humid environment for several days. As our tests with the GO coated colloidal probes indicated (see Graphene Oxide Functionalized Probe), performing force spectroscopy measurements with such a large

probe in air can be difficult if the electrostatic forces from charged samples are too strong. After reducing the surface charge, we performed contact mode scans on both substrates. The fast line of each scan was conducted perpendicular to the position of the cantilever so that the lateral force (LF) images show the torque on the cantilever as it is moved laterally. Greater torque on the cantilever, i.e. a larger value in the LF scan would thus imply a greater frictional force between alumina and polymer. We performed scans of two different areas— $3\text{ }\mu\text{m} \times 3\text{ }\mu\text{m}$  and  $20\text{ }\mu\text{m} \times 20\text{ }\mu\text{m}$ —to ensure that the tip did not remain attached to one location in the previous smaller scan.

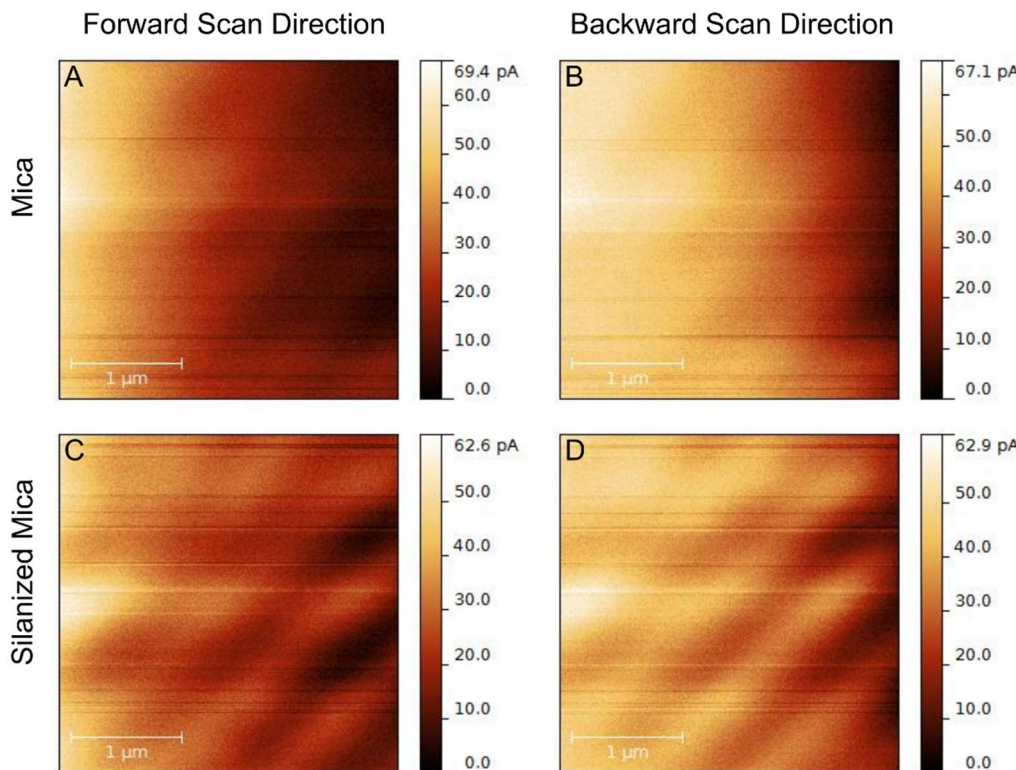


**Figure 77** Raw lateral force images for friction measurements on mica (A, B) and silanized mica (C, D) in the forward (A, C) and backward (B, D) scan directions.

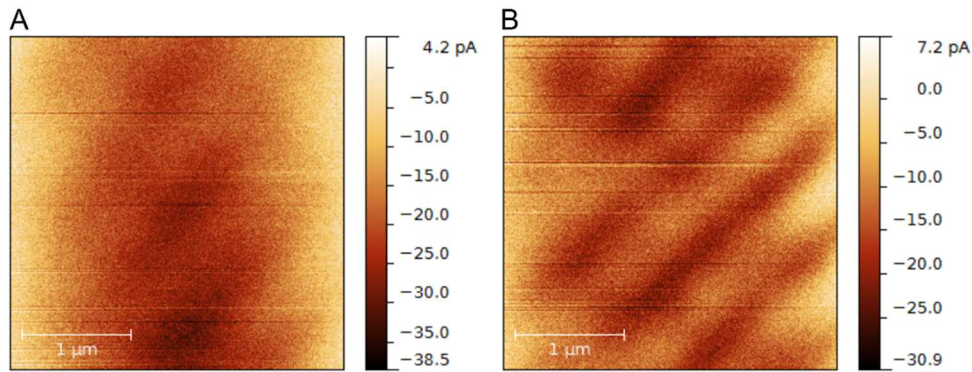


**Figure 78 Subtracted images of mica (A) and silanized mica (B). The average values for each image are 17.01 pA for mica and 12.81 pA for silanized mica.**

To quantify the friction of alumina probe against each substrate, we subtracted the forward scan and backward scan images from one another using Gwyddion (Figure 77 and Figure 78). The average LF value of the scan can then be computed to give a metric of the friction force. For the set of scans shown in Figure 78, the average values were 17.01 pA for mica and 12.81 pA for silanized mica. Thus, a greater frictional force was observed between alumina and mica. We can determine this comparison even without laterally calibrating the cantilever. By performing measurements sequentially on the non-silanized mica and silanized mica without changing the laser alignment, we can directly show on which substrate the cantilever exhibited the greatest torque, i.e. the greatest friction.

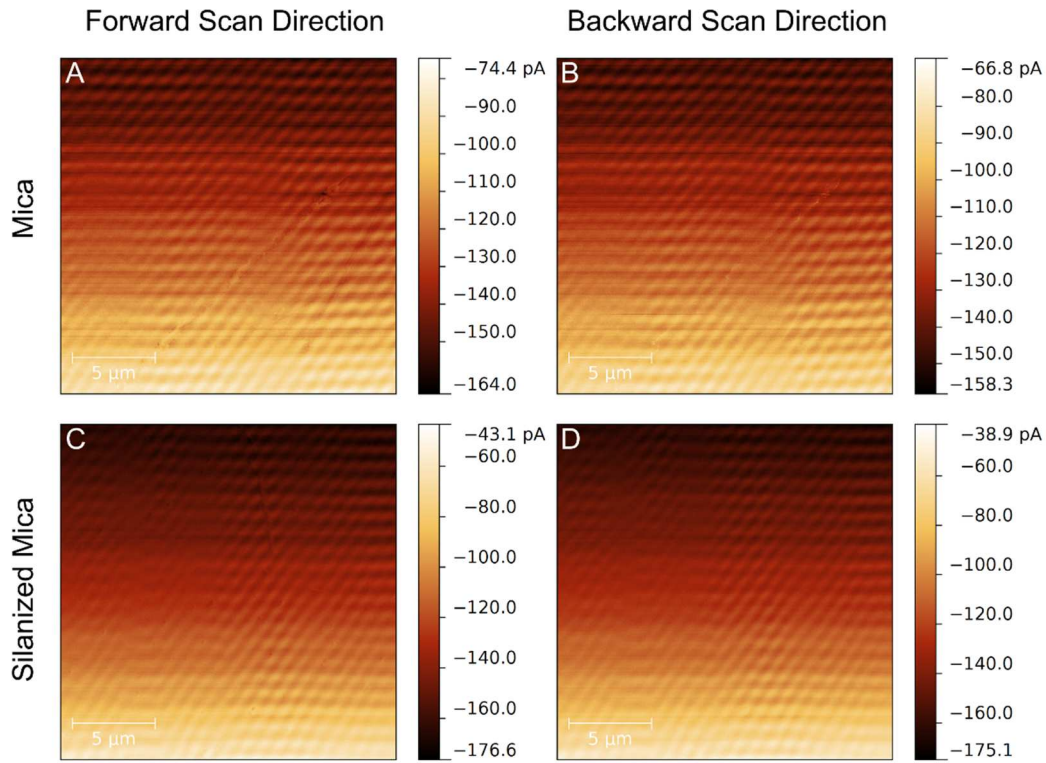


**Figure 79** Raw AFM lateral force scans on mica (A, B) and silanized mica (C, D) in the forward (A, C) and backward (B, D) scan directions.

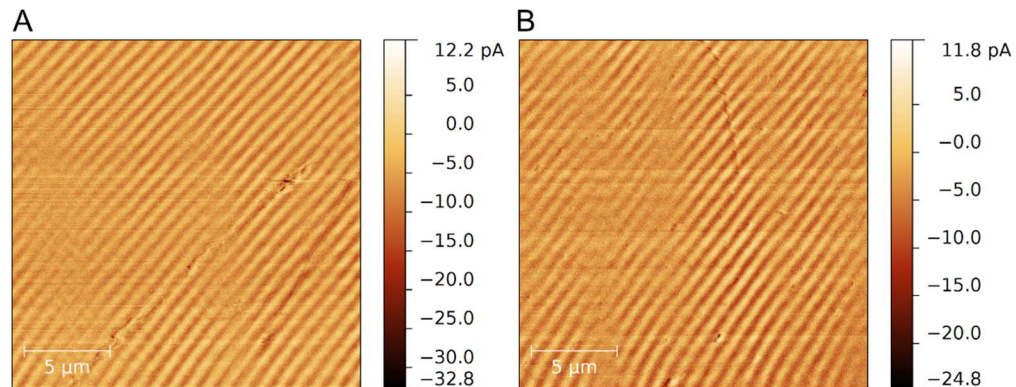


**Figure 80** Subtracted LF images of mica (A) and silanized mica (B). The average values for the two images are 5.34 pA for mica and 3.12 pA for silanized mica.

We repeated the scanning on a  $20 \mu\text{m} \times 20 \mu\text{m}$  area (Figure 79) and performed the same subtracting procedures (Figure 80). In these scans, an average lateral force of

5.34 pA was observed for mica and 3.12 pA for silanized mica, again showing that friction between mica and alumina was greater than between alumina and silanized mica.

### c. Conclusion

Understanding the interfacial adhesion between alumina platelets and various polymer surfaces is a crucial step in the development and design of synthetic nacre-like composites. We have developed two forms of an alumina platelet AFM probe, angled-platelet and parallel-platelet, and introduced a method of functionalizing a probe with GO flakes. We then demonstrated the capability of these probes to perform both force spectroscopy and friction measurements on flat surfaces with different surface chemistries. Our preliminary results showed a greater frictional force between the alumina probe and a polar mica surface than between the alumina and a nonpolar silanized mica surface. Future work with this probe and various polymer substrates should further elucidate the force interactions within alumina-polymer nanocomposites and enhance our capability for designing custom nanocomposite systems.

## **Chapter 6: Conclusions and Future Work**

### **a. Overview**

In this dissertation, we present novel functionalized AFM probes designed to enhance progress, reduce cost, and decrease time in two important industrial fields: petroleum recovery and nanocomposite design. Our custom probes explore the relevant surface interactions in each system to increase knowledge and predictive capabilities. Since these types of measurements were not possible prior to the development of these probes, they represent major technological advances in their respective fields.

### **b. Petroleum Recovery**

In petroleum recovery, our custom probes can be used to develop tailored injection brines that would result in maximized petroleum yields. The ideal customized brine would cause free-floating oil to be repelled from mineral surfaces and adhered oil to loosen, resulting in a larger percentage of oil that could be flushed from the reservoir. This would improve the efficiency of oil recovery and viability of previously abandoned wells. Our initial results utilizing this custom probe reveal the benefits, challenges, and limitations of this work that warrant further study.

When we conducted force spectroscopy measurements between dried “A” oil coated probes and a mica substrate in 1 mM and 10 mM NaCl solutions, the greatest repulsion in the approach curves occurred for the 1 mM NaCl solution, as expected by electric double layer theory. This result showed that (a) our dried oil probe retained the charged components of wet crude oil, (b) these charged components responded in a manner

expected by theory, (c) each probe was robust enough to perform repeated measurements, and (d) the technique for manufacturing the probes was consistent over multiple tests. After this initial series of tests, we gradually adjusted the parameters of our experiment to increase the overall complexity, first by experimenting with different oils, then with substrates that expressed rough topography, and finally under conditions in a single reservoir system. Each of these sets of experiments is addressed in the following section.

To confirm oil-dependent variations in interaction forces, we conducted force spectroscopy experiments using three different crude oils in 1 mM and 10 mM NaCl brines. We found distinct differences in the approach curves as a function of oil type, reaffirming the observation that unique oil reservoirs respond differently to the same injection liquid. The origins and chemical characteristics of our oils were proprietary, but our tests suggest that combining this information with repeated dried oil probe experiments of many different oils should yield fascinating and useful data.

Our force spectroscopy measurements on rough mineral grains provided perhaps the most realistic experimental conditions. In both sets of experiments, e.g. simple and complex brines, we observed more instances of repulsion in the lower salinity brine (1 mM NaCl for the simple brines and “low salinity brine” for the complex brines). There was no clear dependence of adhesion on salinity in the simple brine (1 mM and 10 mM NaCl) experiments, however, the complex brine experiments did exhibit a trend. Interestingly, the adhesion results indicated differences as a function of oil dryness. The two probes dried for shorter periods of time showed gradually decreasing

adhesion over the course of the experiments, while the two probes dried for longer times showed a clear transition with no gradual trends after repeated measurements. These results reinforce the importance of oil drying to obtaining consistent results. Additionally, the variability in the adhesion measurements taken over a grid on a rough mineral grain highlight the usefulness of collecting data over a large number of locations to average the forces on a heterogeneous sample.

In summary, in the dried “A” oil probe experiments we utilized a combination of substrates (mica, “A” mineral grains) and solutions (single and multi-salt brines). Interestingly, there were more instances of repulsion and, in some cases, a greater magnitude of repulsion at lower salinities, regardless of substrate or brine type. Additionally, in cases where we saw clear trends in adhesion, there was greater adhesion at lower salinities. These are interesting trends that reinforce the important role that the oil composition holds in the reservoir interactions. They suggest that for the “A” reservoir using a lower salinity brine as an injection liquid would cause free-floating oil to be repelled from rock surfaces and already adhered oil to bond tightly. Therefore, cycling through multiple brines of varying salinities might be the most effective method for removing both free-floating and already adhered oil.

As we have demonstrated, all future tests would benefit from the experimental details of (a) careful monitoring of the oil dryness on the probe and (b) collecting measurements over a grid on heterogeneous substrates. Future work should draw heavily from these experiments, especially by following the order of complexity that we utilized. An important set of experiments would involve repeating our experiments

with a dried oil probe, simple brine, and mica substrate, and utilizing new crude oils instead of those we employed here. Not only would this provide important information detailing the differences among crude oils, but it would also provide further groundwork for experiments of greater complexity, e.g. rough mineral grains and complex brines. These experiments could also be repeated with a variety of single salt brines to observe the effects of different ions on the interactions. Finally, we believe that repeating our most challenging experiments—utilizing rough grains, dried oil probes, and complex brines—for multiple reservoirs, then comparing the tests to the actual reservoir recovery output levels, would provide the most useful and exciting results.

### **c. Nanocomposites**

Our GO-coated and alumina probes have the potential to streamline the optimization of nanocomposite combinations. Traditionally, mechanical tests of graphene nanocomposites are performed after (a) uniformly dispersing GO flakes into the polymer and (b) processing the nanocomposite without defects, two steps that require substantial time and resources. By first determining the optimal combinations of GO and polymer with small quantities of each, our method should save significant time, materials, and financial resources. More importantly, quantitatively measuring the forces at the nanoscale should allow a previously unavailable type of designed nanocomposites to be developed in which we can predict the material properties. Our

initial experiments provide a clear method for manufacturing these probes and present the first evidence of improvements and challenges in these systems.

In the course of developing the probe, we characterized the attachment of the GO to the probe using optical, AFM, and atomic force spectroscopy techniques. Of these, atomic force spectroscopy was the most effective at demonstrating the changing interactions between the different probe coatings and a flat substrate. For our GO probe–substrate force measurements, most cases showed greater variability in the retract curve than in the approach curve data. Since the approach curves provide information about the force interactions at a larger distance, e.g. where they are not as influenced by topography as the adhesion measurements, we relied predominantly on the approach curves to compare our results among substrates. Future experiments using other substrate materials should closely monitor the effects that substrate roughness can have on the results. The best method to dealing with surface roughness is (a) trying to minimize surface topography, and (b) interpreting the combined information from the approach and retract curve data.

The force spectroscopy snap-down results of some substrates, e.g. PEI, PMMA, mica, were too similar to each other to be distinguished. However, as expected, we observed the smallest snap-down force between the GO probe and nonpolar HOPG and the next smallest as nonpolar silanized mica. This was an exciting development, because for the peeling tests previously performed with mica, PMMA, and HOPG in our lab, we saw the least interactions with HOPG. These similar results show that the two techniques

test the same forces, but the GO probe provides the added benefit of quantitatively measuring the strength of these interactions.

The GO-coated probe showed greater attraction to the PI than to other polar substrates. These results suggest that a GO-PI nanocomposite would have greater interfacial adhesion compared to other combinations, leading to increased mechanical strength. However, this type of composite could be difficult to develop. The heat required to cure the PI that we utilized reduces GO (rGO), which would likely lead to a different set of interactions. To fully explore the effect of rGO on the PI-GO system and again compare results between GO probe tests and peeling tests, we utilized PI in both the recent peeling tests and in the GO probe measurements. The interactions we observed in the peeling test can be ranked: rGO-silanized mica > rGO-PI > rGO-mica. In the GO probe experiments, we ranked the interfacial interactions as such: GO-PI > GO-mica  $\geq$  GO-silanized mica. The results of the two techniques complement each other. In the peeling tests, the nonpolar rGO-silanized mica interactions were greater than the interactions between rGO and the polar PI and mica substrates. In the force spectroscopy tests, the interaction between polar GO and the polar PI and mica substrates was greater than the interaction between polar GO and nonpolar silanized mica. Therefore, the combination of these two techniques indicates that there is a decrease in interfacial adhesion between GO and PI if the GO in the polymer is reduced. Future work with these probes should focus on testing more substrates with the GO probe and comparing the results to new peeling tests. The resulting data should provide a guide for developing reinforced polymer nanocomposites.

Similarly, our development of the alumina platelet probe should improve the development of alumina-polymer and alumina-biopolymer nanocomposites to simulate nacre. Our initial results demonstrated the two ways that these probes can be manufactured. We also showed friction and adhesion measurements between the alumina surface and two surfaces with radically different surface chemistries. Future development of this probe should involve repeating the measurements on many different substrates, including those that we used in our GO probe experiments. Additionally, performing measurements on biopolymers and observing differences as a function of humidity or environmental medium, i.e. performing experiments in aqueous solutions, should provide fascinating parallels to the natural environments in which materials like nacre are adapted to excel.

The development of oil, GO, and alumina functionalized probes provides a set of fascinating new tools with which to study challenging systems in new ways. Using these probes, our research provides the methods and inspiration necessary for great progress in oil recovery and nanocomposites, two distinct yet similar fields in which surface interactions play crucial roles.

## **Appendix A: Optical Analysis of Features in Crude Oil**

In the autumn of 2011, we used an Olympus inverted microscope to optically view droplets of crude oil on glass microscope slides. Within the droplets, we observed banded and tapered ellipse-like structures. Since that time, we have found literature articles referencing similar looking structures in AFM images taken on asphalt<sup>177,178</sup> and bitumen<sup>179–185</sup> samples. Due to the lack of consistent terminology for this feature, further references regarding its characterization were challenging to locate. Although one research group identified this structure in bitumen using an optical microscope,<sup>186</sup> we are unaware of a thorough optical analysis performed on crude oils to describe these features. Therefore, we have included a brief characterization of the features when viewed using optical microscopy techniques.

### **a. Microscopy Techniques**

We identified the features using multiple optical microscopy techniques including reflective brightfield (Figure 81A), reflective darkfield (Figure 81B), reflective differential interference contrast (DIC) (Figure 81C), and transmission (Figure 81D) microscopy. In three modes (brightfield, darkfield, and DIC), the features appear as tapered ellipses with banded stripes of light and dark across their narrow dimension. In the transmission image they appear more as wrinkled features.

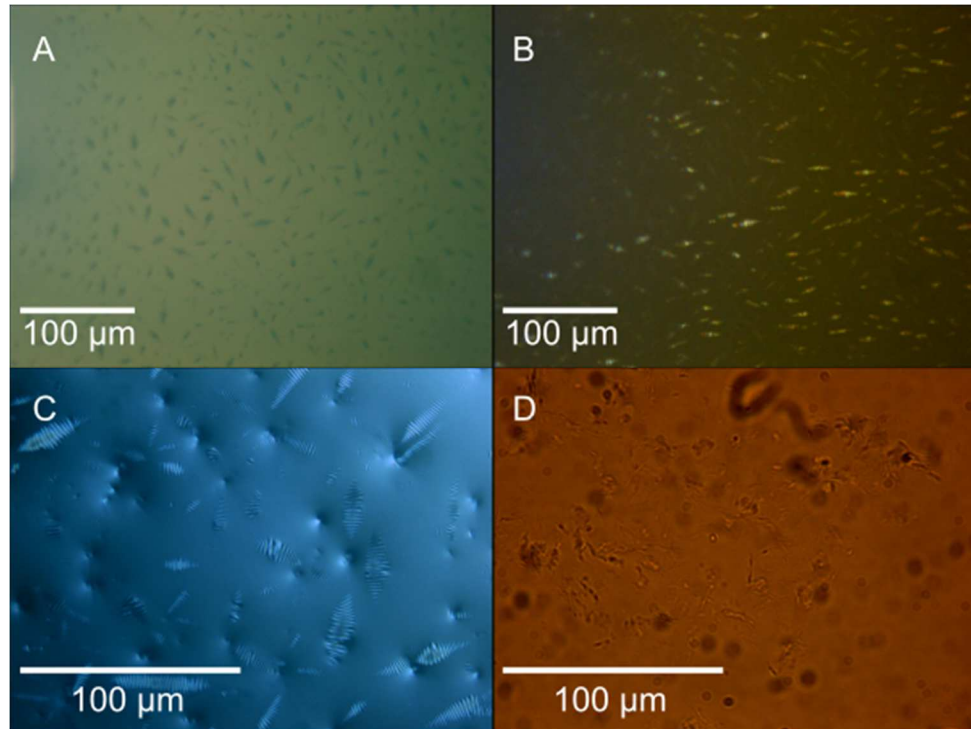


**Figure 81** Reflective brightfield (A), darkfield (B), differential interference contrast (C), and transmission (D) images of crude oil on glass. The same location is shown in both “A” and “B”.

### b. Size, Crude Oil Variety, and Shape

As Figure 82 indicates, the size varies greatly for these features. Figure 82B exhibits particularly large features in comparison to the others that we have seen. For this sample, we first combined crude oil with toluene and centrifuged it, then deposited a droplet on a glass slide for optical analysis. Since other features from the same oil were smaller in size, we do not know if the larger size is due to this additional process or if it occurred by chance. Overall, we have observed the features in five different crude oil samples taken from different wells, so we assume that these structures are common to crude oil. We know that each crude exhibits a range of sizes of this feature, however, we have not systematically viewed enough samples to know if these size ranges are oil-

dependent or if the same range is found in multiple sources. In terms of the shape and appearance, the banded pattern is common throughout all the samples we have observed. However, the shapes of these features are difficult to categorize. Although many exhibit a tapered ellipse-like shape, they are not always symmetric. Also, the ratio of their length to width is not consistent. Some exhibit the same bands for the entire length of the structure, while others have a pronounced diagonal line in the center (yellow circle in Figure 82B). Furthermore, while some of these features are clearly separate, others seem to form together with their points radiating out from a central location like petals on a flower (orange circle in Figure 82C).

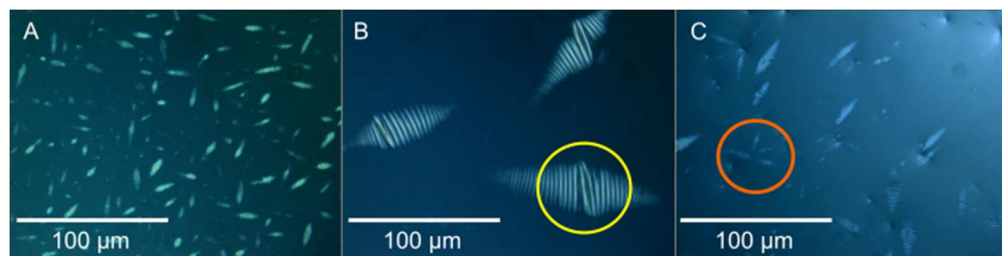


**Figure 82** These images show the varied sizes and shapes of features that we have observed. Images in “A” and “B” show the different range of size features that we have seen. Those in “B” were found in crude oil that was mixed with toluene and centrifuged.

### c. Formation and Movement Behavior

The features are not initially visible when we apply a droplet of crude oil to the glass slide. However, after spreading the crude into a thinner layer they sometimes become apparent. Therefore, we assume that either (a) they are only visible in a particular thickness of oil layer or (b) it is necessary for the oil to be a particular thickness before they form. Frequently, while viewing the oil in the microscope, we see nothing at first and then many features start to appear all over the crude oil. This is true for multiple microscopy methods. Since DIC includes polarized light, and is consequently affected

by the refractive index of the material, if the features suddenly start to appear then this suggests that they are forming as the oil thins. If they were already present, we should still be able to see them, just not in focus.

Additionally, we have observed that the features move as the oil spreads out. Sometimes they twist or turn as they move and when they collide into another feature, they stop moving. We have observed one of these features moving behind another feature so that details of one were in focus while the feature behind it was not. This suggests that they are in the bulk and are not restricted to the surface of the oil. When a strong light is shone on the oil sample from the DIC technique the features sometimes seem to melt, disappearing from view. Additionally, as the oil dries sometimes the surface takes on a granular appearance (Figure 83B).

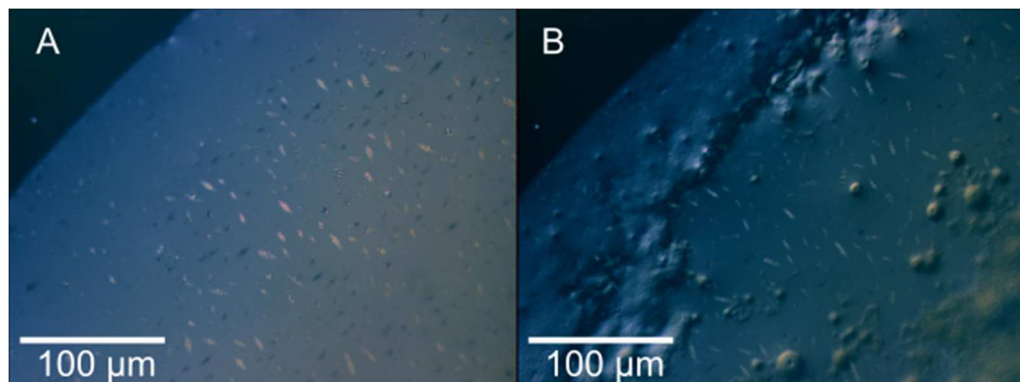


**Figure 83** Same crude oil droplet on glass before (A) and after (B) drying. Some features near the edge of the droplet are immobilized as the oil dries (B).

## References

1. Israelachvili, J. N. *Intermolecular and Surface Forces*. (Academic Press: 2011).
2. Binnig, G., Quate, C. F. & Gerber, C. Atomic Force Microscope. *Physical Review Letters* **56**, 930–933 (1986).
3. Burnham, N. A. & Colton, R. J. Measuring the nanomechanical properties and surface forces of materials using an atomic force microscope. *Journal of Vacuum Science & Technology, A: Vacuum, Surfaces, and Films* **7**, 2906–2913 (1989).
4. Weisenhorn, A. L., Hansma, P. K., Albrecht, T. R. & F., Q. C. Forces in atomic force microscopy in air and water. *Applied Physics Letters* **54**, 2651–2653 (1989).
5. Butt, H.-J., Cappella, B. & Kappl, M. Force measurements with the atomic force microscope: Technique, interpretation and applications. *Surface Science Reports* **59**, 1–152 (2005).
6. Kappl, M. & Butt, H.-J. The Colloidal Probe Technique and its Application to Adhesion Force Measurements. *Particle & Particle Systems Characterization* **19**, 129–143 (2002).
7. Eaton, P. & West, P. *Atomic Force Microscopy*. (Oxford University Press: 2010).
8. Cappella, B., Baschieri, P., Frediani, C., Miccoli, P. & Ascoli, C. Force-Distance Curves by AFM. *IEEE Engineering in Medicine and Biology Magazine* **16**, 58–65 (1997).
9. Cappella, B. & Dietler, G. Force-distance curves by atomic force microscopy. *Surface Science Reports* **34**, 1–104 (1999).
10. Cleveland, J. P., Manne, S., Bocek, D. & Hansma, P. K. A nondestructive method for determining the spring constant of cantilevers for scanning force microscopy. *Review of Scientific Instruments* **64**, 403 (1993).
11. Green, C. P. *et al.* Normal and torsional spring constants of atomic force microscope cantilevers. *Review of Scientific Instruments* **75**, 1988 (2004).
12. Hutter, J. L. & Bechhoefer, J. Calibration of atomic force microscope tips. *Review of Scientific Instruments* **64**, 1868–1873 (1993).
13. Sader, J. E. *et al.* Spring constant calibration of atomic force microscope cantilevers of arbitrary shape. *Review of Scientific Instruments* **83**, 103705 (2012).
14. Burnham, N. A., Dominguez, D. D., Mowery, R. L. & Colton, R. J. Probing the Surface Forces of Monolayer Films with an Atomic-Force Microscope. *Physical Review Letters* **64**, 1931–1934 (1990).
15. Weisenhorn, A. L., Maivald, P., Butt, H.-J. & Hansma, P. K. Measuring adhesion, attraction, and repulsion between surfaces in liquids with an atomic-force microscope. *Physical Review B* **45**, 226–232 (1992).

16. Leite, F. L. & Herrmann, P. S. P. Application of atomic force spectroscopy (AFS) to studies of adhesion phenomena: a review. *Journal of Adhesion Science and Technology* **19**, 365–405 (2005).
17. Butt, H.-J., Jaschke, M. & Ducker, W. Measuring surface forces in aqueous electrolyte solution with the atomic force microscope. *Bioelectrochemistry and Bioenergetics* **38**, 191–201 (1995).
18. Clausen-Schaumann, H., Seitz, M., Krautbauer, R. & Gaub, H. E. Force spectroscopy with single bio-molecules. *Current Opinion in Chemical Biology* **4**, 524–530 (2000).
19. Janshoff, A., Neitzert, M., Oberdörfer, Y. & Fuchs, H. Force Spectroscopy of Molecular Systems—Single Molecule Spectroscopy of Polymers and Biomolecules. *Angew. Chem., Int. Ed.* **39**, 3212–3237 (2000).
20. McConney, M. E., Singamaneni, S. & Tsukruk, V. V. Probing Soft Matter with the Atomic Force Microscopies: Imaging and Force Spectroscopy. *Polymer Reviews* **50**, 235–286 (2010).
21. Zlatanova, J., Lindsay, S. M. & Leuba, S. H. Single molecule force spectroscopy in biology using the atomic force microscope. *Progress in Biophysics and Molecular Biology* **74**, 37–61 (2000).
22. Hassenkam, T. *et al.* The low salinity effect observed on sandstone model surfaces. *Colloids and Surfaces A: Physicochemical and Engineering Aspects* **403**, 79–86 (2012).
23. Hassenkam, T., Pedersen, C. S., Dalby, K., Austad, T. & Stipp, S. L. S. Pore scale observation of low salinity effects on outcrop and oil reservoir sandstone. *Colloids and Surfaces A: Physicochemical and Engineering Aspects* **390**, 179–188 (2011).
24. Dimitriadis, E. K., Horkay, F., Maresca, J., Kachar, B. & Chadwick, R. S. Determination of Elastic Moduli of Thin Layers of Soft Material Using the Atomic Force Microscope. *Biophysical Journal* **82**, 2798–2810 (2002).
25. Indrieri, M., Podestá, A., Bongiorno, G., Marchesi, D. & Milani, P. Adhesive-free colloidal probes for nanoscale force measurements: Production and characterization. *Review of Scientific Instruments* **82**, 023708 (2011).
26. Ducker, W. A. & Senden, T. J. Measurement of Forces in Liquids Using a Force Microscope. *Langmuir* **8**, 1831–1836 (1992).
27. Hartley, P. G., Grieser, F., Mulvaney, P. & Stevens, G. W. Surface Forces and Deformation at the Oil–Water Interface Probed Using AFM Force Measurement. *Langmuir* **15**, 7282–7289 (1999).
28. Hogshead, C. G., Manias, E., Williams, P., Lupinsky, A. & Painter, P. Studies of Bitumen–Silica and Oil–Silica Interactions in Ionic Liquids. *Energy Fuels* **25**, 293–299 (2011).
29. Lee, S. & Sigmund, W. M. AFM study of repulsive van der Waals forces between Teflon AF<sup>TM</sup> thin film and silica or alumina. *Colloids and Surfaces A: Physicochemical and Engineering Aspects* **204**, 43–50 (2002).

30. Liu, J., Xu, Z. & Masliyah, J. Studies on Bitumen—Silica Interaction in Aqueous Solutions by Atomic Force Microscopy. *Langmuir* **19**, 3911–3920 (2003).
31. Zou, Y., Jayasuriya, S., Manke, C. W. & Mao, G. Influence of Nanoscale Surface Roughness on Colloidal Force Measurements. *Langmuir* **31**, 10341–10350 (2015).
32. Long, J., Xu, Z. & Masliyah, J. H. Role of illite–illite interactions in oil sands processing. *Colloids and Surfaces A: Physicochemical and Engineering Aspects* **281**, 202–214 (2006).
33. Basu, S. & Sharma, M. M. Measurement of Critical Disjoining Pressure for Dewetting of Solid Surfaces. *Journal of Colloid and Interface Science* **181**, 443–455 (1996).
34. Basu, S. & Sharma, M. M. Characterization of Mixed-Wettability State in Oil Reservoirs by Atomic Force Microscopy. *SPE Journal* **2**, 427–435 (1997).
35. Basu, S. & Sharma, M. M. Investigating the Role of Crude-Oil Components on Wettability Alteration Using Atomic Force Microscopy. *SPE Journal* **4**, 235–241 (1999).
36. Liu, J., Xu, Z. & Masliyah, J. Colloidal forces between bitumen surfaces in aqueous solutions measure with atomic force microscope. *Colloids and Surfaces A: Physicochemical and Engineering Aspects* **260**, 217–228 (2005).
37. Liu, J., Xu, Z. & Masliyah, J. Interaction forces in bitumen extraction from oil sands. *Journal of Colloid and Interface Science* **287**, 507–520 (2005).
38. Liu, J., Zhang, L., Xu, Z. & Masliyah, J. Colloidal Interactions between Asphaltene Surfaces in Aqueous Solutions. *Langmuir* **22**, 1485–1492 (2006).
39. Giesbers, M., Kleijn, J. M., Fleer, G. J. & Stuart, M. A. C. Forces between polymer-covered surfaces: a colloidal probe study. *Colloids and Surfaces A: Physicochemical and Engineering Aspects* **142**, 343–353 (1998).
40. Martin-Olmos, C., Rasool, H. I., Weiller, B. H. & Gimzewski, J. K. Graphene MEMS: AFM Probe Performance Improvement. *ACS Nano* **7**, 4164–4170 (2013).
41. Israelachvili, J. N. *Intermolecular and Surface Forces*. (Academic Press: 2011).
42. Burnham, N. A., Colton, R. J. & Pollock, H. M. Interpretation of force curves in force microscopy. *Nanotechnology* **4**, 64–80 (1993).
43. Martin, Y., Abraham, D. W. & Wickramasinghe, H. K. High-resolution capacitance measurement and potentiometry by force microscopy. *Applied Physics Letters* **52**, 1103 (1988).
44. Terris, B. D., Stern, J. E., Rugar, D. & Mamin, H. J. Contact Electrification Using Force Microscopy. *Physical Review Letters* **63**, 2669–2672 (1989).
45. Erlandsson, R., McClelland, G. M., Mate, C. M. & Chiang, S. Atomic force microscopy using optical interferometry. *Journal of Vacuum Science & Technology A* **6**, 266 (1988).
46. Hao, H. W., Baró, A. M. & Sáenz, J. J. Electrostatic and contact forces in force microscopy. *Journal of Vacuum Science & Technology B* **9**, 1323–1328 (1991).

47. Jones, R., Pollock, H. M., Cleaver, J. A. S. & Hodges, C. S. Adhesion Forces between Glass and Silicon Surfaces in Air Studied by AFM: Effects of Relative Humidity, Particle Size, Roughness, and Surface Treatment. *Langmuir* **18**, 8045–8055 (2002).
48. Schönenberger, C. & Alvarado, S. F. A differential interferometer for force microscopy. *Review of Scientific Instruments* **60**, 3131 (1989).
49. Derjaguin, B. V. & Landau, L. The theory of stability of highly charged lyophobic sols and Coalescence of highly charged particles in electrolyte solutions. *Acta Physicochimica URSS* **14**, 633 (1941).
50. Verwey, E. J. W. & Overbeek, J. T. G. *Theory of the Stability of Lyophobic Colloids*. (Elsevier Publishing Inc.: New York, 1948).
51. Parsegian, V. A. *VAN DER WAALS FORCES: A Handbook for Biologists, Chemists, Engineers, and Physicists*. (Cambridge University Press: 2006).
52. Tabor, D. & Winterton, R. H. S. The direct measurement of normal and retarded van der Waals forces. *Proceedings of the Royal Society of London Series A* **312**, 435–450 (1969).
53. Bergström, L. Hamaker constants of inorganic materials. *Advances in Colloid and Interface Science* **70**, 125–169 (1997).
54. Johnson, K. L., Kendall, K. & Roberts, A. D. Surface energy and the contact of elastic solids. *Proceedings of the Royal Society of London* **324**, 301–313 (1971).
55. Derjaguin, B. V., Muller, V. M. & Toporov, Y. P. Effect of Contact Deformations on the Adhesion of Particles. *Journal of Colloid and Interface Science* **53**, 314–326 (1975).
56. Maugis, D. & Pollock, H. M. Surface Forces, Deformation and Adherence at Metal Microcontacts. *Acta Metallurgica* **32**, 1323–1334 (1984).
57. Rabinovich, Y. I. *et al.* Capillary forces between surfaces with nanoscale roughness. *Advances in Colloid and Interface Science* **96**, 213–230 (2002).
58. Xiao, X. & Qian, L. Investigation of Humidity-Dependent and Capillary Force. *Langmuir* **16**, 8153–8158 (2000).
59. Hyne, N. J. *Nontechnical Guide to Petroleum Geology, Exploration, Drilling, and Production*. (Penn Well Corporation: 2001).
60. Agbalaka, C., Dandekar, A. Y., Patil, S. L., Khataniar, S. & Hemsath, J. R. The Effect of Wettability on Oil Recovery: A Review. *SPE Asia Pacific Oil & Gas Conference and Exhibition* (2008).
61. Sharma, M. M. & Filoco, P. R. Effect of Brine Salinity and Crude-Oil Properties on Oil Recovery and Residual Saturation. *SPE Journal* **5**, 293–300 (2000).
62. Dake, L. *Fundamentals of Reservoir Engineering*. (Elsevier: Oxford, UK, 1978).
63. Huang, J. S. & Varadaraj, R. Colloid and interface science in the oil industry. *Current Opinion in Colloid & Interface Science* **1**, 535–539 (1998).

64. Mugele, F. *et al.* Insights From Ion Adsorption and Contact-Angle Alteration at Mineral Surfaces for Low-Salinity Waterflooding. *Society of Petroleum Engineers Journal* (2016).
65. Lager, A., Webb, K. J., Collins, I. R. & Richmond, D. M. LoSal(TM) Enhanced Oil Recovery: Evidence of Enhanced Oil Recovery at the Reservoir Scale. *2008 SPE/DOE Improved Oil Recovery Symposium* 1–12 (2008).
66. Skrettingland, K., Holt, T., Twehey, M. T. & Skjevrak, I. Snorre Low-Salinity-Water Injection—Coreflooding Experiment and Single-Well Field Pilot. *SPE Reservoir Evaluation & Engineering* **14**, 182–192 (2011).
67. Suijkerbuijk, B. M. J. M. *et al.* The Development of a Workflow to Improve Predictive Capability of Low Salinity Response. *International Petroleum Technology Conference* (2013).
68. Zhang, Y. & Morrow, N. R. Comparison of Secondary and Tertiary Recovery With Change in Injection Brine Composition for Crude Oil/Sandstone Combinations. *SPE/DOE Symposium on Improved Oil Recovery* 1–14 (2006).
69. Cuiec, L. E. Restoration of the Natural State of Core Samples. *50th Annual Fall Meeting of the Society of Petroleum Engineers of AIME* (1975).
70. Tissot, B. P. & Welte, D. H. *Petroleum Formation and Occurrence*. (Springer-Verlag: 1984).
71. Yangming, Z., Huanxin, W., Zulin, C. & Qi, C. Compositional modification of crude oil during oil recovery. *Journal of Petroleum Science and Engineering* **38**, 1–11 (2003).
72. Aksulu, H., Håmsø, D., Strand, S., Puntervold, T. & Austad, T. Evaluation of Low-Salinity Enhanced Oil Recovery Effects in Sandstone: Effects of the Temperature and pH Gradient. *Energy & Fuels* **26**, 3497–3503 (2012).
73. Anderson, W. G. Wettability Literature Survey—Part 2: Wettability Measurement. *Journal of Petroleum Technology* **38**, 1246–1262 (1986).
74. Austad, T., Shariatpanahi, S. F., Strand, S., Black, C. J. J. & Webb, K. J. Conditions for a Low-Salinity Enhanced Oil Recovery (EOR) Effect in Carbonate Oil Reservoirs. *Energy & Fuels* **26**, 569–575 (2012).
75. Buckley, J. S. Effective wettability of minerals exposed to crude oil. *Current Opinion in Colloid & Interface Science* **6**, 191–196 (2001).
76. Hadia, N. J., Hansen, T., Twehey, M. T. & Torsæter, O. Influence of Crude Oil Components on Recovery by High and Low Salinity Waterflooding. *Energy & Fuels* **26**, 4328–4335 (2012).
77. Kumar, M., Fogden, A., Morrow, N. R. & Buckley, J. S. Mechanism of Improved Oil Recovery From Sandstone by Low Salinity Flooding. *Petrophysics* **52**, 428–436 (2011).
78. Lager, A., Webb, K. J., Black, C. J. J., Singleton, M. & Sorbie, K. S. Low Salinity Oil Recovery - An Experimental Investigation. *International Symposium of the Society of Core Analysts* (2006).

79. Tang, G.-Q. & Morrow, N. R. Influence of brine composition and fines migration on crude oil/brine/rock interactions and oil recovery. *Journal of Petroleum Science & Engineering* **24**, 99–111 (1999).
80. Yildiz, H. O. & Morrow, N. R. Effect of brine composition on recovery of Moutray crude oil by waterflooding. *Journal of Petroleum Science & Engineering* **14**, 159–168 (1996).
81. Zhou, X., Morrow, N. R. & Ma, S. Interrelationship of Wettability, Initial Water Saturation, Aging Time, and Oil Recovery by Spontaneous Imbibition and Waterflooding. *SPE Journal* **5**, 199–207 (2000).
82. Kumar, K., Dao, E. & Mohanty, K. K. AFM study of mineral wettability with reservoir oils. *Journal of Colloid and Interface Science* **289**, 206–217 (2005).
83. Seiedi, O. *et al.* Atomic Force Microscopy (AFM) Investigation on the Surfactant Wettability Alteration Mechanism of Aged Mica Mineral Surfaces. *Energy & Fuels* **25**, 183–188 (2011).
84. Drummond, C. & Israelachvili, J. Fundamental studies of crude oil–surface water interactions and its relationship to reservoir wettability. *Journal of Petroleum Science & Engineering* **45**, 61–81 (2004).
85. Lebedeva, E. V. & Fogden, A. Adhesion of Oil to Kaolinite in Water. *Environ. Sci. Technol.* **44**, 9470–9475 (2010).
86. Lebedeva, E. V. & Fogden, A. Wettability alteration of kaolinite exposed to crude oil in salt solutions. *Colloids and Surfaces A: Physicochemical and Engineering Aspects* **377**, 115–122 (2011).
87. Mahani, H., Berg, S., Ilic, D., Bartels, W.-B. & Joekar-Niasar, V. Kinetics of the Low Salinity Waterflooding Effect Studied in a Model System. *SPE Enhanced Oil Recovery Conference* 1–14 (2013).
88. Lord, D. L. & Buckley, J. S. An AFM study of the morphological features that affect wetting at crude oil–water–mica interfaces. *Colloids and Surfaces A: Physicochemical and Engineering Aspects* **206**, 531–546 (2002).
89. Coleman, J. N., Khan, U., Blau, W. J. & Gun'ko, Y. K. Small but strong: A review of the mechanical properties of carbon nanotube–polymer composites. *Carbon* **44**, 1624–1652 (2006).
90. Jordan, J., Jacob, K. I., Tannenbaum, R., Sharaf, M. A. & Jasiuk, I. Experimental trends in polymer nanocomposites – a review. *Materials Science and Engineering A* **393**, 1–11 (2005).
91. Li, B. & Zhong, W.-H. Review on polymer/graphite nanoplatelet nanocomposites. *Journal of Materials Science* **46**, 5595–5614 (2011).
92. Paul, D. R. & Robeson, L. M. Polymer nanotechnology: Nanocomposites. *Polymer* **49**, 3187–3204 (2008).
93. Tjong, S. C. Structural and mechanical properties of polymer nanocomposites. *Materials Science and Engineering: R: Reports* **53**, 73–197 (2006).
94. Schadler, L. Nanocomposites: Model interfaces. *Nature Materials* **6**, 257–258 (2007).

95. Chen, L., Cheung, C. L., Ashby, P. D. & Lieber, C. M. Single-Walled Carbon Nanotube AFM Probes: Optimal Imaging Resolution of Nanoclusters and Biomolecules in Ambient and Fluid Environments. *Nano Letters* **4**, 1725–1731 (2004).
96. Hafner, J. H., Cheung, C. L., Wooley, A. T. & Lieber, C. M. Structural and Functional Imaging with Carbon Nanotube AFM Probes. *Progress in Biophysics and Molecular Biology* **77**, 73–110 (2001).
97. Wong, S. S., Woolley, A. T., Joselevich, E. & Lieber, C. M. Functionalization of carbon nanotube AFM probes using tip-activated gases. *Chemical Physics Letters* **306**, 219–225 (1999).
98. Woolley, A. T., Cheung, C. L., Hafner, J. H. & Lieber, C. M. Structural biology with carbon nanotube AFM probes. *Chemistry and Biology* **7**, R193–R204 (2000).
99. Cai, M. Nanoscale Mechanical Characterization of Graphene/Polymer Nanocomposites using Atomic Force Microscopy. (2012).
100. Hudson-Smith, N. V. The Effect of Functionalized versus Unmodified Graphene Oxide on Polyimide Nanocomposite Properties. (2015).
101. Southward, R. E., Boggs, C. M., Thompson, D. W. & St. Clair, A. K. Synthesis of Surface-Metallized Polyimide Films via in Situ Reduction of (Perfluoroalkanoato)silver(I) Complexes in a Poly(amic acid) Precursor. *Chem. Mater.* **10**, 1408–1421 (1998).
102. Hummers, J. William S. & Offeman, R. E. Preparation of Graphitic Oxide. *Journal of the American Chemical Society* **80**, 1339 (1958).
103. Marcano, D. C. *et al.* Improved Synthesis of Graphene Oxide. *ACS Nano* **4**, 4806–4814 (2010).
104. Ta, T. C., Sykes, M. T. & McDermott, M. T. Real-Time Observation of Plasma Protein Film Formation on Well-Defined Surfaces with Scanning Force Microscopy. *Langmuir* **14**, 2435–2443 (1998).
105. Buckley, J. S., Takamura, K. & Morrow, N. R. Influence of Electrical Surface Charges on the Wetting Properties of Crude Oils. *SPE Reservoir Engineering* **4**, 332–340 (1989).
106. Buckley, J. S. Chemistry of the Crude Oil/Brine Interface. *Proceedings of the 3rd International Symposium on Evaluation of Reservoir Wettability and Its Effect on Oil Recovery* 33–38 (1994).
107. Buckley, J. S. & Lord, D. L. Wettability and morphology of mica surfaces after exposure to crude oil. *Journal of Petroleum Science and Engineering* **39**, 261–273 (2003).
108. Kokal, S., Tang, T., Schramm, L. & Sayegh, S. Electrokinetic and adsorption properties of asphaltenes. *Colloids and Surfaces A: Physicochemical and Engineering Aspects* **94**, 253–265 (1995).
109. Wang, L., Siretanu, I., Duits, M. H. G., Stuart, M. A. C. & Mugele, F. Ion effects in the adsorption of carboxylate on oxide surfaces, studied with quartz

- crystal microbalance. *Colloids and Surfaces A: Physicochemical and Engineering Aspects* **494**, 30–38 (2016).
- 110. Dishon, M., Zohar, O. & Sivan, U. From Repulsion to Attraction and Back to Repulsion: The Effect of NaCl, KCl, and CsCl on the Force between Silica Surfaces in Aqueous Solution. *Langmuir* **25**, 2831–2836 (2009).
  - 111. Parsons, D. F. & Ninham, B. W. Charge Reversal of Surfaces in Divalent Electrolytes: The Role of Ionic Dispersion Interactions. *Langmuir* **26**, 6430–6436 (2010).
  - 112. Pianegonda, S., Barbosa, M. C. & Y., L. Charge reversal of colloidal particles. *Europhysics Letters* **71**, 831–837 (2005).
  - 113. Sjöström, L., Åkesson, T. & Jönsson, B. Charge Reversal in Electrical Double Layers — a Balance between Energy and Entropy. *Berichte der Bunsengesellschaft für physikalische Chemie* **100**, 889–893 (1996).
  - 114. Zheng, J., Behrens, S. H., Borkovec, M. & Powers, S. E. Predicting the Wettability of Quartz Surfaces Exposed to Dense Nonaqueous Phase Liquids. *Environmental Science and Technology* **35**, 2207–2213 (2001).
  - 115. Szymula, M., Janusz, W. & Jabłoriski, J. Electrochemical Properties of Asphaltene Particles in Aqueous Solutions. *Journal of Dispersion Science and Technology* **21**, 785–802 (2000).
  - 116. Buckley, J. S. & Wang, J. Crude oil and asphaltene characterization for prediction of wetting alteration. *Journal of Petroleum Science & Engineering* **33**, 195–202 (2002).
  - 117. Sayyough, M. H., Hemeida, A. M., Al-Blehed, M. S. & Desouky, S. M. Role of polar compounds in crude oils on rock wettability. *Journal of Petroleum Science & Engineering* **6**, 225–233 (1991).
  - 118. Nasralla, R. A. & Nasr-El-Din, H. A. Impact of Electrical Surface Charges and Cation Exchange on Oil Recovery by Low Salinity Water. *SPE Asia Pacific Oil and Gas Conference and Exhibition* (2011).
  - 119. Nasralla, R. A. & Nasr-El-Din, H. A. Impact of cation type and concentration in injected brine on oil recovery in sandstone reservoirs. *Journal of Petroleum Science & Engineering* **122**, 384–395 (2014).
  - 120. Xie, Q., Liu, Y., Wu, J. & Liu, Q. Ions tuning water flooding experiments and interpretation by thermodynamics of wettability. *Journal of Petroleum Science and Engineering* **124**, 350–358 (2014).
  - 121. Franks, G. V. Zeta Potentials and Yield Stresses of Silica Suspensions in Concentrated Monovalent Electrolytes: Isoelectric Point Shift and Additional Attraction. *Journal of Colloidal and Interface Science* **249**, 44–51 (2002).
  - 122. Takamura, K. & Chow, R. S. The Electric Properties of the Bitumen/Water Interface: Part II. Application of the Ionizable Surface-Group Model. *Colloids and Surfaces* **15**, 35–48 (1985).
  - 123. Hall, J. C. A. C. Collins S. H.; Melrose Stability of Aqueous Wetting Films in Athabasca Tar Sands. *Society of Petroleum Engineers Journal* **23**, 249–258 (1983).

124. Ebeling, D., Ende, D. van den & Mugele, F. Electrostatic interaction forces in aqueous salt solutions of variable concentration and valency. *Nanotechnology* **22**, 1–10 (2011).
125. Mugele, F. *et al.* Ion adsorption-induced wetting transition in oil-water-mineral systems. *Scientific Reports* **5**, 1–8 (2015).
126. Siretanu, I. *et al.* Direct observation of ionic structure at solid-liquid interfaces: a deep look into the Stern Layer. *Scientific Reports* **4**, 1–7 (2014).
127. Ruiter, R. de, Tjerkstra, R. W., Duits, M. H. G. & Mugele, F. Influence of Cationic Composition and pH on the Formation of Metal Stearates at Oil-Water Interfaces. *Langmuir* **27**, 8738–8747 (2011).
128. Marinova, K. G. *et al.* Charging of Oil–Water Interfaces Due to Spontaneous Adsorption of Hydroxyl Ions. *Langmuir* **12**, 2045–2051 (1996).
129. Zhao, C., Ebeling, D., Siretanu, I., Ende, D. van den & Mugele, F. Extracting local surface charges and charge regulation behavior from atomic force microscopy measurements at heterogeneous solid-electrolyte interfaces. *Nanoscale* **7**, 16298–16311 (2015).
130. Kuilla, T. *et al.* Recent advances in graphene based polymer composites. *Progress in Polymer Science* **35**, 1350–1375 (2010).
131. Kim, H., Abdala, A. A. & Macosko, C. W. Graphene/Polymer Nanocomposites. *Macromolecules* **43**, 6515–6530 (2010).
132. Kranbuehl, D. E., Cai, M., Glover, A. J. & Schniepp, H. C. Measurement of the interfacial attraction between graphene oxide sheets and the polymer in a nanocomposite. *Journal of Applied Polymer Science* **122**, 3740–3744 (2011).
133. Wallace, G. G., Kaner, R. B., Muller, M., Gilje, S. & Li, D. Processable aqueous dispersion of graphene nanosheets. *Nature Nanotechnology* **3**, 101–105 (2008).
134. Metwalli, E., Haines, D., Becker, O., Conzone, S. & Pantano, C. G. Surface characterizations of mono-, di-, and tri-aminosilane treated glass substrates. *Journal of Colloid and Interface Science* **298**, 825–831 (2006).
135. Neto, C. & Craig, V. S. J. Colloid Probe Characterization: Radius and Roughness Determination. *Langmuir* **17**, 2097–2099 (2001).
136. Stevens, B. *et al.* Low-Temperature Thermal Reduction of Graphene Oxide Nanobrick Walls: Unique Combination of High Gas Barrier and Low Resistivity in Fully Organic Polyelectrolyte Multilayer Thin Films. *Applied Materials and Interfaces* **6**, 9942–9945 (2014).
137. Wei, Z. *et al.* Nanoscale Tunable Reduction of Graphene Oxide for Graphene Electronics. *Science* **328**, 1373–1376 (2010).
138. Zhang, H.-B. *et al.* Vacuum-assisted synthesis of graphene from thermal exfoliation and reduction of graphite. *Journal of Materials Chemistry* **21**, 5392–5397 (2011).
139. Zhao, B. *et al.* Supercapacitor Performances of Thermally Reduced Graphene Oxide. *Journal of Power Sources* **198**, 423–427 (2012).

140. Zhu, Y. *et al.* Exfoliation of Graphite Oxide in Propylene Carbonate and Thermal Reduction of the Resulting Graphene Oxide Platelets. *ACS Nano* **4**, 1227–1233 (2010).
141. Kong, J.-Y. *et al.* Preparation and properties of polyimide/graphene oxide nanocomposite films with Mg ion crosslinker. *European Polymer Journal* **48**, 1394–1405 (2012).
142. Luong, N. D. *et al.* Enhanced mechanical and electrical properties of polyimide film by graphene sheets via in situ polymerization. *Polymer* **52**, 5237–5242 (2011).
143. Tsai, M.-H., Chang, C.-J., Lu, H.-H., Liao, Y.-F. & Tseng, I.-H. Properties of magnetron-sputtered moisture barrier layer on transparent polyimide/graphene nanocomposite film. *Thin Solid Films* **544**, 324–330 (2013).
144. Tseng, I.-H., Liao, Y.-F., Chiang, J.-C. & Tsai, M.-H. Transparent polyimide/graphene oxide nanocomposite with improved moisture barrier property. *Materials Chemistry and Physics* **136**, 247–253 (2012).
145. Tseng, I.-H., Tsai, M.-H. & Chung, C.-W. Flexible and Transparent Polyimide Films Containing Two-Dimensional Alumina Nanosheets Tempered by Graphene Oxide for Improved Barrier Property. *Applied Materials and Interfaces* **6**, 13098–13105 (2014).
146. Ha, H. W., Choudhury, A., Kamal, T., Kim, D.-H. & Park, S.-Y. Effect of Chemical Modification of Graphene on Mechanical, Electrical, and Thermal Properties of Polyimide/Graphene Nanocomposites. *ACS Applied Materials & Interfaces* **4**, 4623–4630 (2012).
147. Hu, N. *et al.* Graphene Oxide Reinforced Polyimide Nanocomposites via In Situ Polymerization. *Journal of Nanoscience and Nanotechnology* **12**, 173–178 (2012).
148. Liu, H., Li, Y., Wang, T. & Wang, Q. In situ synthesis and thermal, tribological properties of thermosetting polyimide/graphene oxide nanocomposites. *Journal of Materials Science* **47**, 1867–1874 (2012).
149. Min, C., Nie, P., Song, H.-J., Zhang, Z. & Zhao, K. Study of the tribological properties of polyimide/graphene oxide nanocomposite films under seawater-lubricated condition. *Tribology International* **80**, 131–140 (2014).
150. Peng, S., Wang, S., Wan, L. & Dong, B. Polyimide/Graphene Oxide Nanocomposites Films Fabricated by in Situ Polymerization. *The 7th National Conference on Functional Materials and Applications* 579–584 (2010).
151. Tseng, I.-H., Chang, J.-C., Huang, S.-L. & Tsai, M.-H. Enhanced thermal conductivity and dimensional stability of flexible polyimide nanocomposite film by addition of functionalized graphene oxide. *Polymer International* **62**, 827–835 (2013).
152. Wang, C. *et al.* Preparation of amino-functionalized graphene oxide/polyimide composite films with improved mechanical, thermal and hydrophobic properties. *Applied Surface Science* **362**, 11–19 (2016).

153. Wu, C., Li, F., Zhang, Y., Guo, T. & Chen, T. Highly reproducible memory effect of organic multilevel resistive-switch device utilizing graphene oxide sheets/polyimide hybrid nanocomposite. *Applied Physics Letters* **99**, 042108 (2011).
154. Cao, L., Sun, Q., Wang, H., Zhang, X. & Shi, H. Enhanced stress transfer and thermal properties of polyimide composites with covalent functionalized reduced graphene oxide. *Composites: Part A* **68**, 140–148 (2015).
155. Chen, D., Zhu, H. & Liu, T. In Situ Thermal Preparation of Polyimide Nanocomposite Films Containing Functionalized Graphene Sheets. *Applied Materials and Interfaces* **2**, 3702–3708 (2010).
156. Qin, Y. *et al.* Lightweight, Superelastic, and MeMechanical Flexible Graphene/Polyimide Nanocomposite Foam for Strain Sensor Application. *ACS Nano* **9**, 8933–8941 (2015).
157. Zhang, L.-B. *et al.* Preparation, mechanical and thermal properties of functionalized graphene/polyimide nanocomposites. *Composites: Part A* **43**, 1537–1545 (2012).
158. Zhang, L., Wang, J., Yang, S. & Kong, X. Preparation and Characterization of Graphene Sheet-Polyimide Nanocomposite Films. *ACTA POLYMERICA SINICA* 1472–1478 (2014).
159. Zhu, J. *et al.* Multifunctional Polyimide/Graphene Oxide Composites via In Situ Polymerization. *Journal of Applied Polymer Science* 40177 (2014).
160. Shi, H., Li, Y. & Guo, T. In Situ Preparation of Transparent Polyimide Nanocomposite with a Small Load of Graphene Oxide. *Journal of Applied Polymer Science* 3163–3169 (2013).
161. Liang, J. *et al.* Molecular-Level Dispersion of Graphene into Poly(vinyl alcohol) and Effective Reinforcement of their Nanocomposites. *Advanced Functional Materials* **19**, 2297–2302 (2009).
162. Wang, J.-Y. *et al.* Preparation and properties of graphene oxide/polyimide composite films with low dielectric constant and ultrahigh strength via in situ polymerization. *Journal of Materials Chemistry* **21**, 13569 (2011).
163. Xu, Y., Hong, W., Bai, H., Li, C. & Shi, G. Strong and ductile poly(vinyl alcohol)/graphene oxide composite films with a layered structure. *Carbon* **47**, 3538–3543 (2009).
164. Hwang, Y., Heo, Y., Yoo, Y. & Kim, J. The addition of functionalized graphene oxide to polyetherimide to improve its thermal conductivity and mechanical properties. *Polymers for Advanced Technologies* **25**, 1155–1162 (2014).
165. Gonçalves, G. *et al.* Graphene oxide modified with PMMA via ATRP as a reinforcement filler. *Journal of Materials Chemistry* **20**, 9927–9934 (2010).
166. Heuer, A. H. *et al.* Innovative Materials Processing Strategies: A Biomimetic Approach. *Science* **255**, 1098 (1992).
167. Ritchie, R. O. The conflicts between strength and toughness. *Nat Mater* **10**, 817–822 (2011).

168. Wang, J., Cheng, Q. & Tang, Z. Layer nanocomposites inspired by the structure and mechanical properties of nacre. *Chemical Society Reviews* **41**, 1111–1129 (2012).
169. Westbroek, P. & Marin, F. A marriage of bone and nacre. *Nature* **392**, 861–862 (1998).
170. Finnemore, A. *et al.* Biomimetic layer-by-layer assembly of artificial nacre. *Nat Comms* **3**, 966 (2012).
171. Gehrke, N. *et al.* Retrosynthesis of Nacre via Amorphous Precursor Particles. *Chem. Mater.* **17**, 6514–6516 (2005).
172. Tang, Z., Kotov, N. A., Magonov, S. & Ozturk, B. Nanostructured artificial nacre. *Nature Materials* **2**, 413–418 (2003).
173. Alzarrug, F. A. *et al.* The use of different alumina fillers for improvement of the mechanical properties of hybrid PMMA composites. *Materials & Design* **86**, 575–581 (2015).
174. Feng, Q. L., Cui, F. Z., Pu, G., Wang, R. Z. & Li, H. D. Crystal orientation, toughening mechanisms and a mimic of nacre. *Materials Science and Engineering C* **11**, 19–25 (2000).
175. Lee, S. & Sigmund, W. M. AFM study of repulsive van der Waals forces between Teflon AF<sup>TM</sup> thin film and silica or alumina. *Colloids and Surfaces A: Physicochemical and Engineering Aspects* **204**, 43–50 (2002).
176. Franks, G. V. & Meagher, L. The isoelectric points of sapphire crystals and alpha-alumina powder. *Colloids and Surfaces A: Physicochemical and Engineering Aspects* **214**, 99–110 (2003).
177. Loeber, L., Sutton, O., Morel, J., Valleton, J.-M. & Muller, G. New direct observations of asphalts and asphalt binders by scanning electron microscopy and atomic force microscopy. *Journal of Microscopy* **182**, 32–39 (1996).
178. Pauli, A. T., Grimes, R. W., Beemer, A. G., Turner, T. F. & Branthaver, J. F. Morphology of asphalts, asphalt fraction and model wax-doped asphalts studied by atomic force microscopy. *International Journal of Pavement Engineering* **12**, 291–309 (2011).
179. Jäger, A., Lackner, R., Eisenmenger-Sittner, C. & Blab, R. Identification of Microstructural Components of Bitumen by Means of Atomic Force Microscopy (AFM). *Proceedings in Applied Mathematics and Mechanics* **4**, 400–401 (2004).
180. Lyne, Å. L., Wallqvist, V., Rutland, M. W., Claesson, P. & Birgisson, B. Surface wrinkling: the phenomenon causing bees in bitumen. *Journal of Materials Science* **48**, 6970–6976 (2013).
181. Masson, J.-F., Leblond, V. & Margeson, J. Bitumen morphologies by phase-detection atomic force microscopy. *Journal of Microscopy* **221**, 17–29 (2006).
182. Masson, J.-F., Leblond, V., Margeson, J. & Bundalo-Perc, S. Low-temperature bitumen stiffness and viscous paraffinic nano- and micro-domains by cryogenic AFM and PDM. *Journal of Microscopy* **227**, 191–202 (2007).

183. Nahar, S. N., Schmets, A. J. M., Scarpas, A. & Schitter, G. Temperature and thermal history dependence of the microstructure in bituminous materials. *European Polymer Journal* **49**, 1964–1974 (2013).
184. Schmets, A., Kringos, N., Pauli, T., Redelius, P. & Scarpas, T. On the existence of wax-induced phase separation in bitumen. *International Journal of Pavement Engineering* **11**, 555–563 (2010).
185. Soenen, H. *et al.* Laboratory investigation of bitumen based on round robin DSC and AFM tests. *Materials and Structures* **47**, 1205–1220 (2014).
186. Jäger, A., Lackner, R., Eisenmenger-Sittner, C. & Blab, R. Identification of four material phases in bitumen by atomic force microscopy. *Road Materials and Pavement Design* **5**, 9–24 (2004).